2016-12-19

Numerical Investigation of Compressor Non-Synchronous Vibration with Full Annulus Rotor-Stator Interaction

Daniel Espinal
University of Miami, dan_espinal@hotmail.com

Recommended Citation

Espinal, Daniel, "Numerical Investigation of Compressor Non-Synchronous Vibration with Full Annulus Rotor-Stator Interaction" (2016). *Open Access Dissertations*. 1779.
http://scholarlyrepository.miami.edu/oa_dissertations/1779

UNIVERSITY OF MIAMI

NUMERICAL INVESTIGATION OF COMPRESSOR NON-SYNCHRONOUS VIBRATION WITH FULL ANNULUS ROTOR-STATOR INTERACTION

By

Daniel Espinal

A DISSERTATION

Submitted to the Faculty
of the University of Miami
in partial fulfillment of the requirements for
the degree of Doctor of Philosophy

Coral Gables, Florida

December 2016

UNIVERSITY OF MIAMI

A dissertation submitted in partial fulfillment of
the requirements for the degree of
Doctor of Philosophy

NUMERICAL INVESTIGATION OF COMPRESSOR NON-SYNCHRONOUS VIBRATION WITH FULL ANNULUS ROTOR-STATOR INTERACTION

Daniel Espinal

Approved:

Ge-Cheng Zha, Ph.D.
Professor of Mechanical and Aerospace Engineering

Weiyong Gu, Ph.D.
Professor and Chairman of Mechanical and Aerospace Engineering

Kaufui Wong, Ph.D.
Professor of Mechanical and Aerospace Engineering

Guillermo Prado, Ph.D.
Dean of the Graduate School

Brian Haus, Ph.D.
Associate Professor and Chair of Applied Marine Physics

ESPINAL, DANIEL (Ph.D., Mechanical and Aerospace Engineering)

Numerical Investigation of Compressor Non-Synchronous Vibration with Full Annulus Rotor-Stator Interaction (December 2016)

Abstract of a dissertation at the University of Miami.

Dissertation supervised by Professor Ge-Cheng Zha.
No. of pages in text. (121)

The objective of this research is to investigate and confirm the periodicity of the Non-Synchronous Vibration (NSV) mechanism of a GE axial compressor with a full-annulus simulation. A second objective is to develop a high fidelity single-passage tool with time-accurate unsteady capabilities able to capture rotor-stator interactions and NSV excitation response. A high fidelity methodology for axial turbomachinery simulation is developed using the low diffusion shock-capturing Riemann solver with high order schemes, the Spalart-Allmaras turbulence closure model, the fully conservative unsteady sliding BC for rotor-stator interaction with extension to full-annulus and single-passage configurations, and the phase lag boundary conditions applied to rotor-stator interface and circumferential BC.

A URANS solver is used and captures the NSV flow excitation frequency of 2439 Hz, which agrees reasonably well with the measured NSV frequency of 2600 Hz from strain gage test data. It is observed that the circumferentially traveling vortex formed in the vicinity of the rotor tip propagates at the speed of a non-engine order frequency and causes the NSV. The vortex travels along the suction surface of the blade and crosses the passage outlet near blade trailing edge. Such a vortex motion trajectory repeats in each blade passage and generates two low pressure regions due to the vortex core positions, one at the leading edge and one at the trailing edge, both are

oscillating due to the vortex coming and leaving. These two low pressure regions create a pair of coupling forces that generates a torsion moment causing NSV.

The full-annulus simulation shows that the circumferentially traveling vortex has fairly periodical behavior and is a full annulus structure. Also, frequencies below the NSV excitation frequency of 2439 Hz with large amplitudes in response to flow-separation related phenomena are present. This behavior is consistent with experimental measurements. For circumferentially averaged parameters like total pressure ratio, NSV is observed to have an effect, particularly at radial locations above 70% span. Therefore, to achieve similar or better total pressure ratio a design with a smaller loading of the upper blade span and a higher loading of the mid blade spans should be considered.

A fully-conservative sliding interface boundary condition (BC) is implemented with phase-lag capabilities using the Direct Store method for single-passage simulations. Also Direct Store phase-lag was applied to the circumferential BCs to enforce longer disturbance wavelengths.

The unsteady simulation using single-blade-passage with periodic BC for an inlet guide vane (IGV)-rotor configuration captures a 2291 Hz NSV excitation frequency and an IGV-rotor-stator configuration predicts a 2365 Hz NSV excitation frequency with a significantly higher amplitude above 90% span. This correlates closely to the predicted NSV excitation frequency of 2439 Hz for the full-annulus configuration. The two-blade-row configuration exhibits the same vortex structures captured in the full-annulus study. The three-blade-row configuration only captures a tip vortex shedding at the leading edge, which can be attributed to the reflective nature of the BCs causing IGV-rotor-stator interactions to be augmented, becoming dominant and shifting

NSV excitation response to engine order regime. Phase-lag simulations with a Nodal Diameter (ND) of 5 is enforced for the circumferential BCs for the three-blade-row configuration, and the results exactly matched the frequency response and flow structures of the periodic simulation, illustrating the small effect that phase-lag has on strongly periodic flow disturbances. A ND of 7 is enforced at the sliding interface, however the NSV excitation completely disappears and only the wake propagation from IGV-Rotor-Stator interactions are captured. Rotor blade passage exhibits a circumferentially travelling vortex similar to those observed in the full-annulus and two-blade-row simulations. This can occur when the rotating instability responsible for the NSV no longer maintains a pressure variation with a characteristic frequency signature as it rotates relative to the rotor rotation, and now has become the beginning of a spike-type stall cell. In this scenario the travelling vortex has become evidence of part-stall of the upper spans of the rotor blade, but stalling is contained maintaining stable operation.

In conclusion, an efficient method of capturing NSV excitation has been proposed in a high-fidelity manner, where only 2% of the computational resources used in a full-annulus simulation are required for an accurate single-blade-passage multi-stage simulation.

Dedicated to Jesus Christ, my wife and to my parents
for their love, support, encouragement and inspiration.

Acknowledgements

I would like to express my most sincere gratitude to my academic advisor and mentor, Professor Ge-Cheng Zha, whose invaluable investment in my formation and patience during my doctorate will forever be appreciated and cherished.

I owe a special thank you to Dr. Hongsik Im for his guidance, advice and inspiration for my research work in the CFD laboratory. His role as a second mentor during my stay at the University of Miami will not be forgotten. I also want to thank Dr. Jiaye Gan for his insightful discussions and friendship.

I also would like to thank my dissertation committee members, Professor Weiyong Gu, Professor Kau-Fui Wong and Professor Brian Haus, for their insightful review and suggestions on my research work.

Most importantly I want to express my utmost gratitude to my wife, Dui, for her long enduring support and unconditional love throughout this process. And to my parents, Augusto and Francy, for always being the support I've needed during the most critical moments of my doctorate.

Thank you all for your support.

Daniel Espinal

University of Miami

December 2016

Table of Contents

List of Figures

CHAPTER 1

Introduction

Aircraft engine manufacturesrs have been in a race to the bottom in terms of engine weight, size and fuel consumption. This has led competitors to try to achieve the required engine performance with the least amount of compressor and turbine stages. For example, GE LEAP engines rely on advances in materials to make its blades lighter, effectively reducing weight, where as Pratt & Whitney has weight and fuel saving in their PurePower turbofan engines by adding a gear between the fan and compressor requiring less compressor and turbine stages. However, the push for smaller, lighter engines has caused loads on individual blade-rows to increase significantly giving rise to new structural challenges, which will affect blade fatigue life and engine operational costs. These factors must be taken into consideration at earlier phases of the design process.

Turbomachinery computational fluid dynamics (CFD) has been an invaluable tool for the industry starting in the 1960s [7]. In the beginning, simulation used models based on little more than velocity triangles until Wu [8] introduced the S1-S2 or blade-blade-throughflow model. Eventually it was replaced by time-marching solutions of compressible Euler equations on 2D then 3D blade-blade analysis. This in turn evolved from inviscid to viscous analysis and then from steady to unsteady flow simulations. Currently turbomachinery CFD is moving toward the solution of aeroelastic problems through the use of fluid-structure interaction (FSI) techniques.

Progress in turbomachinery CFD has the potential to predict problems that usually are observed during rig testing of compressor and turbine designs such as stall and surge, flutter, and non-synchornous vibration (NSV) amongst other issues. This possibility would reduce development costs for engine manufacturers. Nevertheless, increased problem complexity usually comes with computational costs that make it prohibitively slow and expensive to use earlier in the design process, especially when studying phenomena whose disturbance wavelengths span large sections of the annulus (i.e. multiple blade passages). In order to overcome these challenges phase-lag boundary conditions (BCs) have been implemented to be able to capture accurately flow unsteadiness both circumferentially and across multi-blade-row (rotor-stator) interfaces, allowing large domain simulations to be reduced to single-passage or two-passage simulations.

The push for higher stage efficiencies has forced blade design to increase in complexity as well. Techniques such as blade sweep and lean make it imperative that secondary flow losses, like those presented by Denton [9], be captured by simulations for design and off-design operating conditions to ensure high system efficiency throughout operational envelope. For this reason high-fidelity CFD modelling is necessary to become part of the designer toolbox at an early stage of the design.

In conclusion, since the advent of faster and cheaper computational capabilities industries have began to rely more heavily on computer simulations for research, development and design instead of an experimental approach. Furthermore, advancements in materials engineering has allowed the turbomachinery industry to develop compressor and turbine blades with a thinner profile which makes them lighter, effectively reducing total engine weight, but more susceptible to fatigue and failure induced by blade vibration. Also blade design and optimization has matured to a point where high-fidelity computer modelling is becoming a necessity earlier in the design process while maintaining computational costs to a minimum.

1.1 Non-Synchronous Vibration

Non-synchronous vibration (NSV) in turbomachinery is primarily an aeromechanic problem where a fluid dynamic instability is the primary driver of blade vibration with frequencies non-integral to the engine order. Rotating Instability (RI) is considered as one cause of NSV [6, 10–12]. Baumgartner et al. [6], Kielb et al. [10], Marz et al. [11] and Mailach et al. [12] observed in their experiments high vibrations with frequencies that are not in resonance with engine orders under operating conditions away from the stall boundary. Detection of RI frequencies have a radial dependency, where the strongest effects are found at upper blade spans and can be attributed to vortex structures and flow instabilities present near the blade tip and tip gap. Vortex structures and flow instabilities also propagate circumferentially in the relative frame, hence the rotating designation. Experiments and simulations by Marz et al. [11], Mailach et al. [12] show that a large tip clearance size as the main influence parameter on the rotating instability.

Measurements on the first rotor of a 10 stage high pressure compressor by Baumgartner et al. [6] showed high levels of blade vibration at NSV frequencies. The excitation source can be attributed to a rotating flow instability in the blade tip region of the first compressor rotor. Similar to rotating stall, the RI is attributed to a vortex shedding mechanism that moves relative to the blade row and generates pressure waves. The frequencies of the RI are visible at 91% blade span with high coherence levels dying away from the RI center. At 65% blade span the aerodynamic excitation from RI is no longer detectable.

An experimental and numerical investigation for a full size compressor rig conducted by Kielb et al. [10] had blade-mounted strain gages and case-mounted unsteady pressure transducers to measure the NSV. Strain gage data captured during slow rotor acceleration show a step change in frequency showing lock-in behavior which is a characteristic of NSV. High amplitude response is observed at 2661 Hz at 12700 rpm near first torsional mode (1T), shifting from 2661 to 2600 Hz at 12800 rpm. Numerical results for the 1/7th rotor annulus indicate a suction side vortex shedding and a tip flow instability near 75% span as the excitation source of the NSV.

Marz et al. [11] presents an experimental and numerical study for a low speed single stage fan with outlet guide vanes with RI as the main source of NSV. Four different tip clearances of 0.7%, 1.4%, 2.8%, and 5.6% of tip axial chord were tested at near the maximum fan loading condition. For clearances of 2.8% and 5.6% casing wall pressure measurements near the maximum fan loading captured the rotating instability in the rotor entry plane where the flow intensity varies from blade to blade; the blade sensor signal near the rotating instability has a strong periodic content. Measured wall pressure spectrum shows the rotating instability with a frequency roughly half of BPF which is the NSV. A full annulus simulation of the 2.8% configuration found a vortex structure moving from the suction side to the pressure side in the middle of the blade passage as the main cause of unsteadiness.

Mailach et al. [12] investigated the influence of tip clearance and operating point on rotating instability in an experimental study of a low speed research compressor. Tip clearances of 3% and 4.3% of tip axial chord exhibited rotating instabilities, with the 4.3% tip clearance rotating instability fully developed for all the rotor speeds including 50%, 80%, and 100% design speed for a narrow operating range near the stall boundary. Measurements on the rotor blades show that the rotating instability is limited to the blade tip region and maximum amplitudes appear at 92% of the blade height and 20% to 30% of chord length. Compressor approach of the stall boundary causes the rotating instability to shift to slightly lower frequencies and growth of perturbation amplitude. For a large tip clearance the fluctuating blade tip vortices propagate circumferentially in the rotor tip region. Overall tip clearance size is observed to be the main factor influencing the rotating instability.

However, Im and Zha [13] discovered that the NSV is caused by the circumferential traveling vortices in the tip region, which is mostly created by over loaded upper span. The tip clearance variation changes the excitation frequency and amplitude of aerodynamic forcing, but the existence of NSV is independent of tip clearance size.

Thomassin et al. [14, 15] suggested a theory different from the rotating instability to explain the NSV based on the resonance of an impinging jet vortex structure and the acoustic feedback of a vibrating plate. The jet core feedback theory has been proved by an experiment conducted in [14, 15]. It shows that when the acoustic reflection wave length equals to the jet-to-plate distance, the jet vortical structures lock-on to the acoustic wave frequency and significant amplification of the pressure fluctuation and vibration of the flexible plate are observed. They suggest a simple model to predict the critical tip velocity based on their impinging jet experiment.

Vo's [16] simulation shows a tip clearance flow instability for an isolated subsonic axial compressor rotor. In the blade tip region the trailing edge backflow causes flow impingement on the pressure side that leads to the flow unsteadiness associated with NSV.

Measurements by Sanders [17] captured NSV phenomenon for a low aspect ratio fan stage stator and the URANS simulation demonstrates that the NSV is driven by dynamic stalling of the fan stator due to unsteady shock-boundary layer interaction.

While much research has been performed on NSV phenomena after the fact as shown above, there have been recent efforts attempting to develop prediction models and tools for the preliminary design stage to prevents NSV before getting to expensive full annulus simulations and experimental measurements. The first model proposed by Thomassin et al. [14,15] is based on the jet core feedback theory previously mentioned. The predicting parameter of NSV is the critical tip velocity (U_{tip_c}) shown to be defined as

$$U_{tip_c} = 2(c - 2sf_b/n) \tag{1.1}$$

where c is the blade tip speed of sound, s the blade pitch, f_b is the blade natural frequency, and n an integer that takes into account harmonics of jet core acoustic wave. Designers should keep tip clearance flow velocity away from U_{tip_c}, since the critical condition would initiate NSV. However, the coefficients in Eq. (1.1) are based on empirical approximations and not generalized for all compressor.

The second prediction tool proposed by Clark et al. [18] is mapping turbomachinery characteristics onto a multi-degree-of-freedom van der Pol oscillator since it is able to capture the two main characteristics of NSV observed experimentally: a stable limit cycle oscillation (LCO) and a lock-in phenomenon both maintained for various conditions. The basic approach is to model a coupled fluid-structure system where the fluid is modeled by the van der Pol equation and the structure is modeled by a standard second order linear differential equation, which can then be used to test conditions that exhibit LCO. While as a mathematical model the van der Pol oscillator has the potential to model NSV, the relationship between fluid-structure coupling coefficients and turbomachinery design parameters has yet to be determined.

Both prediction tools proposed by [14, 15] and [18] are valuable during preliminary design, however a high fidelity simulation at the early stages of design may be more reliable than empirical calibration of mathematical models. This is the approach proposed in the present work, where a high-fidelity single-passage simulation is used to capture NSV using methods validated using a full-annulus configuration.

A high-speed axial compressor is simulated in this study, which exhibits a strong non-engine order vibration of the 1st stage rotor blades close to the blade 1T (1st torsional) mode during engine rig tests [10] (see Fig. 1.1). The NSV frequency collapses between 2600 Hz and 2661 Hz with a large amplitude, which is considered as a lock-in phenomenon [18]. The NSV frequency is shifted from 2600 Hz to 2661 Hz as the rotor speed slightly decreases roughly from 12800 RPM to 12700 RPM. The rig test [10] confirms the NSV occurrence before stall. The rotor tip clearance of the full compressor rig is about 1.1% of tip chord.

Previous efforts by Im and Zha [13, 19] and Gan et al. [20] have adopted a 1/7th sector of the full-annulus configuration to simulate the first 1-1/2 stages of this compressor due to geometric periodicity. Since NSV is an unsteady phenomenon, to enforce flux conservation across rotor/stator interfaces, a fully conservative sliding

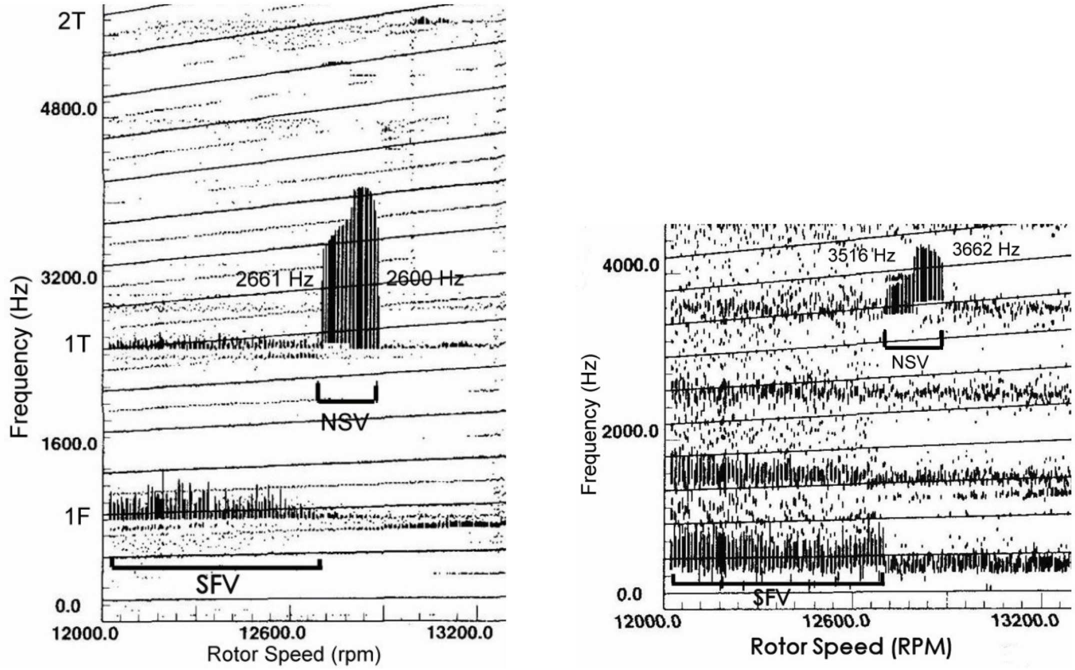

Figure 1.1: Strain gage response (left) and casing unsteady pressure measurements (right) of the first-stage rotor blades of the high-speed compressor showing SFV(separated flow vibration) and NSV(non-synchronous vibration)

boundary condition (BC) was adopted. The flow is treated at the circumferential boundaries with a time-shifted phase-lag BC to capture the travelling waves. Even though the accuracy of phase-lag BCs is an approximation, there has not been any full-annulus simulations thus far aimed at validating the prediction of NSV.

1.2 Full-Annulus Turbomachinery Simulations

Full-annulus simulations have been used to investigate the flow mechanisms of stall inception since the flow has no circumferential periodicity [21–28]. Simulations of single blade-row configurations are aimed at fan and compressor first stage rotors with a high emphasis at characterising the type of stalling the rotor undergoes. Lin et al. [24] simulated a low-speed compressor rotor and found that short-length-scale disturbances from inlet distortion can cause a spike-type stall. Hah et al. [21] investigated the front stage of a high-pressure transonic compressor rotor using a URANS and a LES modelling approach and discovered spike-type rotating stall. Im et al. [22] and Khaleghi et al. [29] simulated the transonic NASA rotor 67 configuration and captured spike stall inception. A high-fidelity DES method was used by [22] which is high order but computationally more efficient than LES modelling. All transonic rotor simulations showed that when tip shock detached from the blade LE the tip clearance vortex would trigger spike-type stall. Also [21–24] found that the stall cells would travel counter to rotor rotation direction at a fraction of wheel speed in the relative frame.

Full annulus Simulations of multiple blade-row configurations were carried out by Chen et al. [27, 28] and Gan et al. [25, 26] using the transonic NASA stage 35 benchmark to capture rotating stall inception. Both [27,28] and [25] used URANS to solve the stall inception at full design speed; [26] recently used DDES to capture the stall mechanism. NASA stage 35 simulations also provide clarification to the fact that rotor-stator interaction does not affect significantly the onset of flow instabilities and their propagation, although Sanders [17] did find computationally that effects from flow instabilities, which include NSV, can be augmented locally by large downstream struts in a low aspect ratio fan stage stator.

Due to the unsteadiness of complex flow phenomena in turbomachines, the limitations brought by periodicity assumptions must be overcome in order to resolve more realistically flow structures. Since the knowledge on NSV excitation is very limited, there are some questions that need to be answered: 1) Is NSV excitation a full annulus phenomenon or a local phenomenon? 2) What are the NSV excitation characteristics along the circumference, periodic or aperiodic? Only a full annulus simulation can answer these questions, as it has been done for stall inception. The answer is also very important to guide the reduced model using a sector of the annulus and the validation of Phase-lag boundary conditions.

1.3 Phase Lag Boundary Condition

CFD boundary conditions have intricate histories, and as understanding of Fluid Mechanics increases, so does the application of BC's for CFD modelling in turbomachinery applications. Phase lag BC's started out as a method meant to allow multi-stage simulations whose geometry was not periodic in a single passage. Improvements in CFD modelling capabilities have allowed the focus of their development increasingly toward capturing Fluid-Structure Interaction (FSI) phenomena such as blade-row vibration under different nodal diameter (ND) and the corresponding fluid response and system coupling. This section will outline the early development of the phase lag BC and later go in-depth to the current state-of-the-art uses for it.

Originally the main focus of turbomachinery was to accurately capture overall characteristics of the machine such as total pressure ratios, flow angles and pressure distributions on the blade surface. Therefore most of the work focused on simulations of cascades and achieving an accurate steady-state solution. When attention was placed to rotor-stator interactions several problems arose:

1. Unsteady effects could no longer be ignored due to wake propagation and wave reflection playing an important role in the overall performance of the stage.

2. Circumferential BC's assumed a periodic boundary because in relative frame each passage in a blade row should be in a steady-state.

Since this assumption broke down when there was no longer geometric periodicity between blade rows due to different number of blades, a more faithful BC was required, hence phase lag BC's.

First, the view of phase lag in this context must be understood. For a single blade row the dominant period is $T = \frac{2\pi}{N}$. Now when 2 blade rows are interacting the dominant period is neither of the two, but their beating namely $T = \frac{2\pi}{\Delta N} = \frac{2\pi}{N_2 - N_1}$, which is the period of a longer circumferential wavelength which produces a phase lag in the circumferential direction for a single passage of either blade row.

Many attempted to circumvent this issue by decreasing the size of the upstream blades to match the periodicity circumferentially. Others increased the size of the downstream blades. But this new dimensioning had many issues (Different loading, blockage, etc.). This method allowed geometric periodicity and therefore periodic BC's could be used, even at the interface, which allowed for unsteady simulations without the use of a mixing plane BC at the interface. However results from such simulations could not be heavily relied on for stage unsteady behavior.

The first to tackle the issue head on was Erdos in 1977 [1] who developed a technique where data was stored for the previous period (T) and transferred the flow variables from a Δt before across circumferential boundaries. This Δt was computed based on the IBPA (Inter-Blade Phase Angle). With this very same method Erdos also reconstructed interface values circumferentially applying the phase lag to fill in "non-overlap" regions of a reduced model (see Fig.1.2). This method has no loss in fidelity but is the most computer memory intensive than the rest of the phase lag BC's.

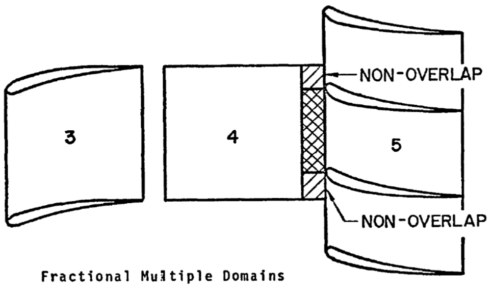

Figure 1.2: Region of non-overlap between rotor passage and stator passage where flow is reconstructed based on IBPA (plot adopted from [1]).

Shape Correction Method, also known as Fourier series decomposition phase lag method, assumes that the flow variables can be split into a steady and an unsteady component as in Eq. 1.2

$$U(x,y,r,t) = \bar{U}(x,y,r) + \tilde{U}(x,y,r,t) \tag{1.2}$$

where U represents any flow feature in the passage, $\bar{U}$ is the steady-state (time-averaged) component and $\tilde{U}$ is the unsteady component that will be decomposed into a Fourier series assuming a period T and of the form shown in Eq. 1.3

$$\tilde{U}(t) = \sum_{n=1}^{N_F} [A_n sin(n\omega t) + B_n cos(n\omega t)] \tag{1.3}$$

where $\omega = 2\pi/T$ which is the disturbance frequency. By using this method it is only necessary to save the coefficients A_n and B_n. This method is proposed by He and

Denton [30]. More details will be presented in Chapter 3, including the relations for the coefficients.

The Time-Inclined Computational Plane method proposed by Giles in 1988 [2] attempts to go back to the periodicity assumption by rotating the temporal plane artificially in the governing equations. An illustration is shown in Fig.1.3. The temporal plane rotation also rotates the fluxes across the cells in the temporal plane and the whole Navier Stokes equations must be rotated for the method to be consistent. While clever, this method would require a new N-S rotation for every IBPA under consideration, which constraints it into a single perturbation under consideration. This technique has not been matured and therefore is not widely used.

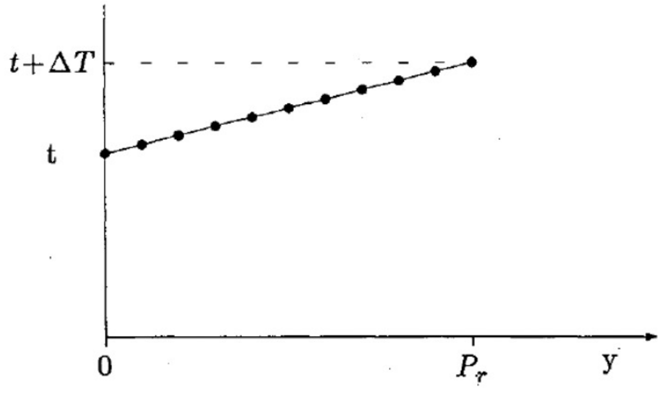

Figure 1.3: Illustration of Time-Inclined Computational Plane method by Giles [2](plot adopted from [2]).

In conclusion, in its early development the concept of phase lag was introduced because the cascade view of rotors could not satisfy the physical unsteady effects when a stator was present with a different blade count. Therefore the motivation for a phase lag BC was geometric, not vibratory.

Srivastava et al. [31] compared the direct store method and the Fourier phase lag BC for a turbine cascade, and showed that once convergence is achieved, similar results are obtained, including unsteady behaviors. However, the Fourier phase lag BC posed the disadvantage of requiring to input the primary perturbation, or vibration frequencies, although such frequencies are not known *a priori*. In other words, the TSPL BC is more general than the Fourier phase lag BC, but still limited to the temporal periodicity assumption, which does not necessarily exist when flow instabilities are present.

When research and commercial CFD software advances allowed the modelling of Fluid-Structure Interaction (FSI) in turbomachinery, a further emphasis on the vibration Nodal Diameter (ND) and the circumferential wavelength of the corresponding travelling wave has moved development of the phase-lag BC onto modelling the damping characteristics of compressors and turbines. Li and He [32] and Im and Zha [33] validated the Shape Correction and Direct Store Methods respectively with single-passage and multiple passage simulations of NASA rotor 67. Consequently Li and He [3, 5] studied the damping characteristics of different ND for a compressor stage (rotor-stator) and a 1-1/2 transonic compressor stage (IGV-rotor-stator) and the effects of intra-row spacing on vibration damping. Im and Zha [33, 34] focused on the application of the Direct Store method to enforce the circumferential wavelength across circumferential BCs while a fully coupled FSI methodology was implemented to blade vibration of NASA rotor 67 [33] and a transonic fan rotor [34]. Their simulations showed that different NDs can affect the stability of the system, in the case of [34] flutter ensues.

1.3.1 Multi-Stage Unsteady Single-Passage Simulations

The challenge of a multi-stage simulation is the treatment of the interface between blade-rows, and the blade-row interaction across the interface introduces unsteadiness to the flow that must be modelled. There are typically two approaches to treat two adjacent blade rows in relative rotation frame; mixing plane and sliding interface.

Mixing plane method has been widely used due to its simplicity. Denton [35], Dawes [36], Singh [37], and Chen [38] used mixing plane approach to calculate multistage machines. In this approach the circumferential-averaging is typically used in order to achieve the radial profiles and conserve the mass flow. However the disadvantages of mixing plane are that it generates artificial mixing loss [39] due to averaging the non-uniform flow at the mixed-out and mixed-in plane, and the effects of unsteady interaction between inter-blade rows could not be taken into account.

Sliding interface methods are often used for multi-stage unsteady rotor-stator interaction. Numerous studies on the unsteady rotor/stator interaction has been developed [2, 40–42] based on interpolation on the rotor-stator interface. Chen et al. [43] pointed out that lack of flux conservation can significantly affect the solution accuracy where shock interaction exists between the blade rows. The fact is the methods of rotor/stator interaction using any type of interpolation methods can not satisfy the conservation of the flux across the interface.

In this thesis, a fully conservative sliding BC based on one-to-one interface mesh is developed with high order shock capturing schemes to accurately capture the unsteady interaction between rotor and stationary blades. The implementation of a sliding BC for a full annulus configuration or for a geometric periodic stage sector is straight forward; however, a sliding interface for single-passage multi-stage simulations has complications regarding data exchange across the interface due to the non-overlaping regions (see Fig.1.2) that arise from geometric non-periodicity (different number of blades for each blade row). As explained above, phase-lag techniques have been used to fill the gaps.

Zaki et al. [44] and Davis and Yao [45] performed single-passage simulations of stall inception in NASA stage 35. [45] used a mixing-plane approach at the rotor-stator interface and [44] used a sliding interface, both working under the assumption of blade passage to blade passage periodicity; no phase-lag was implemented. Both [45] and [44] were able to capture unsteady flow physics relating to NASA stage 35 stall mechanism, but with limitations relating to stall cell size and propagation.

Simulations by Castillon [46] and Castillon et al. [47] used a Shape Correction method with multiple frequency capabilities for the rotor-stator sliding interface of several turbine and compressor stages. [46] simulated two quasi-3D single-passage configurations: the 1.5 turbine stage Vega3 and the 3 stage axial compressor CREATE. Results were validated with full-annulus configurations and showed that the multiple frequency phase lag method was able to capture properly the unsteady characteristics of the flow field, especially for neighboring blade rows (N and N+1). However unsteady effects induced by clocking (N and N+2) are not well captured when compared to the multi-passage reference computations. Similar observations are made for a full 3D simulation of the 3 stage compressor CREATE in [47] using the same interface treatment.

Gerolymos et al. [48] also applied the Shape Correction method for single-passage simulations of a 1.5 turbine stage, a transonic compressor stage (IGV-rotor), and a compressor stage (rotor-stator). Of special interest is the ability of the phase-lag BC capability to handle the non-linearity of the shocks in the transonic compressor. Gerolymos [49] presents an extensive review of phase-lag BC methodologies and applications, with a focus on variations of the Shape Correction Phase Lag technique including the multiple frequency phase lag used by Castillon et al. [46, 47]. However it can be noted that the strength of these approaches is in capturing unsteady effects caused by blade passing propagating through multiple blade rows. The frequencies of these type of phenomena can be known ahead of time due to its synchronous nature. Since the aerodynamic excitation frequencies for the NSV problem are asynchronous and not known, this approach is not suitable to treat sliding interface and circumferential BCs.

From the present review it can be observed that a Direct Store Phase Lag treatment has not been widely used for multi-stage single-passage simulations due to the high requirements on computer memory to store instantaneous flow characteristics over a long period of time. However, computer memory has been more readily available over time and at present most systems are capable of managing the demands of Direct Store Method on the computation. Furthermore, it is known that the Direct Store Method has no loss in fidelity and therefore should capture phenomena that could fall outside of the linearity assumptions for Fourier decomposition used in the Shape Correction Method. The present work will focus on implementing the Direct Store Method to the single-passage simulation to capture NSV excitation frequencies.

1.4 High Order Shock Capturing Scheme

The essentially non-oscillatory (ENO) or weighted essentially non-oscillatory (WENO) schemes are attractive for their capability to capture discontinuities and achieve the consistent high order accuracy in smooth regions. By using a convex combination of all candidate stencils to replace the smoothest one in the ENO scheme, a WENO scheme has more advantages over its ENO counterpart. For example, it approaches certain high order accuracy in smooth regions and has better convergence rate due to the smoother numerical flux used. From its inception [50, 51] to present, the WENO schemes have been extensively applied to different flow problems in many areas.

In a WENO scheme, a Riemann solver is needed to capture the discontinuities. There are two ways to evaluate the Riemann solver fluxes. For WENO finite difference schemes, Shu suggested that the WENO reconstruction be directly applied to the split fluxes from left or right [52]. In this research, we employ a different method, which is to evaluate the conservative variables with WENO scheme and then use the conservative variables to calculate the fluxes based on the Riemann solvers. This is similar to the MUSCL method of Van Leer [53].

Zhang and Shu [54] found that, when a 5th order WENO scheme combined with a Runge-Kutta time discretization is used to achieve steady state solutions, the residual stops dropping at the truncation error level of the scheme, which is far above the machine zero. They noticed that the original smoothness indicator of Jiang and Shu [51] results in a small oscillation near a steady shock wave. The oscillation propagates to the smooth region and causes the residual to hang at the truncation error level rather than to approach machine zero. They proposed a modified smoothness indicator near the shock region for the fifth order WENO scheme, which can drive the residual to machine zero for some 1D and 2D problems without the influence from the boundary conditions. But for the other examples, the residuals still fluctuate at the level of ($10^{-2} \sim 10^{-4}$). Zhang and Shu [54] attribute the convergence difficulty to the influence of boundary conditions. At a critical point (the first derivative is zero), the first term in the Taylor series expansion of the IS_k of Zhang and Shu does not satisfy the requirement of $IS_k = D(1 + O(\Delta x^{r-1}))$ to achieve 5th order accuracy. Thus the accuracy of the scheme of Zhang and Shu [54] is only 3rd order at a critical point.

Henrick et al. [55] proposed a mapped WENO scheme to achieve the optimal accuracy order at the critical point of a smooth function and discussed the choice of ε value for the 5th order WENO scheme. When ε is dominant in magnitude, the preconditions of WENO5 scheme approaches those of a central difference scheme. Furthermore, the oscillation on the order of ε^2 may exist near discontinuities. Hence if the ε is too large, it will mitigate the ENO behavior of the method. Henrick et al. suggested that ε can be slightly larger than the square root of the smallest positive number allowed for a particular machine. But they didn't study the convergence behavior for computing steady state solutions.

In this research, the 5th order finite differencing WENO scheme [56, 57] is used to evaluate the inviscid fluxes, and the 4th order central differencing scheme [58] is used to calculate the viscous fluxes. The WENO scheme adopted uses an optimized ϵ value and is able to remove the weights oscillation, maintain the sensitivity to shock and contact surface discontinuities, achieve optimal weights and thus the minimal dissipation, and obtain solid convergence to machine zero.

An upwind scheme is required as a Riemann solver when a high order WENO scheme is used. The upwind schemes are designed to make the flux computation based on the flow characteristics. The upwind schemes have inherent numerical dissipation, which makes the artificial dissipation unnecessary. The approximate Riemann solver scheme developed by Roe [59] is one of the most famous upwind schemes. By introducing the Jacobian and Roe's average for the variables, the Roe scheme exactly satisfies the Rankine-Hugonoit relations and directly capture the discontinuities. The Roe scheme was considered as the most accurate scheme among the available differencing schemes in 1987 [60]. But the Roe scheme uses matrix dissipation and hence it is time consuming.

To achieve the purpose of efficiency, accuracy and simplicity to use, many efforts have been made to develop upwind schemes only using scalar dissipation instead of matrix dissipation such as that of the Roe's flux difference splitting (FDS) scheme [59]. Pioneered by Liou and Steffen [61], the researchers seeking the scalar dissipation primarily follow the guideline that the velocity and pressure should be separated to consider their characteristics representing the physics of the convection and waves. Liou and his colleagues termed their schemes as advection upstream splitting method(AUSM) schemes, and Jameson gave the name of convective upwind and split pressure (CUSP) schemes [62, 63].

Zha et al. recently suggested a Low Diffusion E-CUSP (LDE) scheme [64] using the Mach number splitting of Edwards's LDFSS schemes [65, 66] for the convective flux. The LDE scheme has low diffusion and can capture crisp shock wave profiles and exact contact discontinuities [64]. The scheme is consistent with the characteristic directions due to the nature of E-CUSP scheme. The solutions calculated by the new scheme is smooth and the scheme can capture crisp shock profile and exact contact discontinuity. In this thesis, the LDE scheme is used for all cases studied. It is shown by extensive turbomachinery validations that the LDE scheme accurately predicts turbomachinery flows with strong shock/boundary layer interactions and shows its robustness for turbomachinery aeromechanical applications as well.

1.5 Research Strategy

A high fidelity numerical strategy for turbomachinery is established to accommodate both full-annulus and single-passage capabilities for unsteady multi-stage simulations with the following developments:

1. An accurate rotor/stator sliding BC is developed for multistage turbomachinery simulation in order to resolve the wake propagation between blade rows. This includes the creation of an advanced multiprocessor algorithm for the even distribution of computational load for the full-annulus configuration. Also implementation of the Direct Store phase-lag method to the sliding interface for single-passage simulations is developed to handle geometric non-periodicity due to differing blade counts across blade-rows.

2. For sector of annulus simulations, circumferential boundary conditions are implemented to consider the effect of phase angle difference using a Direct Store phase lag approach.

3. Advanced numerical algorithms are adopted for high speed axial fan/compressor simulations. An efficient and low diffusion E-CUSP (LDE) scheme is used as a shock capturing Riemann solver to resolve discontinuities with minimal

> numerical dissipation. An implicit high order accuracy weighted essentially non-oscillatory (WENO) scheme for the inviscid flux is employed with a set of fully conservative high order central differencing for the viscous terms to accurately capture the nonlinear interaction of vibrating blades with the flow.

After implementation, the method described above will be validated with experimental data presented in [10] where NSV is measured for an 1.5 stage axial compressor. First, a full annulus simulation will be performed to test the sliding BC without phase-lag and to capture NSV excitation and the flow mechanisms that causes it. Lastly, a single-passage configuration will be tested and validated with both the full-annulus simulation and rig test data.

1.5.1 Objectives

The objective of this research is to investigate and confirm the periodicity of the NSV mechanism of a GE axial compressor with a full-annulus simulation. A second objective is to develop a high fidelity single-passage tool with time-accurate unsteady capabilities able to capture rotor-stator interactions and NSV.

1.5.2 Outline of Dissertation

The outline of the present dissertation starts with the present chapter where an introduction and literature review are performed. Chapter 2 starts with the derivation of the time accurate Navier-Stokes equations in a rotating frame as the flow governing equations. The chapter ends with the description of the numerical methods including the implicit discretization of the Navier-Stokes equations, the low diffusion E-cusp scheme as an accurate approximate Riemann solver, and the high order inviscid and viscous flux reconstruction schemes. In Chapter 3 turbomachinery boundary conditions used in this research are presented in detail, including fully conservative rotor-stator sliding interface with treatments for full-annulus and single-passage simulations.

After a theoretical foundation has been established, in Chapter 4 a 1.5 stage high-speed compressor is simulated using a full-annulus configuration to investigate the NSV aerodynamic excitation without circumferential sector boundary condition effect. A set of single-passage simulations are performed in Chapter 5 using the high fidelity approach ascribed to capture the NSV aerodynamic excitation.

CHAPTER 2

Theory

2.1 Navier-Stokes Equations in Rotating Frame

The equations of motion of fluid flow for turbomachinery are derived in a moving frame of reference in order to take into account the effects of Coriolis force ($2\Omega\times\mathbf{W}$) and the centrifugal force($\Omega\times\Omega\times\mathbf{r}$). To improve computational efficiency and accuracy, the Navier-Stokes equations are transformed from the physical space to the computational space.

The Navier-Stokes equations can be written in a conservative form in a rotating frame as follows;

$$\frac{\partial\rho}{\partial t}+\frac{\partial\rho u_k}{\partial x_k}=0 \tag{2.1}$$

$$\frac{\partial\rho u_i}{\partial t}+\frac{\partial\rho u_i u_k}{\partial x_k}=-\frac{\partial p}{\partial x_i}+\frac{\partial\tau_{ik}}{\partial x_k}+S_i \tag{2.2}$$

$$\frac{\partial\rho e}{\partial t}+\frac{\partial(\rho e+p)u_k}{\partial x_k}=\frac{\partial(\tau_{ik}u_i+q_k)}{\partial x_k} \tag{2.3}$$

$$p=\rho RT \tag{2.4}$$

$$\rho e=\frac{p}{\gamma-1}+\frac{1}{2}\rho(W^2-\Omega^2r^2) \tag{2.5}$$

where R is the gas constant and γ is the specific heat ratio of the working fluid. S_i is the source term added due to the rotor rotation and can be given as

$$\begin{pmatrix} S_x \\ S_y \\ S_z \end{pmatrix} = \begin{pmatrix} 0 \\ \rho\Omega^2 y + 2\rho\Omega w \\ \rho\Omega^2 z - 2\rho\Omega v \end{pmatrix} \tag{2.6}$$

2.1.1 Spatially Filtered NS Equations in Rotating Frame

The Navier-Stokes equations through Eq. (2.1) - Eq. (2.5) are considered to be able to directly solve engineering turbulent flows. However, such a direct numerical simulation has largely been limited to simple geometries at low Reynolds number since in general it requires a tremendous mesh and very small temporal scale, for example grid points $\simeq Re^{9/4}$ and times steps $\simeq Re^{3/4}$ to resolve all scales of turbulence [67].

Since turbulence consists of random fluctuations of the various flow properties, the statistical approach such as time, spatial or ensemble averaging is usually more meaningful in engineering practice. The spatial filtering eliminates the small scale high frequency components of the fluid motion, while keeping the unsteadiness associated with the large scale turbulent motion [68]. For an arbitrary function $u(x_i, t)$, the filtered variable $\bar{u}(x_i, t)$ is defined as:

$$\bar{u}(x_i, t) = \int_D G(x_i - \xi_i, \Delta) u(\xi_i, t) d\xi_i \tag{2.7}$$

where G is the filter function and Δ is the filter width and is associated with the mesh size. Similar to the case of RANS, for compressible flows, it is convenient to introduce the Favre-filtered variable $\tilde{u}(x_i, t)$ as:

$$\tilde{u}(x_i, t) = \frac{\overline{\rho u}}{\bar{\rho}} \tag{2.8}$$

A variable can be thus decomposed into its Favre-filtered component and fluctuating component as:

$$u(x_i, t) = \tilde{u}(x_i, t) + u''(x_i, t) \tag{2.9}$$

The molecular viscous stress tensor, $\bar{\tau}$ is estimated as:

$$\bar{\tau}_{ij} = \frac{2}{3}\tilde{\mu}\frac{\partial \tilde{u}_k}{\partial x_{\ k}}\delta_{ij} + \mu(\frac{\partial \tilde{u}_i}{\partial x_j} + \frac{\partial \tilde{u}_j}{\partial x_i}), \qquad i, j = 1, 2, 3 \tag{2.10}$$

The above equation is in the tensor form, where the subscript 1, 2, 3 represent the coordinates, x, y, z and the Einstein summation convention is used. The molecular viscosity $\tilde{\mu} = \tilde{\mu}(\tilde{T})$ is determined by Sutherland law.

The σ is the subgrid scale stress tensor due to the filtering process and is expressed as:

$$\sigma_{ij} = -\bar{\rho}(\widetilde{u_i u_j} - \tilde{u}_i \tilde{u}_j) \tag{2.11}$$

The energy flux Q is expressed as:

$$Q_i = \tilde{u}_j(\bar{\tau}_{ij} + \sigma_{ij}) - \bar{q}_i + \Phi_i \tag{2.12}$$

where Φ is the subscale heat flux:

$$\Phi_i = -C_p\bar{\rho}(\widetilde{u_i T} - \tilde{u}_i \tilde{T}) \tag{2.13}$$

The $\bar{q}_i$ is the molecular heat flux:

$$\bar{q}_i = -\frac{C_p\tilde{\mu}}{Pr}\frac{\partial\tilde{T}}{\partial x_i} \tag{2.14}$$

$$\bar{\rho}\tilde{e} = \frac{\bar{p}}{(\gamma-1)} + \frac{1}{2}\bar{\rho}(\tilde{u}^2 + \tilde{v}^2 + \tilde{w}^2 - \Omega^2 r^2) + \rho k \tag{2.15}$$

where γ is the ratio of specific heats, ρk is the subscale kinetic energy per unit volume.

$$\rho k = \frac{1}{2}\bar{\rho}(\widetilde{u_i u_i} - \tilde{u}_i\tilde{u}_i) = -\frac{1}{2}\sigma_{ii} \tag{2.16}$$

In the current simulations, the ρk in Eq.(2.15) is omitted based on the assumption that the effect is small.

Applying above definitions for the Navier-Stokes equations through Eq. (2.1) - Eq. (2.5) and using the eddy viscosity concept, then the shear stress $\bar{\tau}_{ik}$ and total heat flux $\bar{q}_k$ can be expressed in Cartesian coordinates as follows:

$$\bar{\tau}_{ik} = (\mu + \mu_{SA})\left[\left(\frac{\partial\tilde{u}_i}{\partial x_k} + \frac{\partial\tilde{u}_k}{\partial x_i}\right) - \frac{2}{3}\delta_{ik}\frac{\partial\tilde{u}_j}{\partial x_j}\right] \tag{2.17}$$

$$\bar{q}_k = -\left(\frac{\mu}{Pr} + \frac{\mu_{SA}}{Pr_t}\right)\frac{\partial\tilde{T}}{\partial x_k} \tag{2.18}$$

Note that μ_{SA} is obtained by the Spalart-Allmaras (SA) closure model for turbulence [69, 70] in this study. Sutherland's law is used to model the molecular viscosity μ.

$$\frac{\mu}{\mu_\infty} = (\frac{T}{T_\infty})^{1.5}\frac{T + 110K}{T + T_\infty} \tag{2.19}$$

where the subscript ∞ represents the condition at a reference point. A constant Prandtl number is given to determine thermal conductivity of fluid.

For simplicity, all the bar and tilde in above equations will be dropped for the rest of the thesis.

2.1.2 Nondimensionalization of the Governing Equations

The flow governing equations are normalized by a characteristic dimension L and freestream conditions.

$$\begin{aligned} t^* = \tfrac{tV_\infty}{L}, \quad x^* = \tfrac{x}{L}, \quad y^* = \tfrac{y}{L}, \quad z^* = \tfrac{z}{L} \\ \mu^* = \tfrac{\mu}{\mu_\infty}, \quad u^* = \tfrac{u}{V_\infty}, \quad v^* = \tfrac{v}{V_\infty}, \quad w^* = \tfrac{w}{V_\infty} \\ \rho^* = \tfrac{\rho}{\rho_\infty}, \quad T^* = \tfrac{T}{T_\infty}, \quad p^* = \tfrac{p}{\rho_\infty V_\infty^2}, \quad e^* = \tfrac{e}{V_\infty^2} \end{aligned} \tag{2.20}$$

As the nondimensional numbers introduced in this study, Reynolds number Re, Mach number M, and Rossby number R_o are defined as

$$Re = \frac{\rho_\infty L V_\infty}{\mu_\infty} \tag{2.21}$$

$$M_\infty = \frac{V_\infty}{\sqrt{\gamma R T_\infty}} \tag{2.22}$$

$$R_o = \frac{\Omega L}{V_\infty} \tag{2.23}$$

Above normalization results in

$$\mu^* = \frac{\mu}{\mu_\infty} = \frac{\mu Re}{\rho_\infty L V_\infty} \tag{2.24}$$

$$\mu^* = (T^*)^{1.5} \frac{T^* + 110/T_\infty}{T^* + 1} \tag{2.25}$$

$$p^* = \frac{\rho^* T^*}{\gamma M_\infty^2} \tag{2.26}$$

$$\rho^* e^* = \frac{P^*}{\gamma - 1} + \frac{1}{2}\rho^*(u^{*2} + v^{*2} + w^{*2} - {R_o}^2 r^{*2}) \tag{2.27}$$

For simplicity, the superscript asterisk will be dropped for the rest of the thesis. The normalized filtered compressible Navier-Stokes(NS) equations in Cartesian coordinates in a rotating frame can be expressed in a conservative flux vector form as

$$\frac{\partial \mathbf{Q}}{\partial t}+\frac{\partial \mathbf{E}}{\partial x}+\frac{\partial \mathbf{F}}{\partial y}+\frac{\partial \mathbf{G}}{\partial z}=\frac{1}{Re}(\frac{\partial \mathbf{E_v}}{\partial x}+\frac{\partial \mathbf{F_v}}{\partial y}+\frac{\partial \mathbf{G_v}}{\partial z})+S_R \tag{2.28}$$

where S_R is the source term appeared due to the rotor rotation. The variable vector **Q**, inviscid flux vectors **E**, **F**, **G**, and the viscous fluxes $\mathbf{E_v}$, $\mathbf{F_v}$, $\mathbf{G_v}$are given as the following.

$$\mathbf{Q}=\begin{pmatrix}\rho\\ \rho u\\ \rho v\\ \rho w\\ \rho e\end{pmatrix} \tag{2.29}$$

$$\mathbf{E}=\begin{pmatrix}\rho u\\ \rho u^2+p\\ \rho uv\\ \rho uw\\ (\rho e+p)u\end{pmatrix},\ \mathbf{F}=\begin{pmatrix}\rho v\\ \rho vu\\ \rho v^2+p\\ \rho vw\\ (\rho e+p)v\end{pmatrix},\ \mathbf{G}=\begin{pmatrix}\rho w\\ \rho wu\\ \rho wv\\ \rho w^2+p\\ (\rho e+p)w\end{pmatrix} \tag{2.30}$$

$$\mathbf{E_v}=\begin{pmatrix}0\\ \tau_{xx}\\ \tau_{xy}\\ \tau_{xz}\\ u_k\tau_{xk}-q_x\end{pmatrix},\ \mathbf{F_v}=\begin{pmatrix}0\\ \tau_{yx}\\ \tau_{yy}\\ \tau_{yz}\\ u_k\tau_{yk}-q_y\end{pmatrix},\ \mathbf{G_v}=\begin{pmatrix}0\\ \tau_{zx}\\ \tau_{zy}\\ \tau_{zz}\\ u_k\tau_{zk}-q_z\end{pmatrix} \tag{2.31}$$

$$S_R = \begin{pmatrix} 0 \\ 0 \\ \rho R_o^2 y + 2\rho R_o w \\ \rho R_o^2 z - 2\rho R_o v \\ 0 \end{pmatrix} \tag{2.32}$$

where

$$\tau_{ik} = (\mu + \mu_{SA} Re)[\frac{\partial u_i}{\partial x_k} + \frac{\partial u_k}{\partial x_i} - \frac{2}{3}\delta_{ik}\frac{\partial u_j}{\partial x_j}] \tag{2.33}$$

$$q_j = -\frac{1}{(\gamma - 1)M_\infty^2}(\frac{\mu}{Pr} + \frac{\mu_{SA} Re}{Pr_t})\frac{\partial T}{\partial x_j} \tag{2.34}$$

2.1.3 Transformation of the Navier-Stokes Equations

A transformation of the governing equations from the physical space(x, y, z) to the computational space(ξ, η, ζ) is performed to have an equally spaced rectangular grid system in the computational domain.

In generalized coordinates, Eq.(2.28) can be expressed as the following:

$$\frac{\partial \mathbf{Q}'}{\partial t} + \frac{\partial \mathbf{E}'}{\partial \xi} + \frac{\partial \mathbf{F}'}{\partial \eta} + \frac{\partial \mathbf{G}'}{\partial \zeta} = \frac{1}{\mathrm{Re}}\left(\frac{\partial \mathbf{E}'_\mathbf{v}}{\partial \xi} + \frac{\partial \mathbf{F}'_\mathbf{v}}{\partial \eta} + \frac{\partial \mathbf{G}'_\mathbf{v}}{\partial \zeta}\right) + \mathbf{S}'_\mathbf{R} \tag{2.35}$$

where

$$\mathbf{Q}' = \frac{\mathbf{Q}}{J} \tag{2.36}$$

$$\mathbf{E}' = \frac{1}{J}(\xi_t \mathbf{Q} + \xi_x \mathbf{E} + \xi_y \mathbf{F} + \xi_z \mathbf{G}) \tag{2.37}$$

$$\mathbf{F}' = \frac{1}{J}(\eta_t \mathbf{Q} + \eta_x \mathbf{E} + \eta_y \mathbf{F} + \eta_z \mathbf{G}) \tag{2.38}$$

$$\mathbf{G}' = \frac{1}{J}(\zeta_t \mathbf{Q} + \zeta_x \mathbf{E} + \zeta_y \mathbf{F} + \zeta_z \mathbf{G}) \tag{2.39}$$

$$\mathbf{E}'_\mathbf{v} = \frac{1}{J}(\xi_x \mathbf{E}_\mathbf{v} + \xi_y \mathbf{F}_\mathbf{v} + \xi_z \mathbf{G}_\mathbf{v}) \tag{2.40}$$

$$\mathbf{F'_v} = \frac{1}{J}(\eta_x \mathbf{E_v} + \eta_y \mathbf{F_v} + \eta_z \mathbf{G_v}) \tag{2.41}$$

$$\mathbf{G'_v} = \frac{1}{J}(\zeta_x \mathbf{E_v} + \zeta_y \mathbf{F_v} + \zeta_z \mathbf{G_v}) \tag{2.42}$$

$$\mathbf{S'_R} = \frac{S_R}{J} \tag{2.43}$$

where $J$is the transformation Jacobian.

The inviscid fluxes in generalized coordinate system are expressed as:

$$\mathbf{E}' = \begin{bmatrix} \rho U \\ \rho u U + l_x p \\ \rho v U + l_y p \\ \rho w U + l_z p \\ (\rho e + p)\, U - l_t p \end{bmatrix}, \mathbf{F}' = \begin{bmatrix} \rho V \\ \rho u V + m_x p \\ \rho v V + m_y p \\ \rho w V + m_z p \\ (\rho e + p)\, V - m_t p \end{bmatrix}, \mathbf{G}' = \begin{bmatrix} \rho W \\ \rho u W + n_x p \\ \rho v W + n_y p \\ \rho w W + n_z p \\ (\rho e + p)\, W - n_t p \end{bmatrix}$$
(2.44)

where U, V and $W$are the contravariant velocities in ξ, η and ζ directions.

$$\begin{aligned} U &= l_t + \mathbf{l} \bullet \mathbf{V} = l_t + l_x u + l_y v + l_z w \\ V &= m_t + \mathbf{m} \bullet \mathbf{V} = m_t + m_x u + m_y v + m_z w \\ W &= n_t + \mathbf{n} \bullet \mathbf{V} = n_t + n_x u + n_y v + n_z w \end{aligned} \tag{2.45}$$

where $\mathbf{l}$, $\mathbf{m}$, $\mathbf{n}$ are the normal vectors on ξ, η, ζ surfaces with their magnitudes equal to the elemental surface area and pointing to the directions of increasing ξ, η, ζ.

$$\mathbf{l} = \frac{\nabla \xi}{J} d\eta d\zeta,\ \mathbf{m} = \frac{\nabla \eta}{J} d\xi d\zeta,\ \mathbf{n} = \frac{\nabla \zeta}{J} d\xi d\eta \tag{2.46}$$

$$l_t = \frac{\xi_t}{J} d\eta d\zeta,\ m_t = \frac{\eta_t}{J} d\xi d\zeta,\ n_t = \frac{\zeta_t}{J} d\xi d\eta \tag{2.47}$$

where $d\xi = d\eta = d\zeta = 1$ in the current discretization. When the gird is stationary, $l_t = m_t = n_t = 0$.

2.1.4 Spalart-Allmaras Turbulence Closure Model

The Spalart-Allmaras (S-A) one equation model [71] solves a transport equation for the working variable $\tilde{\nu}$ related to the turbulent eddy ν. Using the normalization given in Eq. (2.20), the nondimensionalized S-A model including closure coefficients and damping functions is written in terms of eddy viscosity ν_t as follows.

Turbulent Eddy Viscosity:

$$\mu_{SA} = \rho \nu_t = \rho \tilde{\nu} f_{v1} \tag{2.48}$$

Eddy Viscosity Equation:

$$\begin{aligned} \tfrac{\partial \bar{\rho}\bar{\tilde{\nu}}}{\partial \bar{t}} + \bar{\nabla} \cdot \left(\bar{\rho}\bar{\tilde{\nu}}\bar{\vec{V}}\right) \quad &= \tfrac{1}{Re}\bar{\nabla} \cdot \left[\tfrac{\bar{\rho}}{\sigma}(\bar{\nu} + \bar{\tilde{\nu}})\bar{\nabla}\bar{\tilde{\nu}}\right] + \bar{\rho} c_{b1}\left(1 - f_{t2}\right)\left(\bar{S} + \tfrac{1}{Re}\tfrac{\bar{\tilde{\nu}}}{\kappa^2 \bar{d}^2} f_{v2}\right)\bar{\tilde{\nu}} - \\ &\tfrac{1}{Re}\bar{\rho}\left(c_{w1} f_w - \tfrac{c_{b1}}{\kappa^2} f_{t2}\right)\left(\tfrac{\bar{\tilde{\nu}}}{\bar{d}}\right)^2 - \tfrac{1}{Re}\tfrac{1}{\sigma}\left(\bar{\nu} + \bar{\tilde{\nu}}\right)\bar{\nabla}\bar{\tilde{\nu}} \cdot \bar{\nabla}\bar{\rho} + \\ &\tfrac{1}{Re}\tfrac{\bar{\rho}}{\sigma} c_{b2}\left(\bar{\nabla}\bar{\tilde{\nu}}\right)^2 + Re\bar{\rho} f_{t1}\left(\Delta\bar{q}\right)^2 \end{aligned}$$

(2.49)

Closure Coefficients:

$$c_{b1} = 0.1355, c_{b2} = 0.622, \sigma = \tfrac{2}{3}, c_{w1} = \tfrac{c_{b1}}{k^2} + \tfrac{1 + c_{b2}}{\sigma}$$

$$c_{w2} = 0.3, c_{w3} = 2, k = 0.41, c_{v1} = 7.1, c_{t1} = 1.0, c_{t2} = 2.0, c_{t3} = 1.1, c_{t4} = 2.0$$

(2.50)

Auxiliary Relations:

$$\chi = \frac{\tilde{\nu}}{\nu}, \quad g = r + c_{w2}(r^6 - r), \quad r = \frac{\tilde{\nu}}{Re\tilde{S}k^2 d^2} \tag{2.51}$$

$$f_{v1} = \frac{\chi^3}{\chi^3 + c_{v1}^3}, \quad f_{v2} = 1 - \frac{\chi}{1 + \chi f_{v1}}, \quad f_w = g(\frac{1 + c_{w3}^6}{g^6 + c_{w3}^6})^{1/6} \tag{2.52}$$

$$\tilde{S} = S + \frac{\tilde{\nu}}{Rek^2 d^2} f_{v2}, \quad S = \sqrt{2\omega_{ij}\omega_{ij}}, \quad g_t = min\left(0.1, \frac{\Delta q}{\omega_t \Delta x_t}\right) \tag{2.53}$$

$$f_{t2} = c_{t3} exp\left(-c_{t4}\chi^2\right), \quad f_{t1} = c_{t1} g_t exp\left[-c_{t2}\frac{\omega_t^2}{\Delta U^2}\left(d^2 + g_t^2 d_t^2\right)\right] \tag{2.54}$$

Where $\omega_{ij} = \frac{1}{2}\left(\frac{\partial u_i}{\partial x_j} - \frac{\partial u_j}{\partial x_i}\right)$ is the fluid particle angular velocity tensor. ω_t is the wall vorticity at the wall boundary layer trip location, d is the distance to the closest wall, d_t is the distance of the field point to the trip location, Δq is the difference of the velocities between the field point and the trip location, Δx_t is the grid spacing along the wall at the trip location.

To couple the SA model with Eq. (2.35), the eddy viscosity equation (2.49) is also transformed to the computational space and can be expressed in the generalized coordinate system as

$$\begin{aligned} \frac{\partial \frac{1}{J}\rho\tilde{\nu}}{\partial t} + \frac{\partial \rho\tilde{\nu}U}{\partial \xi} + \frac{\partial \rho\tilde{\nu}V}{\partial \eta} + \frac{\partial \rho\tilde{\nu}W}{\partial \zeta} &= \frac{1}{Re}\left(\frac{\partial \frac{\rho}{\sigma}\left(\nu + \tilde{\nu}\right)\left(\mathbf{l} \bullet \nabla\tilde{\nu}\right)}{\partial \xi}\right. \\ &\left. + \frac{\partial \frac{\rho}{\sigma}\left(\nu + \tilde{\nu}\right)\left(\mathbf{m} \bullet \nabla\tilde{\nu}\right)}{\partial \eta} + \frac{\partial \frac{\rho}{\sigma}\left(\nu + \tilde{\nu}\right)\left(\mathbf{n} \bullet \nabla\tilde{\nu}\right)}{\partial \zeta} + \frac{1}{J}S_\nu\right) \end{aligned} \tag{2.55}$$

where

$$\begin{aligned} S_\nu = \rho c_{b1}\left(1 - f_{t2}\right)\tilde{S}\tilde{\nu} + \tfrac{1}{Re}\Big[-\rho\left(c_{w1}f_w - \tfrac{c_{b1}}{\kappa^2}f_{t2}\right)\left(\tfrac{\tilde{\nu}}{d}\right)^2 \\ + \tfrac{\rho}{\sigma}c_{b2}\left(\nabla\tilde{\nu}\right)^2 - \tfrac{1}{\sigma}\left(\nu + \tilde{\nu}\right)\nabla\tilde{\nu} \bullet \nabla\rho\Big] + Re\left[\rho f_{t1}\left(\Delta q\right)^2\right] \end{aligned} \tag{2.56}$$

In summary, the spatially filtered Navier-Stokes equations with the SA model turbulence closure in a rotating frame of reference in the generalized coordinates(ξ, η, ζ) can be written in a conservative form as the following:

$$\frac{\partial \mathbf{Q}}{\partial t} + \frac{\partial \mathbf{E}}{\partial \xi} + \frac{\partial \mathbf{F}}{\partial \eta} + \frac{\partial \mathbf{G}}{\partial \zeta} = \frac{1}{Re}\left(\frac{\partial \mathbf{R}}{\partial \xi} + \frac{\partial \mathbf{S}}{\partial \eta} + \frac{\partial \mathbf{T}}{\partial \zeta}\right) + \mathbf{D} \tag{2.57}$$

where

$$\mathbf{Q} = \frac{1}{J}\begin{bmatrix} \rho \\ \rho u \\ \rho v \\ \rho w \\ \rho e \\ \rho\tilde{\nu} \end{bmatrix} \tag{2.58}$$

$$\mathbf{E} = \begin{bmatrix} \rho U \\ \rho u U + l_x p \\ \rho v U + l_y p \\ \rho w U + l_z p \\ (\rho e + p)\, U - l_t p \\ \rho\tilde{\nu} U \end{bmatrix}, \mathbf{F} = \begin{bmatrix} \rho V \\ \rho u V + m_x p \\ \rho v V + m_y p \\ \rho w V + m_z p \\ (\rho e + p)\, V - m_t p \\ \rho\tilde{\nu} V \end{bmatrix}, \mathbf{G} = \begin{bmatrix} \rho W \\ \rho u W + n_x p \\ \rho v W + n_y p \\ \rho w W + n_z p \\ (\rho e + p)\, W - n_t p \\ \rho\tilde{\nu} W \end{bmatrix} \tag{2.59}$$

$$\mathbf{R} = \begin{bmatrix} 0 \\ l_k \tau_{xk} \\ l_k \tau_{yk} \\ l_k \tau_{zk} \\ l_k(u_i \tau_{ik} - q_k) \\ \frac{\rho}{\sigma}\left(\nu + \tilde{\nu}\right)\left(\mathbf{l} \bullet \nabla\tilde{\nu}\right) \end{bmatrix}, \mathbf{S} = \begin{bmatrix} 0 \\ m_k \tau_{xk} \\ m_k \tau_{yk} \\ m_k \tau_{zk} \\ m_k(u_i \tau_{ik} - q_k) \\ \frac{\rho}{\sigma}\left(\nu + \tilde{\nu}\right)\left(\mathbf{m} \bullet \nabla\tilde{\nu}\right) \end{bmatrix}, \mathbf{T} = \begin{bmatrix} 0 \\ n_k \tau_{xk} \\ n_k \tau_{yk} \\ n_k \tau_{zk} \\ n_k(u_i \tau_{ik} - q_k) \\ \frac{\rho}{\sigma}\left(\nu + \tilde{\nu}\right)\left(\mathbf{n} \bullet \nabla\tilde{\nu}\right) \end{bmatrix} \tag{2.60}$$

$$\mathbf{D} = \frac{1}{J}\begin{bmatrix} 0 \\ 0 \\ \rho R_o^2 y + 2\rho R_o w \\ \rho R_o^2 z - 2\rho R_o v \\ 0 \\ \frac{S_\nu}{Re} \end{bmatrix} \tag{2.61}$$

where

$$\tau_{ik} = (\mu + \mu_{SA} Re)[\frac{\partial u_i}{\partial x_k} + \frac{\partial u_k}{\partial x_i} - \frac{2}{3}\delta_{ik}\frac{\partial u_j}{\partial x_j}] \tag{2.62}$$

$$q_k = -\frac{1}{(\gamma - 1)M_\infty^2}(\frac{\mu}{Pr} + \frac{\mu_{SA} Re}{Pr_t})\frac{\partial T}{\partial x_k} \tag{2.63}$$

2.2 Numerical Methodology

An implicit finite difference discretization for the flow governing equations is described. The inviscid fluxes are discretized using a low diffusion E-CUSP scheme [64]. The structure governing equations are discretized and solved implicitly in the same manner to be consistent with the flow governing equations.

2.2.1 Implicit Discretization

Let $J = \frac{1}{\Delta V}$, then 3D Navier-Stokes equations (2.57) is rewritten in a conservative flux vector form as

$$\frac{\partial \Delta V \mathbf{Q}}{\partial t} + \frac{\partial(\mathbf{E} - \mathbf{R}')}{\partial \xi} + \frac{\partial(\mathbf{F} - \mathbf{S}')}{\partial \eta} + \frac{\partial(\mathbf{G} - \mathbf{T}')}{\partial \zeta} = \Delta V \mathbf{D} \tag{2.64}$$

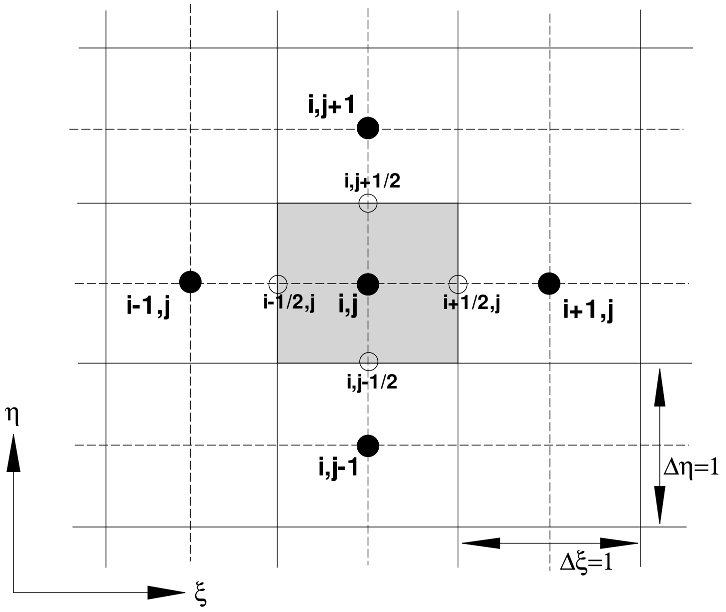

Figure 2.1: Discretization domain indicating the cell center(i,j)

where ΔV denotes the volume of the cell and $\mathbf{R}' = \mathbf{R}/Re$, $\mathbf{S}' = \mathbf{S}/Re$, $\mathbf{T}' = \mathbf{T}/Re$. For steady state solutions, the governing equation will be elliptic type at subsonic and hyperbolic at supersonic. This will make it difficult to discretize the Navier-Stokes equations using a consistent scheme. The temporal term is thus included for steady state solutions to keep the governing equations to have the same hyperbolic type across Mach number 1. For steady state solution, the accuracy of the temporal term is irrelevant since it must be zero when it is converged. Hence, the temporal term is discretized using first order Euler method for its simplicity. The discretized temporal term becomes

$$\frac{\Delta V(\mathbf{Q}^{n+1}-\mathbf{Q}^{n})}{\Delta t}+[\frac{\partial(\mathbf{E}-\mathbf{R}')}{\partial\xi}]^{n+1}+[\frac{\partial(\mathbf{F}-\mathbf{S}')}{\partial\eta}]^{n+1}+[\frac{\partial(\mathbf{G}-\mathbf{T}')}{\partial\zeta}]^{n+1}=\Delta V\mathbf{D}^{n+1}$$

(2.65)

where n and $n+1$ are two sequential time levels, which have a time interval of Δt. Eq. (2.65) can be further discretized in space using a conservative differencing as the following:

$$\begin{aligned}
&\tfrac{\Delta V_{ijk}(\mathbf{Q}_{ijk}^{n+1}-\mathbf{Q}_{ijk}^{n})}{\Delta t}\\
&+(\mathbf{E}_{i+\frac{1}{2}}-\mathbf{E}_{i-\frac{1}{2}})^{n+1}-(\mathbf{R}'_{i+\frac{1}{2}}-\mathbf{R}'_{i-\frac{1}{2}})^{n+1}\\
&+(\mathbf{F}_{j+\frac{1}{2}}-\mathbf{F}_{j-\frac{1}{2}})^{n+1}-(\mathbf{S}'_{j+\frac{1}{2}}-\mathbf{S}'_{j-\frac{1}{2}})^{n+1}\\
&+(\mathbf{G}_{k+\frac{1}{2}}-\mathbf{G}_{k-\frac{1}{2}})^{n+1}-(\mathbf{T}'_{k+\frac{1}{2}}-\mathbf{T}'_{k-\frac{1}{2}})^{n+1}\\
&=\Delta V_{ijk}\mathbf{D}_{ijk}^{n+1}
\end{aligned} \tag{2.66}$$

To evaluate the inviscid fluxes at the cell interface $\mathbf{E},\mathbf{F},\mathbf{G}$, the characteristic based upwind schemes are usually employed due to importance of capturing strong shocks and careful treatment of discontinuity, while the central differencing is used for the viscous fluxes $\mathbf{R},\mathbf{S},\mathbf{T}$. For implicit methods, a Jacobian must be introduced at time level $n+1$ for linearization. This Jacobian is formed by the derivatives of the flux values with respect to each conservative variables at a cell center point.

The implicit matrices will result in 9 elements around the diagonal element for 3D with first order upwind for inviscid fluxes and second order central differencing scheme. The first order upwind scheme for the implicit matrix will have the diagonal dominance required by Gauss-Seidel iteration [72]. Using Gauss-Seidel line relaxation, a block tri-diagonal matrix is inversed along each mesh line.

With an upwind scheme, the numerical flux is split into its left(L) and right(R) side fluxes. For example, the inviscid flux $\mathbf{E}$ at $i+\frac{1}{2}$ can be expressed as

$$\mathbf{E}_{i+\frac{1}{2}} = \mathbf{E}_L + \mathbf{E}_R = \mathbf{E}^+_{i+\frac{1}{2}} + \mathbf{E}^-_{i+\frac{1}{2}} \tag{2.67}$$

Since Eq. (2.64) is nonlinear, a linearization procedure is necessary. Let us apply a Taylor series expansion to the flux vectors at time level $n+1$ as

$$\mathbf{E}^{n+1} \cong \mathbf{E}^n + \frac{\partial \mathbf{E}}{\partial t}\Delta t + O[(\Delta t)^2] \tag{2.68}$$

$$\frac{\partial \mathbf{E}}{\partial t} = \frac{\partial \mathbf{E}}{\partial \mathbf{Q}}\frac{\partial \mathbf{Q}}{\partial t} \cong \frac{\partial \mathbf{E}}{\partial \mathbf{Q}}\frac{\Delta \mathbf{Q}}{\Delta t} \tag{2.69}$$

$$\mathbf{E}^{n+1} \cong \mathbf{E}^n + A \bullet \Delta \mathbf{Q} \tag{2.70}$$

where $A(=\frac{\partial \mathbf{E}}{\partial \mathbf{Q}})$ is the inviscid flux Jacobian matrix and the change in the conservative variable vector, $\Delta \mathbf{Q}$, is defined by

$$\Delta \mathbf{Q} = \mathbf{Q}^{n+1} - \mathbf{Q}^n \tag{2.71}$$

The inviscid flux $\mathbf{E}$ at the cell interface $i+\frac{1}{2}$ can be given as

$$\mathbf{E}^{n+1}_{i+\frac{1}{2}} = \mathbf{E}^n_{i+\frac{1}{2}} + (\tfrac{\partial \mathbf{E}^+}{\partial \mathbf{Q}})_L \bullet \Delta \mathbf{Q}_L + (\tfrac{\partial \mathbf{E}^-}{\partial \mathbf{Q}})_R \bullet \Delta \mathbf{Q}_R \tag{2.72}$$

where $\Delta \mathbf{Q}$ approaches zero when it is converged. Hence the accuracy order for $\Delta \mathbf{Q}$ is not important. The first order accuracy is used to evaluate $\Delta \mathbf{Q}$.

$$\Delta \mathbf{Q}_L = \Delta \mathbf{Q}_i, \quad \Delta \mathbf{Q}_R = \Delta \mathbf{Q}_{i+1} \tag{2.73}$$

Let

$$A^L_{i+\frac{1}{2}} = (\frac{\partial \mathbf{E}^+}{\partial \mathbf{Q}})_L, \quad A^R_{i+\frac{1}{2}} = (\frac{\partial \mathbf{E}^-}{\partial \mathbf{Q}})_R \tag{2.74}$$

Then,

$$\mathbf{E}^{n+1}_{i+\frac{1}{2}} = \mathbf{E}^n_{i+\frac{1}{2}} + A^L_{i+\frac{1}{2}}\Delta \mathbf{Q}_i + A^R_{i+\frac{1}{2}}\Delta \mathbf{Q}_{i+1} \tag{2.75}$$

Thus,

$$\begin{gathered}\mathbf{E}^{n+1}_{i+\frac{1}{2}} - \mathbf{E}^{n+1}_{i-\frac{1}{2}} = \\ (\mathbf{E}^{n}_{i+\frac{1}{2}} - \mathbf{E}^{n}_{i-\frac{1}{2}}) + A^{R}_{i+\frac{1}{2}}\Delta\mathbf{Q}_{i+1} + (A^{L}_{i+\frac{1}{2}} - A^{R}_{i-\frac{1}{2}})\Delta\mathbf{Q}_{i} - A^{L}_{i-\frac{1}{2}}\Delta\mathbf{Q}_{i-1}\end{gathered} \tag{2.76}$$

The viscous fluxes are linearized using central differencing.

$$\begin{aligned}(\mathbf{R}'_{i+\frac{1}{2}})^{n+1} &= (\mathbf{R}'_{i+\frac{1}{2}})^{n} + \frac{\partial\mathbf{R}'_{i+\frac{1}{2}}}{\partial\mathbf{Q}_{i+1}}\Delta\mathbf{Q}_{i+1} + \frac{\partial\mathbf{R}'_{i+\frac{1}{2}}}{\partial\mathbf{Q}_{i}}\Delta\mathbf{Q}_{i} \\ &= (\mathbf{R}'_{i+\frac{1}{2}})^{n} + L^{R}_{i+\frac{1}{2}}\Delta\mathbf{Q}_{i+1} + L^{L}_{i+\frac{1}{2}}\Delta\mathbf{Q}_{i}\end{aligned} \tag{2.77}$$

Thus,

$$\begin{gathered}(\mathbf{R}'_{i+\frac{1}{2}})^{n+1} - (\mathbf{R}'_{i-\frac{1}{2}})^{n+1} = \\ (\mathbf{R}'_{i+\frac{1}{2}})^{n} - (\mathbf{R}'_{i-\frac{1}{2}})^{n} + L^{R}_{i+\frac{1}{2}}\Delta\mathbf{Q}_{i+1} + (L^{L}_{i+\frac{1}{2}} - L^{R}_{i-\frac{1}{2}})\Delta\mathbf{Q}_{i} - L^{L}_{i-\frac{1}{2}}\Delta\mathbf{Q}_{i-1}\end{gathered} \tag{2.78}$$

The source term can be linearized by

$$\mathbf{D}^{n+1}_{i,j,k} \cong \mathbf{D}^{n}_{i,j,k} + (\frac{\partial\mathbf{D}}{\partial\mathbf{Q}})_{i,j,k} \bullet \Delta\mathbf{Q}_{i,j,k} \tag{2.79}$$

To apply above linearization to the fluxes in η and ζ direction, then the integrated governing equations are written as

$$\begin{gathered}(I-\Theta)\Delta\mathbf{Q}_{i,j,k} + \hat{A}^{+}\Delta\mathbf{Q}_{i+1,j,k} + \hat{A}\Delta\mathbf{Q}_{i,j,k} + \hat{A}^{-}\Delta\mathbf{Q}_{i-1,j,k} \\ +\hat{B}^{+}\Delta\mathbf{Q}_{i,j+1,k} + \hat{B}\Delta\mathbf{Q}_{i,j,k} + \hat{B}^{-}\Delta\mathbf{Q}_{i,j-1,k} \\ +\hat{C}^{+}\Delta\mathbf{Q}_{i,j,k+1} + \hat{C}\Delta\mathbf{Q}_{i,j,k} + \hat{C}^{-}\Delta\mathbf{Q}_{i,j,k-1} = \mathbf{RHS}^{n}\end{gathered} \tag{2.80}$$

where $\Theta = \Delta t \bullet (\frac{\partial\mathbf{D}}{\partial\mathbf{Q}})^{n}_{i,j,k}$. The coefficients A, A^{+}, A^{-}, B, B^{+}, B^{-}, and C, C^{+}, C^{-} are called the left hand side (LHS) coefficient matrices and given as

$$
\begin{aligned}
\hat{A}^{+} &= \tfrac{\Delta t}{\Delta V}(A^{R}_{i+\frac{1}{2}} - L^{R}_{i+\frac{1}{2}}) \\
\hat{A} &= \tfrac{\Delta t}{\Delta V}(A^{L}_{i+\frac{1}{2}} - L^{L}_{i+\frac{1}{2}} - A^{R}_{i-\frac{1}{2}} + L^{R}_{i-\frac{1}{2}}) \\
\hat{A}^{-} &= -\tfrac{\Delta t}{\Delta V}(A^{L}_{i-\frac{1}{2}} - L^{L}_{i-\frac{1}{2}}) \\
\hat{B}^{+} &= \tfrac{\Delta t}{\Delta V}(B^{R}_{j+\frac{1}{2}} - M^{R}_{j+\frac{1}{2}}) \\
\hat{B} &= \tfrac{\Delta t}{\Delta V}(B^{L}_{j+\frac{1}{2}} - M^{L}_{j+\frac{1}{2}} - B^{R}_{j-\frac{1}{2}} + M^{R}_{j-\frac{1}{2}}) \\
\hat{B}^{-} &= -\tfrac{\Delta t}{\Delta V}(B^{L}_{j-\frac{1}{2}} - M^{L}_{j-\frac{1}{2}}) \\
\hat{C}^{+} &= \tfrac{\Delta t}{\Delta V}(C^{R}_{k+\frac{1}{2}} - N^{R}_{k+\frac{1}{2}}) \\
\hat{C} &= \tfrac{\Delta t}{\Delta V}(C^{L}_{k+\frac{1}{2}} - N^{L}_{k+\frac{1}{2}} - C^{R}_{k-\frac{1}{2}} + N^{R}_{k-\frac{1}{2}}) \\
\hat{C}^{-} &= -\tfrac{\Delta t}{\Delta V}(C^{L}_{k-\frac{1}{2}} - N^{L}_{k-\frac{1}{2}})
\end{aligned}
\tag{2.81}
$$

In Eq. (2.80), $\mathbf{RHS}^n$ is the summation of all terms on the right hand side (RHS) of the discretized equation and written as

$$
\begin{aligned}
\mathbf{RHS}^n = -\tfrac{\Delta t}{\Delta V}[(\mathbf{E}_{i+\frac{1}{2}} - \mathbf{E}_{i-\frac{1}{2}})^n + (\mathbf{F}_{i+\frac{1}{2}} - \mathbf{F}_{i-\frac{1}{2}})^n + (\mathbf{G}_{i+\frac{1}{2}} - \mathbf{G}_{i-\frac{1}{2}})^n \\
-(\mathbf{R}'_{i+\frac{1}{2}} - \mathbf{R}'_{i-\frac{1}{2}})^n - (\mathbf{S}'_{i+\frac{1}{2}} - \mathbf{S}'_{i-\frac{1}{2}})^n - (\mathbf{T}'_{i+\frac{1}{2}} - \mathbf{T}'_{i-\frac{1}{2}})^n] + \Delta t \bullet \mathbf{D}^n
\end{aligned}
\tag{2.82}
$$

Since the delta formulation($\Delta\mathbf{Q}$), the left hand side (LHS) in Eq. (2.80) constructed by employing 1st order scheme, does not affect the final solution, the accuracy of the converged solution relies on the accuracy of $\mathbf{RHS}^n$. The 5th order WENO scheme with an efficient upwind Riemann solver, so called the low diffusion E-CUSP (LDE) scheme [64], is used to evaluate the interface inviscid fluxes in $\mathbf{RHS}^n$. A fully conservative 4th order central differencing scheme [58] is used to evaluate the viscous fluxes. The unfactored Gauss-Seidel line iteration method is adopted to solve the Eq. (2.80) because the diagonal dominance is achieved through the 1st order implicit discretization and it is shown to be the most efficient relaxation method for transonic flow simulation [73].

2.2.2 The Low Diffusion E-CUSP (LDE) Scheme

The Low Diffusion E-CUSP (LDE) Scheme [64] is used to evaluate the inviscid fluxes. The basic idea of the LDE scheme is to split the inviscid flux into the convective flux E^c and the pressure flux E^p based on the upwind characteristics. In generalized coordinate system, the flux $\mathbf{E}$ can be split as the following:

$$\mathbf{E}' = E^c + E^p = \begin{pmatrix} \rho U \\ \rho u U \\ \rho v U \\ \rho w U \\ \rho e U \\ \rho \tilde{\nu} U \end{pmatrix} + \begin{pmatrix} 0 \\ l_x p \\ l_y p \\ l_z p \\ p\overline{U} \\ 0 \end{pmatrix} \tag{2.83}$$

where, U is the contravariant velocity in ξ direction and is defined as the following:

$$U = l_t + l_x u + l_y v + l_z w \tag{2.84}$$

$\overline{U}$ is defined as:

$$\overline{U} = l_x u + l_y v + l_z w \tag{2.85}$$

The convective term, E^c is evaluated by

$$E^c = \rho U \begin{pmatrix} 1 \\ u \\ v \\ w \\ e \\ \tilde{\nu} \end{pmatrix} = \rho U f^c, \ f^c = \begin{pmatrix} 1 \\ u \\ v \\ w \\ e \\ \tilde{\nu} \end{pmatrix} \tag{2.86}$$

let

$$C = c\left(l_x^2 + l_y^2 + l_z^2\right)^{\frac{1}{2}} \tag{2.87}$$

where $c = \sqrt{\gamma RT}$ is the speed of sound.

Then the convective flux at interface $i + \frac{1}{2}$ is evaluated as:

$$E^c_{i+\frac{1}{2}} = C_{\frac{1}{2}}\left[\rho_L C^+ f^c_L + \rho_R C^- f^c_R\right] \tag{2.88}$$

where, the subscripts L and R represent the left and right hand sides of the interface. The Mach number splitting of Edwards [66] is borrowed to determine C^+ and C^-.

The pressure flux, E^p is evaluated as the following

$$E^p_{i+\frac{1}{2}} = \begin{pmatrix} 0 \\ \mathcal{P}^+ p\, l_x \\ \mathcal{P}^+ p\, l_y \\ \mathcal{P}^+ p\, l_z \\ \frac{1}{2} p \left[\overline{U} + \overline{C}_{\frac{1}{2}} \right] \\ 0 \end{pmatrix}_L + \begin{pmatrix} 0 \\ \mathcal{P}^- p\, l_x \\ \mathcal{P}^- p\, l_y \\ \mathcal{P}^- p\, l_z \\ \frac{1}{2} p \left[\overline{U} - \overline{C}_{\frac{1}{2}} \right] \\ 0 \end{pmatrix}_R \tag{2.89}$$

The contravariant speed of sound $\overline{C}$ in the pressure vector is consistent with $\overline{U}$. It is computed based on C as the following,

$$\overline{C} = C - l_t \tag{2.90}$$

The use of $\overline{U}$ and $\overline{C}$ instead of U and C in the pressure vector is to take into account of the grid speed so that the flux will transit from subsonic to supersonic smoothly. When the grid is stationary, $l_t = 0$, $\overline{C} = C$, $\overline{U} = U$.

The pressure splitting coefficient is:

$$\mathcal{P}^{\pm}_{L,R} = \frac{1}{4} \left(M_{L,R} \pm 1 \right)^2 \left(2 \mp M_L \right) \tag{2.91}$$

The LDE scheme can capture crisp shock profile and exact contact surface discontinuities as accurately as the Roe scheme [74]. With an extra equation from the SA turbulence model, the splitting is basically the same as the original scheme for the Euler equation.

The interface flux, $E_{i+\frac{1}{2}} = E(Q_L, Q_R)$, is evaluated by determining the conservative variables Q_L and Q_R using fifth-order WENO scheme [56, 57]. A set of fully conservative fourth-order accurate finite central differencing schemes for the viscous terms is employed in this research [58, 75].

2.2.3 Implicit Time Integration

When a unsteady solution is considered, higher order approximation for the time derivative is desirable. For unsteady flow, Jameson formulated so called the 2nd order dual time stepping scheme [76]. By introducing a pseudo time term, the unsteady problem at each physical time step is treated as a steady state problem for pseudo time. Without losing time accuracy, the dual time stepping scheme can greatly improve the computation efficiency by enhancing diagonal dominance [77].

2.2.3.1 Implicit Time Accurate Flow Solver

The time accurate governing equations are solved using dual time stepping method suggested by Jameson [76]. To achieve high convergence rate, the implicit pseudo time marching scheme is used with the unfactored Gauss-Seidel line relaxation [78]. The physical temporal term is discretized implicitly using a three point, backward differencing as the following:

$$\frac{\partial Q}{\partial t} = \frac{3Q^{n+1} - 4Q^{n} + Q^{n-1}}{2\Delta t} \tag{2.92}$$

where $n-1$, n and $n+1$ are three sequential time levels, which have a time interval of Δt. The first-order Euler scheme is used to discretize the pseudo temporal term to enhance diagonal dominance. The semi-discretized equations of the governing equations are finally given as the following:

$$\begin{aligned}&\left[\left(\tfrac{1}{\Delta\tau}+\tfrac{1.5}{\Delta t}\right)I-\left(\frac{\partial R}{\partial Q}\right)^{n+1,m}\right]\delta Q^{n+1,m+1}\\&=R^{n+1,m}-\tfrac{3Q^{n+1,m}-4Q^{n}+Q^{n-1}}{2\Delta t}\end{aligned}\tag{2.93}$$

where the $\Delta\tau$ is the pseudo time step, R is the net flux evaluated on a grid point using the fifth-order WENO scheme.

CHAPTER 3

Turbomachinery Boundary Conditions

The boundary conditions (BCs) for 3D multistage fan/compressor simulation are described in this chapter. Inlet boundary condition(BC), outlet BC, wall BC, circumferential phase-lagged BC with time shifted or Direct Store phase lag are given in detail. Unsteady rotor/stator sliding BCs are explained including treatment of algorithm for Full Annulus and Single-Passage simulations.

3.1 Cartesian and Cylindrical System Coordinate Mapping

It is convenient for turbomachinery to express the boundary conditions in Cylindrical system. Assuming the system is rotating about the x-axis, then θ and r denote the other two directions of the cylindrical system and can be defined as

$$\theta = tan^{-1}(\frac{z}{y}) \tag{3.1}$$

$$r = \sqrt{y^2 + z^2} \tag{3.2}$$

Coordinates mapping between the Cartesian (x, y, z) and Cylindrical system (x, θ, r) can be given as

$$\begin{pmatrix} V_x \\ V_\theta \\ V_r \end{pmatrix} = \begin{pmatrix} u \\ -v \cdot sin\theta + w \cdot cos\theta \\ v \cdot cos\theta + w \cdot sin\theta \end{pmatrix} = \begin{pmatrix} u \\ \frac{-v \cdot z + w \cdot y}{r} \\ \frac{v \cdot y + w \cdot z}{r} \end{pmatrix} \tag{3.3}$$

where u, v, and w are the relative velocity components in the x, y, and z coordinate directions respectively.

The absolute velocity components in Cylindrical coordinates (C_x, C_θ, C_r) are related to the relative velocity components(V_x, V_θ, V_r) via the rotor wheel speed$(r\Omega)$ as

$$\begin{pmatrix} C_x \\ C_\theta \\ C_r \end{pmatrix} = \begin{pmatrix} V_x \\ V_\theta + rR_o \\ V_r \end{pmatrix} \tag{3.4}$$

3.2 Rotor Inlet BC

At the rotor inlet, the radial distributions of total pressure P_o, total temperature T_o, swirl angle α and pitch angle β are specified. The velocity is taken from the computational domain by the extrapolation in order to determine the rest of variables. First, we assume that the speed of sound a is constant at the inlet boundary. Then, the static temperature is obtained by

$$T_b = T_o[1 - \frac{\gamma - 1}{2}(\frac{C_i}{a_o})^2] \tag{3.5}$$

where the subscripts i represents the first interior cell and subscripts b indicates the first ghost cell of the boundary. C_i is the absolute velocity of the first interior cell and a_o is the total speed of sound defined by

$$\frac{a_o^2}{\gamma-1} = \frac{a_i^2}{\gamma-1} + \frac{C_i^2}{2} \tag{3.6}$$

Using the isentropic relations, the absolute velocity(C_b), the static pressure(p_b) and density(ρ_b) are determined by

$$|C_b| = \frac{1}{M_\infty}\sqrt{\frac{2}{\gamma-1}\left(T_o - T_b\right)} \tag{3.7}$$

$$p_b = P_o\left(\tfrac{T_b}{T_o}\right)^{\frac{\gamma}{\gamma-1}} \tag{3.8}$$

$$\rho_b = \tfrac{p_b\gamma}{a_b^2} \tag{3.9}$$

Then, the velocity components are decoupled and the conservative variables are found as the following:

$$\begin{pmatrix} \rho \\ \rho V_x \\ \rho V_r \\ \rho V_\theta \\ \rho e \end{pmatrix}_b = \begin{pmatrix} \rho_b \\ \rho_b C_m cos\beta \\ \rho_b C_m sin\beta \\ \rho_b (C_m tan\alpha - rR_o) \\ \frac{p_b}{(\gamma-1)} + \frac{\rho_b}{2}(V_x^2 + V_r^2 + V_\theta^2 - r^2R_o^2) \end{pmatrix} \tag{3.10}$$

3.3 Rotor Outlet BC

At the rotor outlet, the static pressure(p_b) is specified. The components of velocity(u, v, w) are extrapolated from the computational domain. If we neglect the viscosity and constant density, the radial momentum equation can be written as

$$\frac{\partial V_r}{\partial t} + V_r \frac{\partial V_r}{\partial t} + \frac{V_\theta}{r} \frac{\partial V_r}{\partial \theta} + u \frac{\partial V_r}{\partial z} - \frac{V_\theta^2}{r} = -\frac{1}{\rho} \frac{\partial p}{\partial r} \tag{3.11}$$

The change in the radial velocity can be usually negligible($\partial V_r \cong 0$) in axial turbomachinery and for the steady state, known as the radial equilibrium equation is obtained.

$$\frac{1}{\rho} \frac{\partial p}{\partial r} = \frac{V_\theta^2}{r} \tag{3.12}$$

Using the radial equilibrium equation(3.12) that can reflect the nonuniform variations of the static pressure in the annulus, the radial distributions of the back pressure are determined. If radial distributions of the static pressure are available from the experiment like NASA Rotor 67 [79], then the measured radial profile is directly given instead of solving the equation. The density(ρ_b) is calculated by using the following isentropic relation.

$$\rho_b = \left(\frac{p_b}{p_i} \right)^{\frac{1}{\gamma}} \rho_i \tag{3.13}$$

where p_i is the static pressure and ρ_i is the density at the first interior cell of the outlet boundary. Using the velocity, pressure and density at outlet boundary determined, the total energy given by Eq. (2.27) is updated.

3.4 Rotor Wall BC

On the solid wall, the non-slip boundary condition is applied to enforce mass flux going through the wall to be zero. The velocity components of the ghost cells are obtained by the extrapolation between the moving wall velocity and interior cells as follows:

$$\vec{V_b} = 2\vec{V_w} - \vec{V_i} \tag{3.14}$$

where $\vec{V_b}$ denotes the ghost cell velocity, $\vec{V_i}$ stands for the velocity of $1st$ interior cell close to the wall, and $\vec{V_w}$ is wall moving velocity given by $\vec{\Omega} \times \vec{r}$. Another option to save mesh size in our computation is to use the law of the wall. When y^+ is between 11 and 300, the no slip condition is replaced by using the wall function.

$$u^+ = \frac{1}{k} lny^+ + B \tag{3.15}$$

where k denotes Von K*á*rm*á*n constant taken as 0.41, and B denotes a dimensionless constant corresponding to the wall roughness taken as 5.0. The law of the wall approach is based on the assumption that the boundary layer is attached.

The rational that the law of the wall BC is used for all the conditions including near stall is that the vortices in the tip and hub region are mostly large structures and the inconsistency is minimized by using the local velocity direction at the boundary layer edge. The numerical results at the near stall conditions of NASA Rotor 67 by the present authors [22] indicate that the radial profiles at hub and tip agree very well with the measurement at the near stall conditions. It means that such treatment is acceptable and predicts reasonable results. The same BC is also widely used by other research groups to reduce the excessive mesh and CPU time in the rotor tip region [16, 23, 80–86].

Eq. (3.12) is used to determine the casing/hub wall static pressure, whereas zero pressure gradient condition is used on the blade surface. For the density, the perfect gas law is used to impose zero heat flux through the wall.

$$T_b = T_i : \qquad \rho_b = \frac{P_b}{P_i}\rho_i \tag{3.16}$$

3.5 Circumferential Phase-lagged Boundary Conditions

For turbomachinery, each blade is subjected to unsteadiness due to the phase difference. Therefore, a boundary condition needs to be implemented on the circumferential boundaries of a sector of the annulus in order to avoid use of a full annulus configuration. The time shifted phase lag or Direct Store method is implemented by assuming that the phase-shifted periodicity exits at upper and lower circumferential boundaries.

3.5.1 Direct Store Phase Lag Method

The Direct Store phase lag BC is utilized as suggested by Erdos et al. [1] and Srivastava et al. [31] based on phase periodicity with the period determined by nodal diameter. The Direct Store BC is selected for this study since it does not need to input the primary perturbation or vibration frequencies required by the Fourier phase lag BC [34]. Such frequencies are not known *a priori*. In other words, the Direct Store BC presents less loss in fidelity than the Fourier phase lag BC, but still limited to the circumferential periodicity assumption, which does not necessarily exists at all operating conditions.

As sketched in Fig. 3.1, let us assume that the rotor rotates from the upper circumferential boundary to the lower circumferential boundary such that information at the upper side is delayed by time δt. T is the period of one nodal diameter (N_D). To update the upper/lower circumferential boundaries, first the conservative variables of the upper inner cells(Q_{IU}) and the lower inner cells(Q_{IL}) are stored for δt and $T - \delta t$ respectively. Then, these stored values are rotated by the circumferential angle of the sector geometry (ϕ) to update the boundary ghost cells of the other side. The upper ghost cell Q_{GU} at time t can be updated using Q_{IL} at time $T - \delta t$. However, the lower ghost cell Q_{GL} at time t can not be updated using the upper ghost cell values since Q_{IU} at time $t + \delta t$ is not available. The way to update Q_{GL} is to take one cycle-lagged value, Q_{IU} at time $T - t + \delta t$, by assuming phase periodicity as depicted in Fig. 3.1. Note that the boundaries are treated as in-phase condition for the first cycle since the stored Q at both sides are not available.

$$Q_{GL}(t) = Q_{IU}(t + \delta t) = Q_{IU}(t - T + \delta t) \tag{3.17}$$

$$Q_{GU}(t) = Q_{IL}(t - \delta t) \tag{3.18}$$

The following definitions for T and δt apply for a given circumferential angle of sector geometry ϕ and a non-dimensional angular velocity R_o

$$T = \frac{2\pi}{R_o \times N_D} \tag{3.19}$$

$$\delta t = \frac{\phi}{R_o} \tag{3.20}$$

3.6 Steady Mixing Plane

A mixing plane technique is implemented using the halo cell approach. The conservative variables are averaged and stored to corresponding halo cell layers of the adjacent domain using the following relations between the moving (or rotating relative frame) and the fixed frame.

$$\begin{pmatrix} \bar{\rho} \\ \bar{\rho}\bar{U} \\ \bar{\rho}\bar{V}_r \\ \bar{\rho}(\bar{V}_\theta + rR_o) \\ \bar{\rho}\bar{e} + \bar{\rho}\bar{C}_\theta rR_o \\ \bar{\rho}\bar{\tilde{\nu}} \end{pmatrix}_{Fixed} \rightleftharpoons \begin{pmatrix} \bar{\rho} \\ \bar{\rho}\bar{U} \\ \bar{\rho}\bar{V}_r \\ \bar{\rho}\bar{V}_\theta \\ \bar{\rho}\bar{e} \\ \bar{\rho}\bar{\tilde{\nu}} \end{pmatrix}_{rotating\ relative\ frame} \tag{3.21}$$

where the overbar denotes volume-averaged variables and the cell volume V can be calculated using cell surface area vectors and cell diagonal.

$$\bar{\Phi} = \frac{1}{V}\int\int\int \Phi dV \tag{3.22}$$

As mentioned previously, the circumferential average cuts off the wake propagation and adds artificial mixing loss to the calculation. However, the mixing plane method is convenient to couple multi-stage computations.

3.7 Fully Conservative Rotor/Stator Sliding BC

The interaction between rotating and stationary blades introduces inherent unsteadiness to the flow of multistage turbomachinery. For instance, the shock wave interaction between the inter blade rows as well as rotating instabilities as a main driver of NSV can be predicted not by the steady approach, but only by the conservative unsteady approach. Numerous studies on the unsteady rotor/stator interaction has been developed [2, 40–42] based on interpolation on the rotor-stator interface.

Rai [40] used the patched and overlaid grid system based on interpolation to solve an axial turbine with a rotor-stator configuration. Chen et al. [43] pointed out that lack of flux conservation can significantly affect the solution accuracy where shock interaction exists between the blade rows. In fact, the methods of rotor/stator interaction using any type of interpolation methods can not satisfy the conservation of the flux across the interface.

To rigorously resolve wake propagation, shocks interaction and rotating instabilities, a fully conservative sliding BC without interpolation is developed to solve the moving rotor in the rotating relative frame and the stator blades in the fixed frame. The following relations between the rotating relative frame and the fixed frame are used for variable exchange.

$$\begin{pmatrix} \rho \\ \rho U \\ \rho V_r \\ \rho(V_\theta + rR_o) \\ \rho e + \rho C_\theta r R_o \\ \rho\tilde{\nu} \end{pmatrix}_{Fixed} \rightleftharpoons \begin{pmatrix} \rho \\ \rho U \\ \rho V_r \\ \rho V_\theta \\ \rho e \\ \rho\tilde{\nu} \end{pmatrix}_{rotating\ relative\ frame} \tag{3.23}$$

The conservative variables in cylindrical rotating coordinates ($\rho, \rho U, \rho V_r, \rho V_\theta$, ρe, $\rho\tilde{\nu}$) are exchanged when the moving domains slide and are updated in every pseudo time step. Since the sliding BC with the hallo cells ensure the sliding boundary to be solved in the same manner as the inner domain, it hence can capture the interactive effects between the rotor and the stator.

The condition for this sliding BC to avoid interpolation across the sliding BC is to use one-to-one matched grid points at the interface [87]. The two domains at the interface need to have the same mesh size and the grid point coordinates, which should be also evenly distributed circumferentially. This condition can be always satisfied if it is a full annulus calculation. If it is for a sector of the annulus, a geometrically periodic sector should be used first if possible. In this case, the grid size of the interface disk in the rotor circumferential direction can be found by the greatest common factor (GCF). For example, if a compressor has 56 IGV blades and 35 rotor blades, the full annulus can be reduced to 1/7th annulus with 8 IGV blades and 5 rotor blades, satisfying the geometry periodicity. Then, the GCF is 40 as 5 multiples per IGV blade and 8 multiples per rotor blade can meet the matching condition for both domains. In case a geometric periodicity for a sector of the full annulus does not exist, a sector being closest to a geometric periodicity may be used based on the best judgement.

It is desirable to use a physical time step (Δt_{cell}) that moves the rotor a distance exactly equal to the circumferential grid interval. This will ensure the mesh always slides in a perfectly matched system as depicted in Fig.3.2. Δt_{cell} can be calculated as

$$\Delta t_{cell} = \frac{60}{RPM \times N_M} \frac{V_\infty}{L} = \frac{2\pi}{R_o \times N_M} \tag{3.24}$$

where R_o is Rossby number and N_M denotes total number of grid cells in the rotor rotational direction.

As illustrated in Fig. 3.3, assuming the rotor domain is rotated by two cells from the initial position, then cell 3 to 11 on the rotor side and cell 1 to 9 on the stator side are matched and exchanged. However, cell 1 and 2 of the rotor domain and cell 10 and 11 of the stator domain will have no halo cells for data exchange. Therefore, we define the exchange array of those cells using a periodic rotation rule under the condition that the circumferential boundaries are a nodal diameter boundary. For instance, rotor cell 1 and 2 are rotated by an angle (ϕ) and are exchanged with the stator cell 10 and 11. We employ the conservative cell exchange technique to reduce the computational efforts and to fully conserve the fluxes across the sliding interface. When Δt is large and the rotor mesh sliding distance is hence also large, more pseudo time steps are usually needed to reduce the residual. Conservation of mass flux through the sliding interface is inspected for a GE axial compressor study in [87].

3.7.1 Full-Annulus Algorithm

The condition for this sliding BC to avoid interpolation across the sliding BC is to use a one-to-one matched grid at the interface [87]. Two domains at the interface have to have the same mesh size and also the grid points should be evenly distributed circumferentially. This condition can be always satisfied for full annulus calculations. When the rotating blades are moving, the mesh of the rotor blades moves with the blades. The one-to-one connection of the two grid points from the stationary blade to the moving blade at the sliding interface will remain on the same grid points when the circumferential distance of the two grid points is small. When the circumferential distance of the two grid points is greater than half of the grid interval due to the moving blades, the connection will switch to the next grid point so that all the grid points remain one-to-one connected without high mesh skewness. This process keeps being repeated in the rotor-stator sliding interface during the calculation.

For a full-annulus computation, the rotor and stator interface domains may be prohibitively large in terms of mesh size compared to blocks in other regions of the mesh (i.e. blocks around the rotor blade). This requires for interface domains to be split into smaller regions circumferentially to speed up parallel computing across the interface. Fig. 3.4 illustrates the algorithm of the conservative sliding BC for multiple processes at the interfaces. If the interface is defined by a single block on each side of the interface, then the send and receive commands for the MPI parallel computing procedures will have only one destination ("d1") and the BC would follow the same procedure found in [87]. Once the interface is divided further into more blocks the logics behind the destinations of the send and receive commands for MPI become increasingly more complex. The sketches on the left in Fig. 3.4 illustrate the case of having the interface divided into three congruent blocks. At time $t = 0$ all blocks are one to one where $1, 2, ...$ connect directly with $1', 2', ...$ respectively. After some time $t = \tau$ the configuration to the left of the dashed line is present. The arrows show the direction of the MPI command send across the interface for the block with the corresponding color. The labels 'd1' and 'd2' represent destination 1 (the block connected one-to-one at t=0) and destination 2 (the block that follows due to rotation direction) respectively; these labels are assigned for each block based on its neighboring blocks. The blocks defined as d1 and d2 will depend on whether the current block is on the rotor side of the interface or the stator/IGV side and whether it is downstream or upstream of the interface. Assuming that $\Delta\tau = 1/(3\Omega)$, then at $t = \Delta\tau$ the blocks are again one-to-one but with block indices shifted once following the rotation direction; and at $t = \tau + \Delta\tau$ the top configuration to the right of the dashed line applies. At this moment the blocks d1 and d2 have switched since neighboring blocks have different indices. To account for this change in destination blocks for MPI send and receive, arrays with the indices of the blocks upstream and downstream of the interfaces are built such that every $\Delta\tau$ time interval the array with the downstream (red) blocks changes according to rotation convention.

The algorithm for each individual cell is shown at the right of Fig.3.4. Let the rotor domain be rotated by two cells from the initial position. Then, the cell 3 to 11 on the rotor side and the cell 1 to 9 on the stator side are matched and exchanged, while the cell 1 and 2 of the rotor domain and the cell 10 and 11 of the stator domain have no cells to exchange. Therefore, we define the exchange array of those cells to the corresponding neighboring block (i.e. 'd2'). For instance, the rotor cell 1 and 2 are rotated by the angle(ϕ) and are exchanged with the stator cell 10 and 11 of block 'd2'. We employ the conservative cell exchange technique to reduce the computational efforts and to fully conserve data exchange. The rotated mesh is located to the closest cell of the counterpart domain. When Δt is large such that the rotor mesh sliding distance is greater than one circumferential grid cell spacing, more pseudo time steps are usually needed to reduce the residual due to the large rotor moving distance.

3.7.2 Single-Passage Phase-lag Treatment

As mentioned above, a one-to-one, evenly distributed, matched grid at the interface is used for the multi-stage single-passage simulations. In Fig. 3.5 a sketch of the ghost, or buffer, cells is presented for a single-passage configuration on the left in sketch (a). On the right of Fig. 3.5 in sketch (b) the flow of information is represented with an arrow within the passage towards the opposite passage buffer layer showing the algorithm conceptualization of populating the buffer cell array with the flow information inside the opposing passage, with the proper transformations of the flow variables relating to rotating or fixed reference frame as explained in Eq.3.23.

When the passage circumferential angle is not the same across the interface due to blade count mismatch, which is common in axial compressors, the problem of non-overlap regions emerges. The sketch in Fig. 3.6 provides a visual to contextualize the method used in implementing Direct Store phase lag to the sliding interface to overcome non-overlap data exchange. Point A is a circumferential location in the rotor passage (upstream blade-row) at the sliding interface; similarly, Point B corresponds to a circumferential location at the sliding interface on the stator passage (downstream blade-row). Both circumferential points remain at the same relative location within the blade passage as rotation occurs. After a time δt, the rotor passage would have traversed a number of stator passages, considered in an artificial way inside the simulation, to a position where the Points A and B coincide in their relative circumferential locations.

The flux information is exchanged as explained in Section 3.7 across the rotor-stator interface; data in Point B is sent to the ghost cell location corresponding to Point A. At this instant in the data exchange procedure Phase-lag is implemented by retrieving data at the current time step, enforcing a periodic passages (i.e. $N_D = 0$), or at an earlier–or lagged–time step depending on the assumed circumferential wavelength (i.e. $N_D \neq 0$).

The approach of implementing the time lag between the flowfield at the physical stator passage and the virtual stator passage, which is stored in the buffer layer of the rotor, is the same as the one used for the circumferential phase-lag explained in Section 3.5 and shown in Fig. 3.1.

IGV blade wakes convected through rotor passage and onto the stator passage are depicted in Fig. 3.7 with entropy contours for the full-annulus (left) and single-passage (right) conservative sliding interface as validation that BC development is capable of capturing unsteady rotor-stator interaction phenomena.

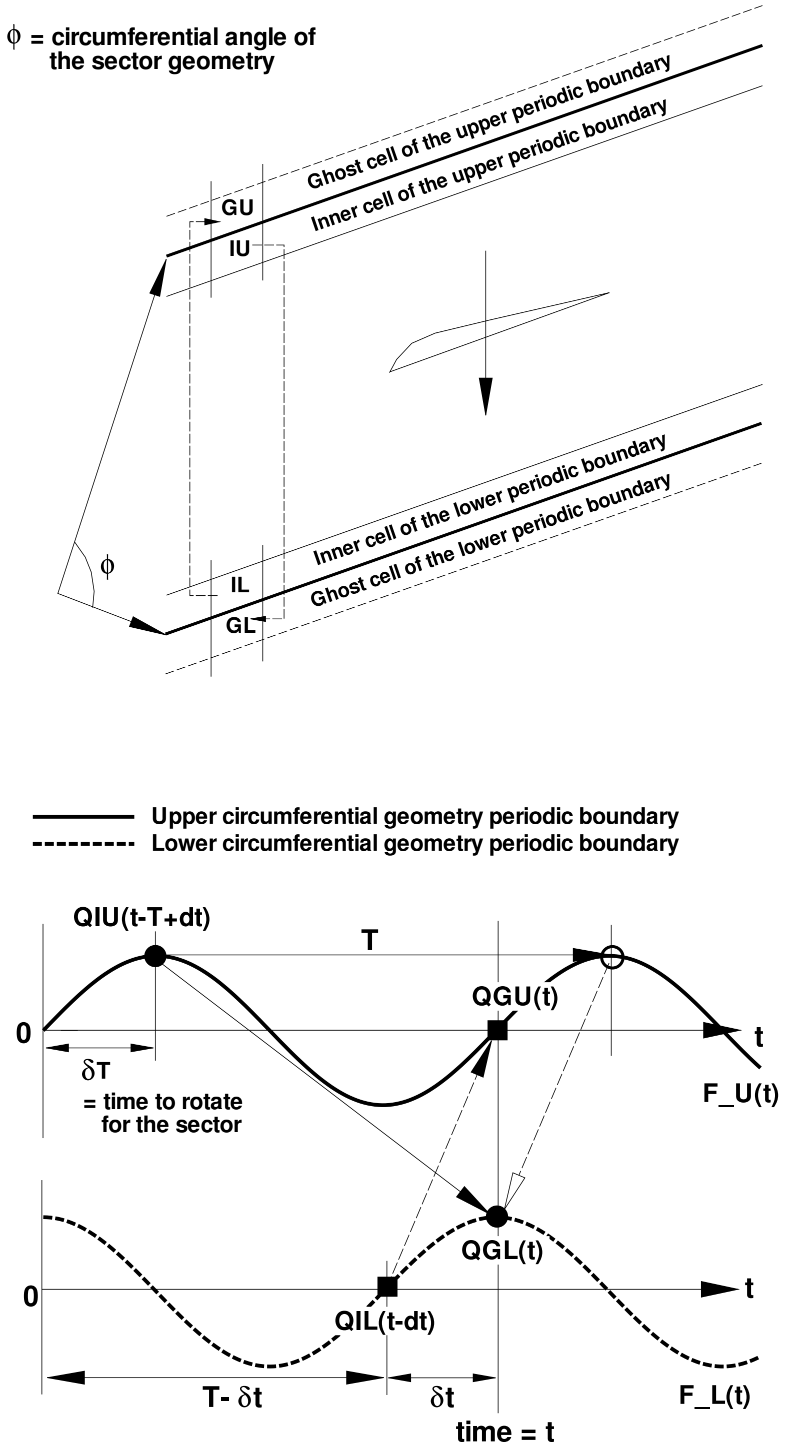

Figure 3.1: Sketch of the time shift phase lag BC showing how to define upper periodic ghost cell, Q_{GU}

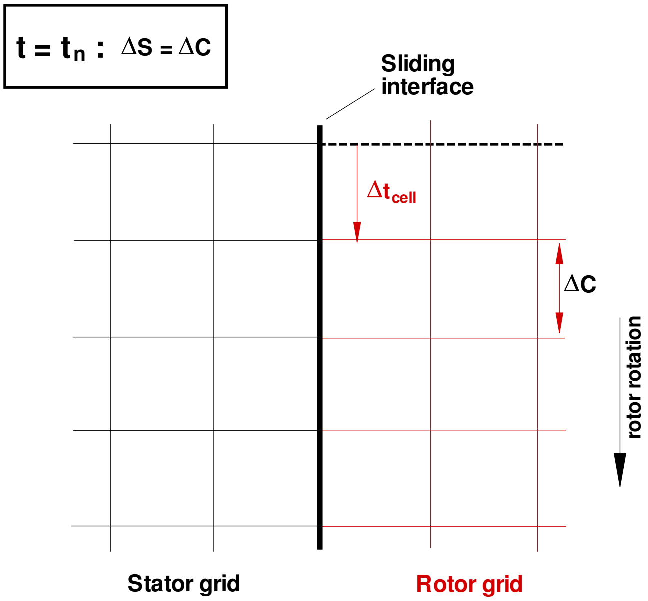

Figure 3.2: Perfectly matched one-to-one mesh sliding system due to use of Δt_{cell} as unsteady physical time step

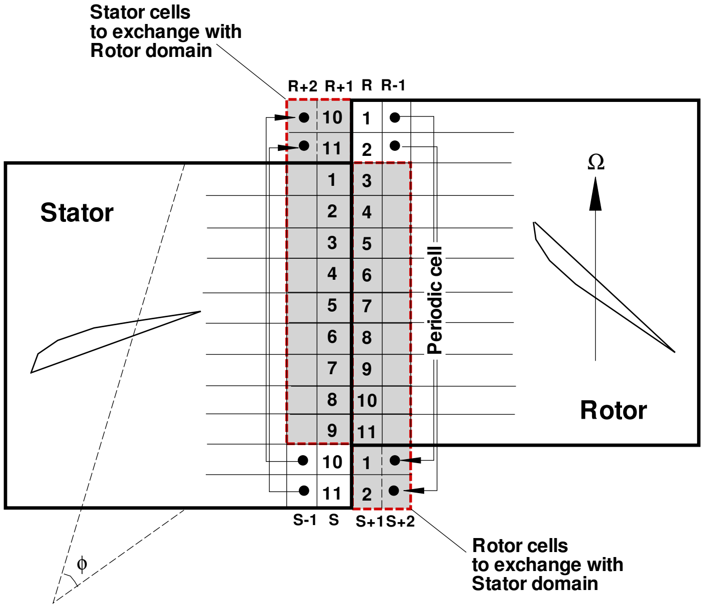

Figure 3.3: Rotor/stator interface exchange algorithm

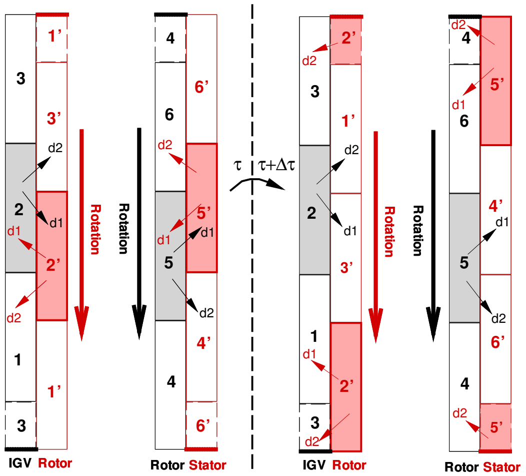

Figure 3.4: Rotor/Stator interface exchange algorithm between blocks

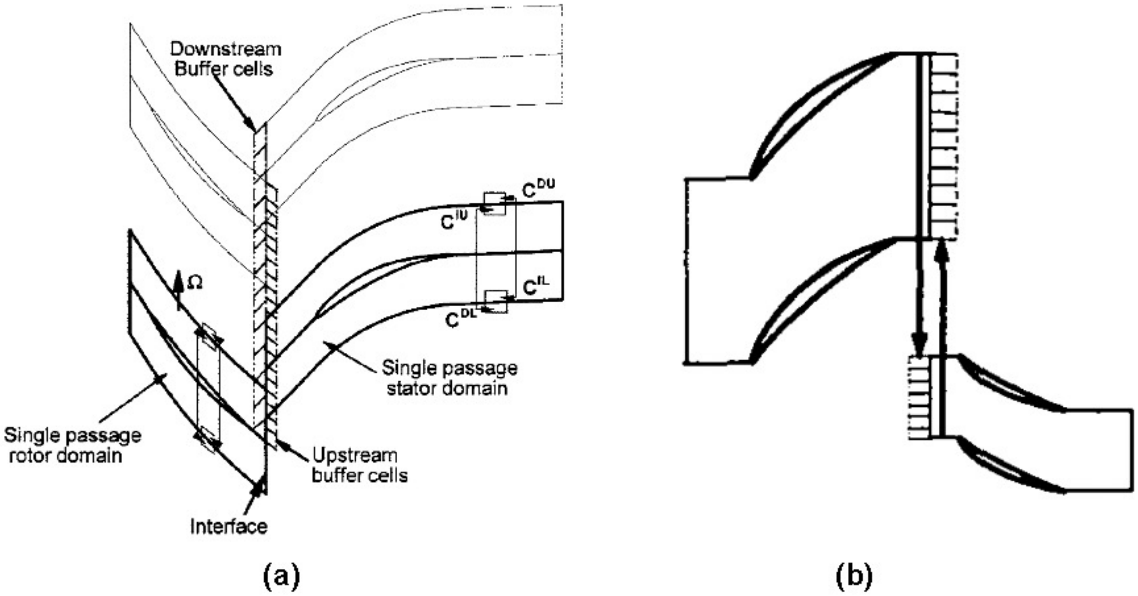

Figure 3.5: Ghost (or Buffer) layer conceptualization (a) and information propagation at sliding interface (b) for multi-stage single-passage configuration (plots adopted from [3] and [4] respectively).

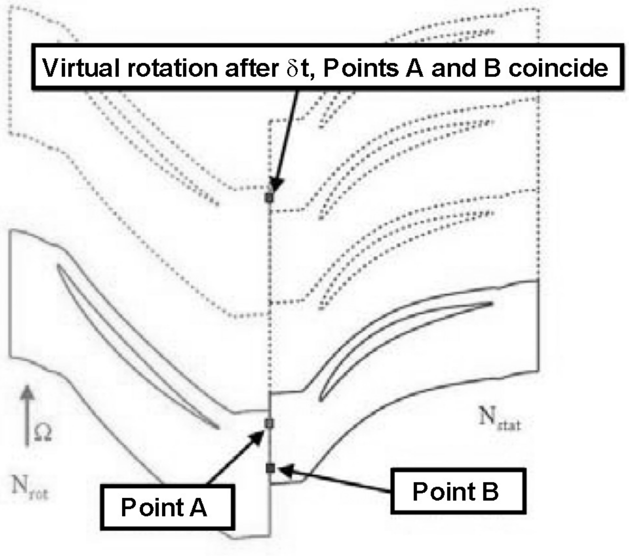

Figure 3.6: Sketch of rotor travelling through virtual stator passages and relative rotor (Point A) and stator (Point B) passage locations of Point of coincidence in virtual passages.

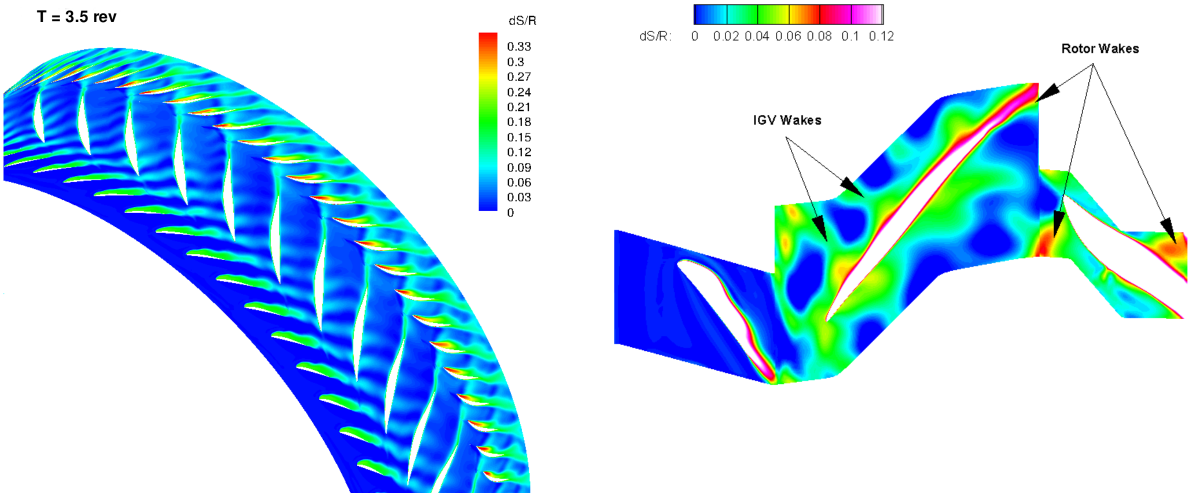

Figure 3.7: 1-1/2 Stage wake patterns shown by entropy increase contours at 50% span for full-annulus (left) and single-passage (right) configurations.

CHAPTER 4

Full-Annulus Simulation of NSV

The purpose of this study is to conduct a high-fidelity simulation of NSV aerodynamic excitation in the first 1-1/2 stages of a GE high-speed axial compressor using a full-annulus configuration, which is able to capture flow structures with length scales on the order of the rotor circumference and to prevent errors induced due to circumferential BCs. Also, the current study will aid in the validation of the time-shifted phase-lag BC adopted by Im et al. [13] by comparing the results of the 1/7th annulus simulations to the full-annulus results.

4.1 The High-Speed Axial Compressor

The high-speed axial compressor studied exhibits NSV at the first stage rotor blades [10]. The first 1-1/2 stage with 56 IGVs, 35 rotor blades and 70 stator blades of the full annulus compressor is used for current simulations. The rotor tip clearance of the compressor rig is 1.1% of tip chord. The measured blade NSV is a phase-locked response and close to 1st torsional blade natural frequency. The strain gage on the blade surface shows the NSV frequency of 2600 Hz at around 12880 rpm and 2661 Hz as the rotor speed slightly decreases to 12700 rpm as shown in Fig. 1.1 (left). The measured NSV frequency of the blade surface can be used for comparison since the rotating frame of reference is adopted in this study. Also on the right of Fig. 1.1 is shown the casing unsteady pressure measurement frequencies in absolute frame, which are doppler shifted.

4.2 Numerical Methods

The unsteady Reynolds-averaged Navier-Stokes (URANS) equations are solved in a rotating frame [22] with the Spalart-Allmaras (S-A) turbulence model [69]. A shock capturing scheme is necessary to simulate high-speed axial compressors since most rotor blades experience shock/boundary layer interaction. In this study the Low Diffusion E-CUSP (LDE) Scheme [64] as an accurate shock capturing Riemann solver is used with a 3rd order WENO reconstruction for inviscid flux and a 2nd order central differencing is used for viscous terms [57]. An implicit 2nd order dual time stepping method [78] is solved using an unfactored Gauss-Seidel line iteration to achieve high convergence rate. The high-scalability parallel computing is implemented to save wall clock time [88].

The interaction between rotating and stationary blades introduces inherent unsteadiness to the flow of multistage turbomachinery. For instance, the shock wave interaction between the inter blade rows as well as rotating instabilities as a main driver of NSV can be predicted not by the steady approach, but only by the conservative unsteady approach. Numerous studies on the unsteady rotor/stator interaction has been developed [2, 40–42] based on interpolation on the rotor-stator interface. Rai [40] used the patched and overlaid grid system based on interpolation to solve an axial turbine with a rotor-stator configuration. Chen et al. [43] pointed out that lack of flux conservation can significantly affect the solution accuracy where shock interaction exists between the blade rows. In fact, the methods of rotor/stator interaction using any type of interpolation methods can not satisfy the conservation of the flux across the interface.

In this study a fully conservative sliding boundary condition (BC) for multiple processors at the blade row interface is developed in order to rigorously resolve wake propagation, shock interactions and rotating instabilities while maintaining an even computational load for the full-annulus simulation. All boundary conditions are explained in detail in Chapter 3.

4.3 Computational Mesh

The full-annulus structured mesh for 1-1/2 stage of the compressor is presented in Fig. 4.1. The rotor tip clearance is modeled with 2 blocks of 21 spanwise grid points using an O-mesh topology of density 101×15. The mesh of IGV/rotor/stator is partitioned to total 1246 blocks for parallel computation. The grid around the blade was constructed as an O-mesh. The mesh size for the IGV and stator is 121(around blade)×51(blade-to-blade)×71(blade span); for the rotor the mesh size is 201(around blade)×51(blade-to-blade)×71(blade span). An H-mesh layer is used for the matched one-to-one grid point connection at the sliding BC interface of IGV/rotor/stator that enables variable exchange in a fully conservative manner. Each H-mesh layer has 7 blocks with a mesh size of 201(tangential)×6(axial)×71(blade span). The total mesh size for this full-annulus simulation of 1-1/2 compressor stages is 97,317,920.

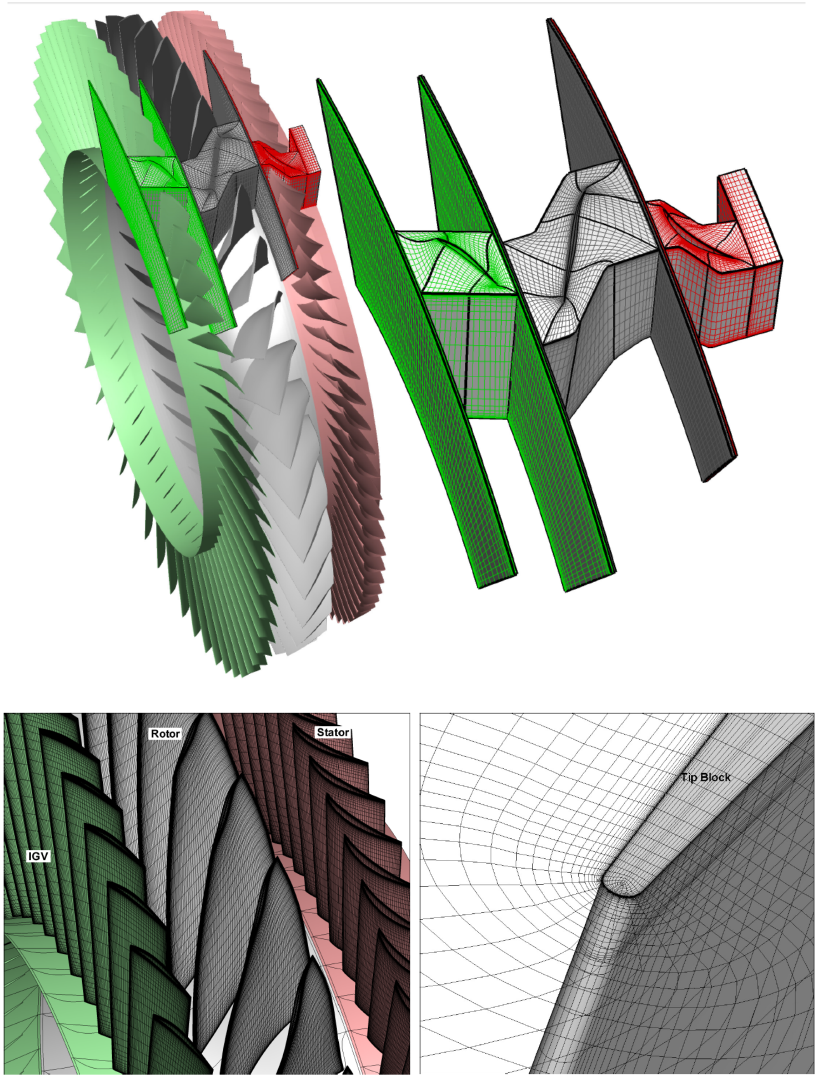

Figure 4.1: Full Annulus mesh for NSV simulation and close-up views of blade surface mesh, interface H-mesh blocks and rotor tip gap O-mesh.

4.3.1 Numerical Probes

The numerical probes to acquire the static pressure responses at the tip clearance are shown in Fig. 4.2. A total of 520 points on every blade surface captures instantaneous pressure with a grid of 26 probes spanwise by 20 probes distributed in the axial direction where 10 are on the suction surface and 10 on the pressure surface. Location of probes is given as a percentage of span and chord as shown in Fig. 4.2.

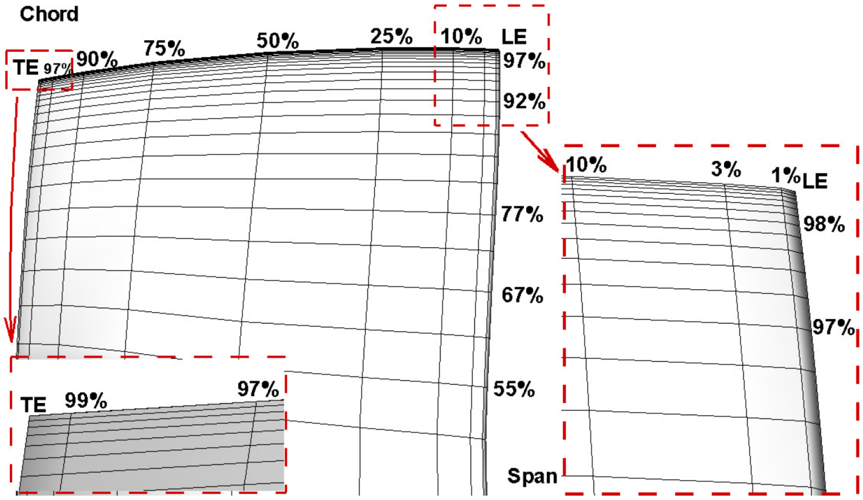

Figure 4.2: Numerical probes of the rotor blade on suction surface, Pressure surface probe distribution is the same.

4.4 Results and Discussion

The rig testing of the axial compressor with 1.1% tip clearance [10] is shown to have the NSV frequency range of 2600 Hz to 2661 Hz, which is located between 12EOL(engine order line) to 13EOL as shown in the Campbell diagram in Fig. 4.3. The measured compressor NSV is at 2600 Hz at the present simulation operating condition of 12880 RPM. The numerical residual is reduced by three orders of magnitude within each physical time step, which is usually achieved within 15 to 20 pseudo time step iterations. A non-dimensional time step of about 0.005 is used. The Campbell diagram can be used to evaluate whether a blade frequency including natural frequency is synchronous or not with engine shaft. The numerically captured NSV frequency is 2439 Hz, which agrees fairly well with the measured value of 2600 Hz as shown in Fig. 4.3.

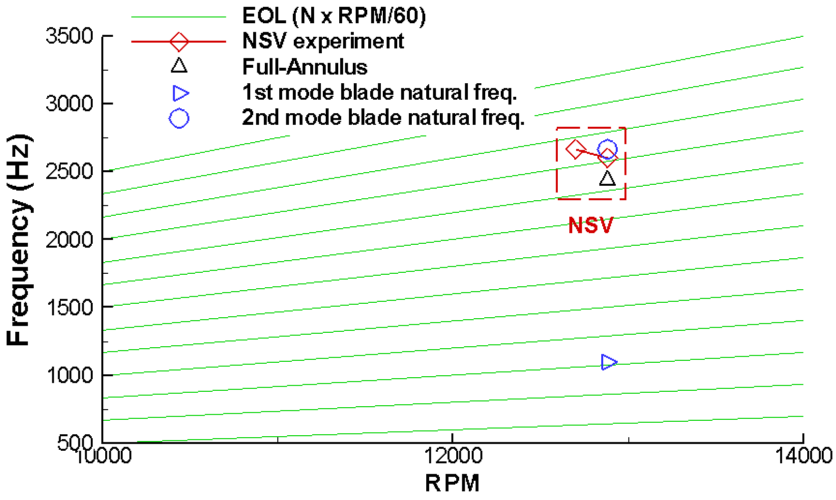

Figure 4.3: Campbell diagram

Steady flow simulations are conducted using a single passage of the compressor at different back pressure conditions to obtain the speedline. Fig. 4.4 shows the predicted speedline of the 1-1/2 stage axial compressor. Note that the full-annulus speedline point in Fig. 4.4 is obtained by averaging the final 2 rotor revolutions to avoid the transitional period since the unsteady computations are started from the steady solutions obtained by a mixing plane approach [87].

4.4.1 Flow Structure and Instabilities

The wake propagation patterns of the 1-1/2 stage compressor is shown for 3.25 and 3.5 rotor revolutions in Fig. 4.5 which demonstrate the instantaneous entropy contours at 50% of the span for the aforementioned times. The IGV wakes are cut by the rotor blade row and the rotor blade wakes are cut by the downstream stators. Fig. 4.5 also indeicates that the sliding BC indeed preserves the wake profiles very well due to the flux conservation.

Previous unsteady simulations of the present compressor [10, 13, 19, 20] show that a circumferentially traveling vortex above 78% of the span causes NSV. This near-blade-tip circumferentially traveling vortices have been shown to occur in all rotor blades of the 1/7 annulus simulations [13, 19, 20], and the present simulation confirms that this vortex system is also present in all the blades of the full-annulus simulation as shown in Fig. 4.6.

The zoomed in circumferentially traveling vortex structure is shown in Fig. 4.7. It can be seen that the reverse flow occurs at the outer span region of the vortices. The axes of the tornado vortices, shown by the vortex core lines, are perpendicular to the suction surface of the blades. When observed for the full-annulus in Fig. 4.8, the vortex core line at T=3.5 revolutions has a clear presence in every rotor-blade passage near and in front of the leading edge of the blades, which indicates that the circumferentially traveling vortex tube is closed along the annulus. Fig. 4.9 is the zoomed in view showing that the vortex core is nearly normal to the blade suction surface and the vortex propagation direction is opposite to the rotation direction in the relative frame.

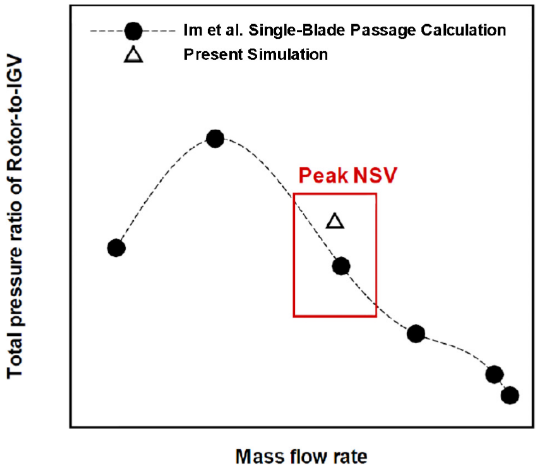

Figure 4.4: Total pressure ratio of IGV-to-Stator versus mass flow rate at the rotor exit.

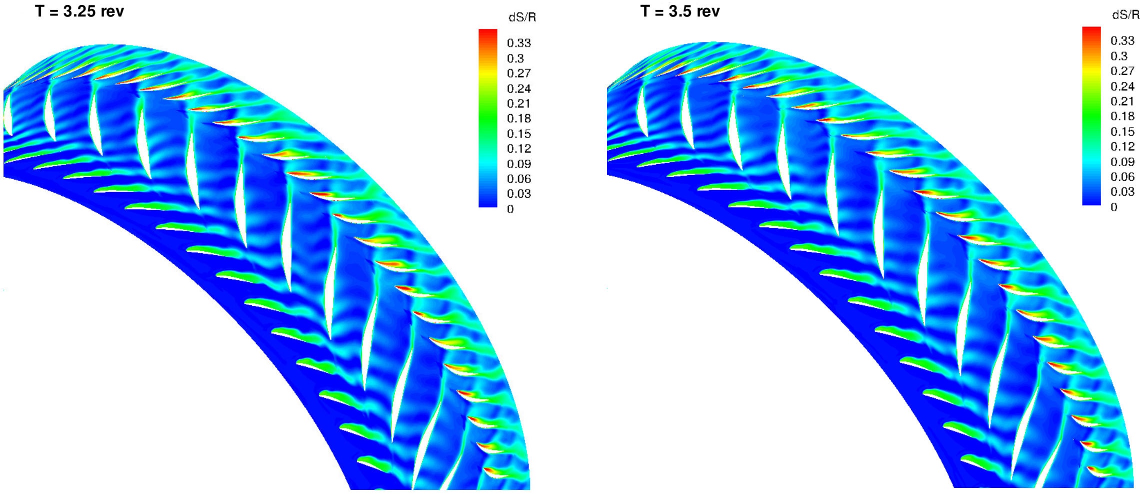

Figure 4.5: 1-1/2 Stage wake patterns shown by entropy increase contours at 50% span at 3.25 and 3.5 revolutions.

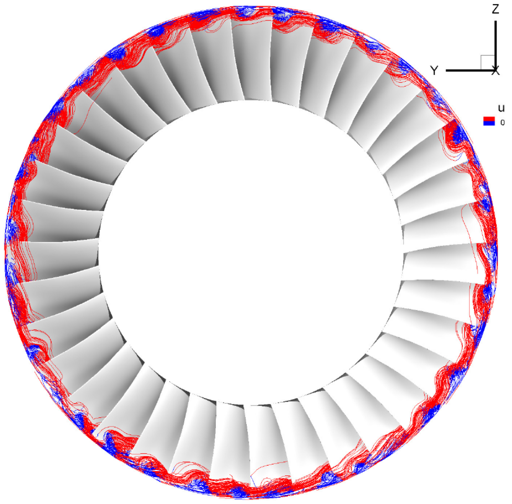

Figure 4.6: Streamlines colored by axial velocity showing the vortex structure predicted in rotor stage above 77% span. Red color shows flow going downstream, blue color shows backflow going upstream toward IGV.

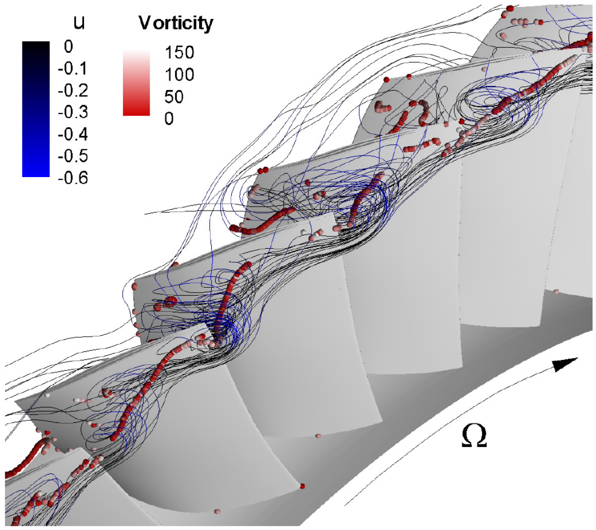

Figure 4.7: Zoom-in view of the circumferentially traveling vortices near the tip region of rotor blades shown by streamlines colored by reverse axial velocity with vortex core shown in red.

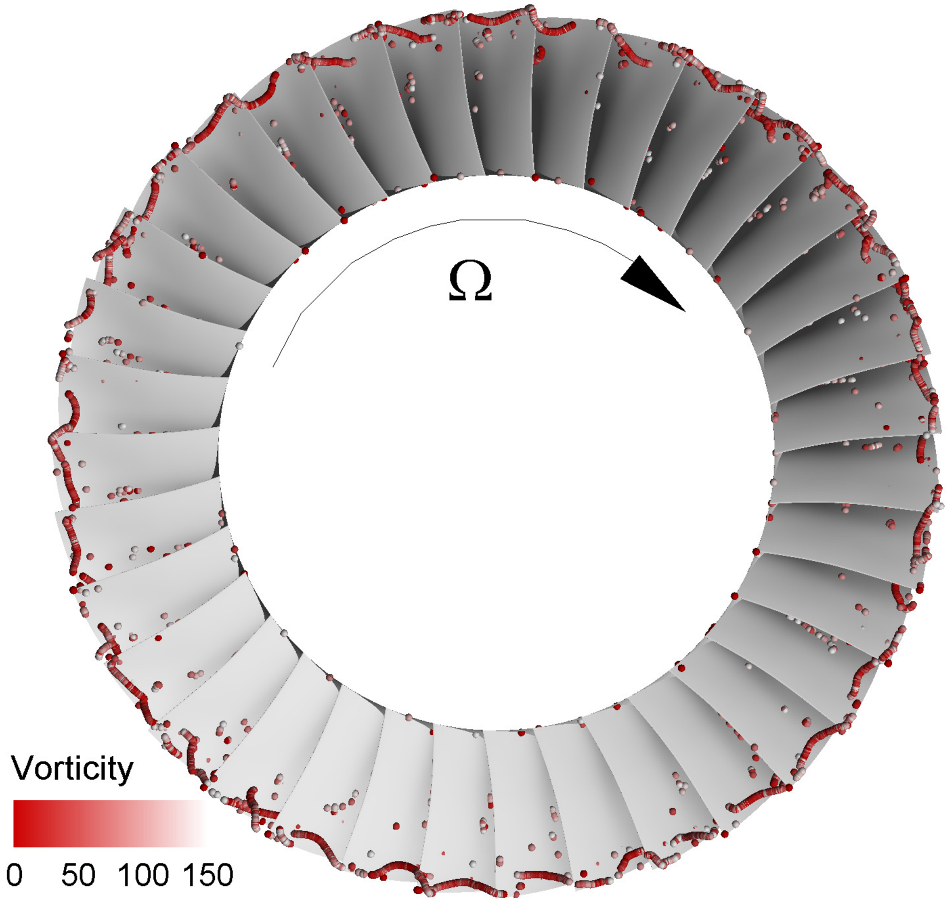

Figure 4.8: Instantaneous vortex core structure predicted at T=3.5 rev. with all blades showing presence of vortical flow showing a circumferential vortex tube.

The full-annulus URANS simulates how the circumferentially traveling vortex causes the NSV, which is displayed in Fig. 4.10 showing the instantaneous motion of the vortex over the two rotor blades. The vortex on the blade A suction surface at $\frac{1}{70}$ Rev moves to the blade B at $\frac{6}{70}$ Rev in the opposite direction to the rotor rotation. The vortex travels on the suction surface from the leading edge to the trailing edge, and then crosses the passage to the next blade leading edge. Such a vortex motion trajectory generates two low pressure regions due to the vortex core positions, one at the leading edge and one at the trailing edge, both are oscillating due to the vortex coming and leaving. These two low pressure regions create a pair of coupling forces that generates a torsion moment causing NSV. This is consistent with the experimental and numerical observations in [10, 19] that the NSV of this rotor is dominant at its first torsion mode(2nd mode). The frequency of this tornado vortex propagation captured is roughly equal to the NSV frequency of the blade pressure signals. Other experiments [6, 12] for axial fan/compressor also show that the flow instabilities in the vicinity of rotor tip rotates circumferentially and cause NSV.

4.4.2 Full-Annulus NSV Excitation Frequencies

The full-annulus simulated NSV excitation frequency is measured and compared to the 1/7 annulus simulation [13] for the same rotor geometry and the same tip clearance of 1.1% of tip-chord. Fig. 4.11 shows the predicted frequencies for the pressure signals on the blade suction surface and the comparison to the frequencies predicted by the 1/7 simulation. This demonstrates that the circumferentially time-shifted phase-lag BC used in [13] can capture the same NSV frequency as the full-annulus. A sample

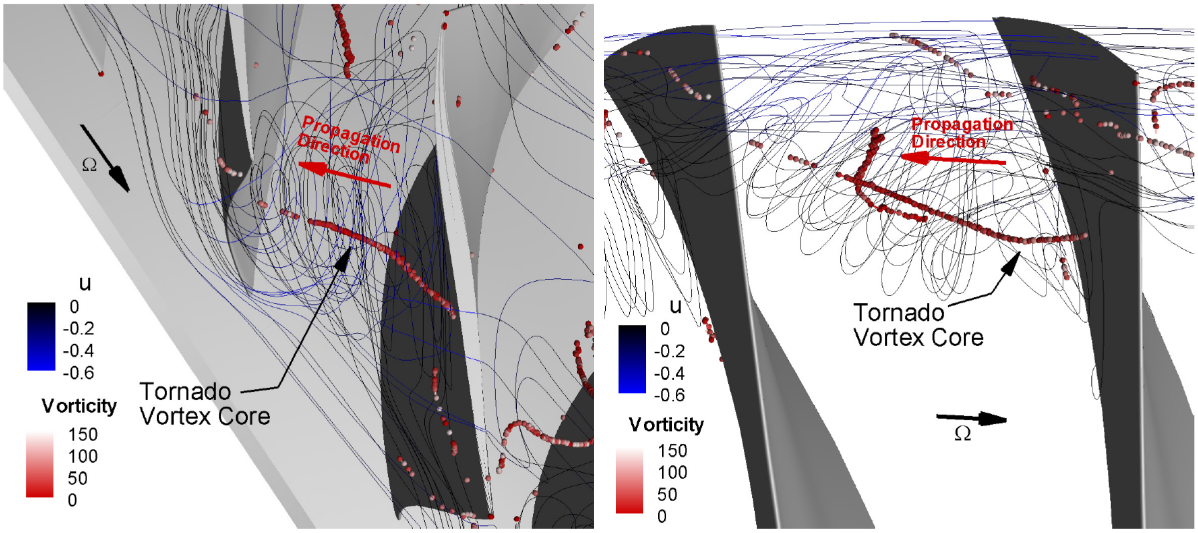

Figure 4.9: Side and top view of a circumferentially traveling vortex with vortex core almost perpendicular to suction surface and propagation direction parallel but opposite to rotation direction.

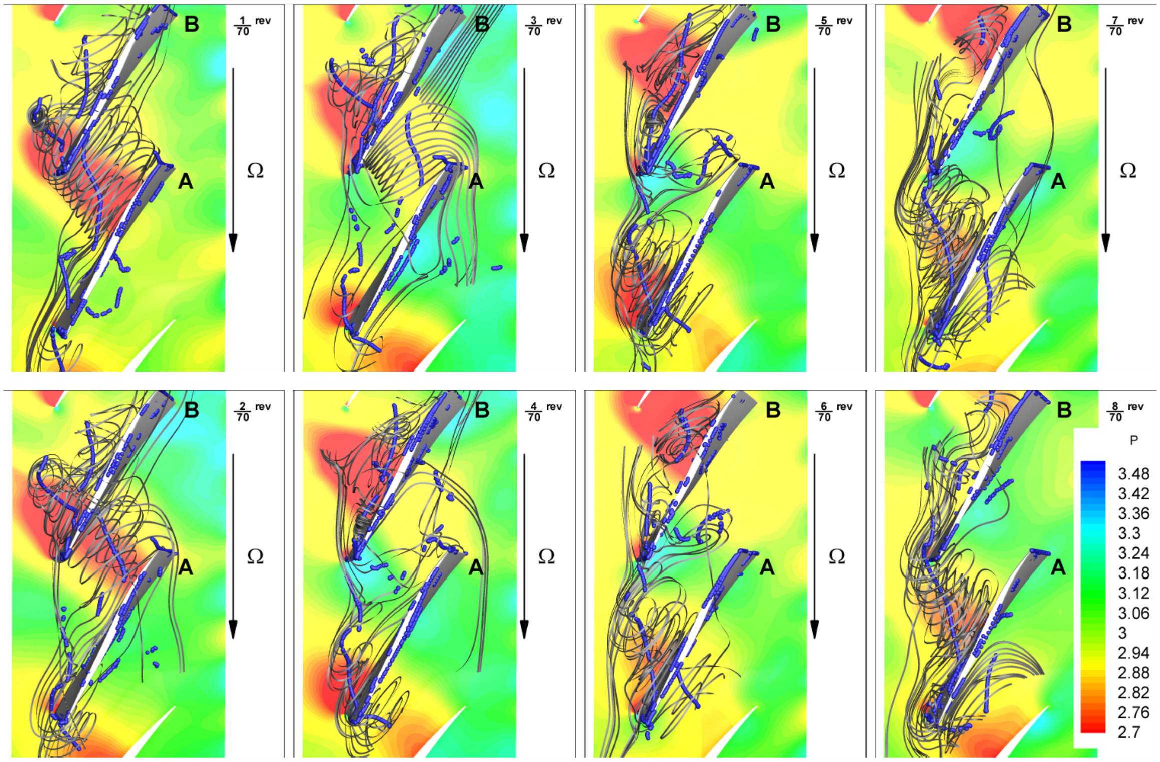

Figure 4.10: Instantaneous vortex trajectories in tip region every 1/35th of a revolution colored by the normalized static pressure.

static pressure reading of one of the 35 rotor blades is presented for the numerical probe at 77% of span at the LE in Fig. 4.12.

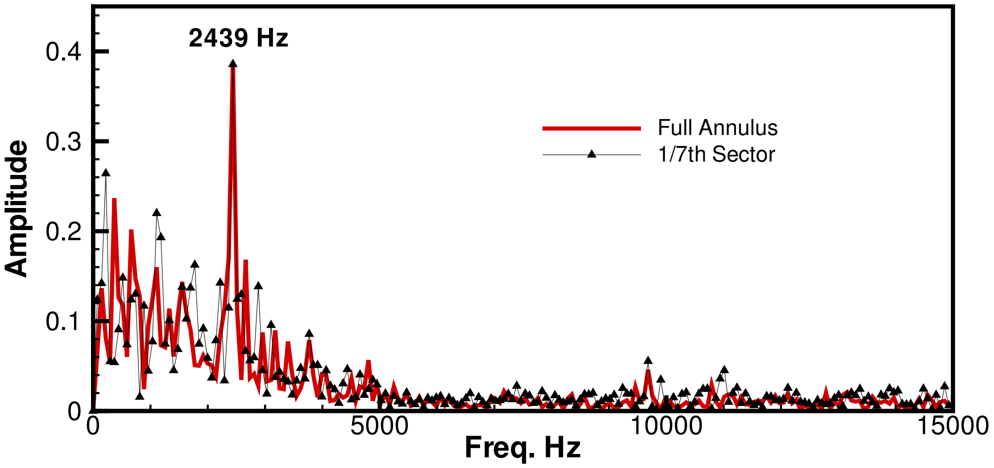

Figure 4.11: Predicted NSV frequencies for full annulus and 1/7th annulus simulations for a sample blade at 77% span near LE.

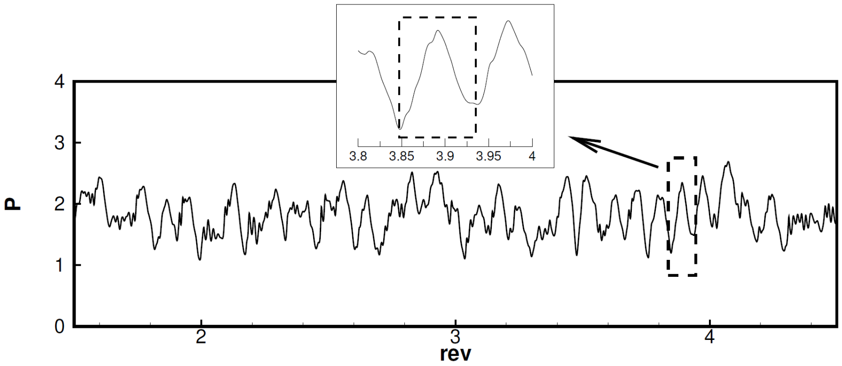

Figure 4.12: Pressure signal for sample blade of full-annulus (blade 6) at 77% span near LE with zoom-in of a signal period.

Fig. 4.13 plots the frequency of all the 35 rotor blades for readings from the same probe of each blade as in Fig. 4.2 . There is an important finding that is not captured by the 1/7 simulation: the NSV frequencies are for the most part the highest peak

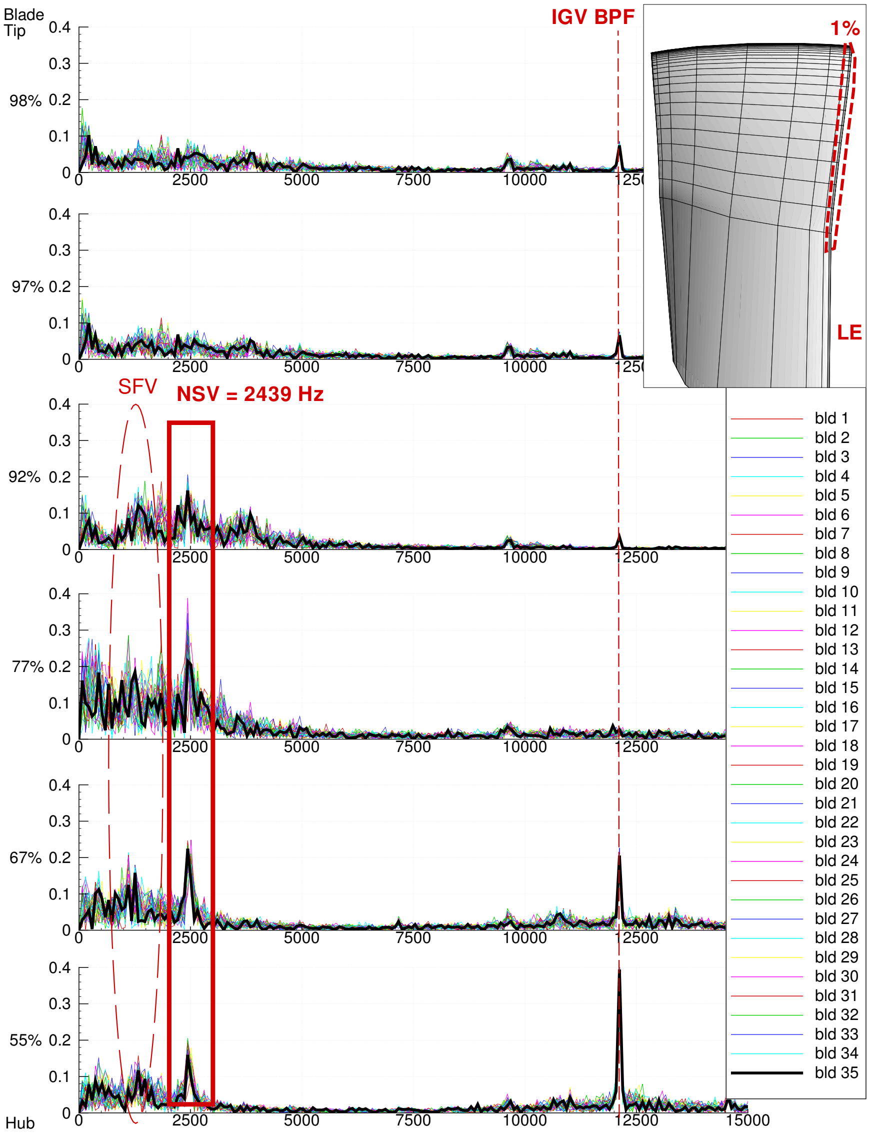

Figure 4.13: Frequency maps for all 35 rotor blades for LE probes showing strong frequency response for NSV frequency of 2439 Hz.

in the frequency map, but some blades show phenomena of lower frequency taking precedence to the NSV phenomenon as seen in Fig. 4.13.

The high response frequencies below 2400 Hz are caused by flow separation at high incidence through out the annulus. Comparing with the rig test results in Fig. 1.1, measurements by the strain gages on the blades do not show this behavior, but the pressure measurements on the casing wall do show that while NSV phenomena has dominance, flow frequencies related to SFV are still significant in amplitude compared to NSV-related frequencies. The difference in these two behaviors can be explained by the nature of the measurement. Strain gage measurements follow blade deformation and therefore the dominant frequencies captured will be modal, whereas the pressure transducer will capture all frequencies found in the flow without being influenced by blade modal frequencies. Since the numerical probes used in this simulation act more as pressure transducers and the blades are assumed to be rigid, the frequencies captured should and do behave like those captured by the pressure transducers in the experiment.

The key issue with these lower frequencies is that they hint at the presence of secondary flow features other than NSV that relate to flow separation. This can be illustrated by plotting on the blade surface the peak excitation frequency and amplitude contours using the FFT analyses at each probe location, as shown in Fig. 4.14. This sample blade is representative of the blades around the annulus. Two basic conclusions can be drawn from Fig. 4.14:

1. Maximum excitation amplitude is found at the LE with upper span locations experiencing NSV excitation frequencies.

2. Downstream of LE on suction surface, above 77% span, the excitation amplitude remains high until approximately 30% of chord length. Downstream of 30% chord length the excitation amplitude decreases significantly.

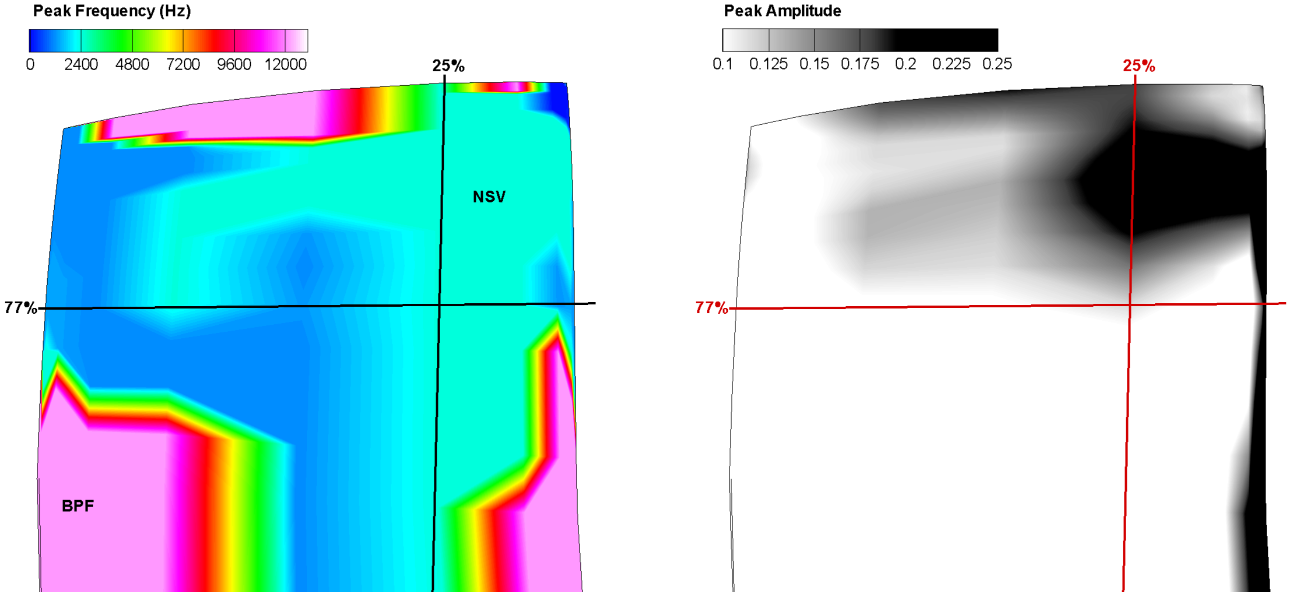

Figure 4.14: Sample blade suction surface with contours of peak frequencies from FFT at each probe location (left) and corresponding peak amplitude (right) showing region of NSV frequency dominance between LE and 30% chord location. 77% span and 25% chord locations are shown for reference (see Fig. 4.2).

4.4.3 Stage Unsteady Response

In Fig. 4.13 the spread of amplitudes of NSV and SFV frequencies is wide, which means that for each blade the flow excitation differs slightly and the flow separation is aperiodic and local to specific passages. For example, the dual-vortex system is not present in every rotor passage, nor is it a sustained flow structure as the circumferentially traveling vortex is. Because of the local nature of such flow structures, instantaneous stage performance parameters were recorded throughout the simulation to consider the effect of the vortex systems on the whole annulus. Fig. 4.15 shows the unsteady average stage total pressure ratio radial profile obtained by integrating over the full-annulus circumferentially for each span location using a mass-averaged approach. The total pressure ratio is calculated as the ratio of the total pressure at the rotor outlet to that at IGV inlet. Also the range of total pressure ratio variation at each radial location (shown by the variation bars in Fig. 4.15) is the highest near the 77% span and above, the same location where flow excitation is observed as the strongest locally on rotor blade suction surface that causes the NSV. Total pressure ratio variation is 8.2% of the average total pressure ratio at 77% span, 7.4% at 92% span, and 2.3% at 42% span for a record starting after 1.5 rotor revolutions. The results of a Fourier analysis of the instantaneous total pressure ratios are shown in Fig. 4.16. The frequency spectrum shows that the NSV frequency of 2439 Hz is outstanding for circumferentially averaged total pressure ratio which confirms that NSV is a full-annulus phenomenon.

Fig. 4.15 provides an indication as to the reason of the NSV, and a direction for the redesign of this compressor stage to eliminate it. The loading of the upper blade spans (70% and above) causes large flow incidence, which generates the circumferentially travelling vortex. The vortices further in turn cause large blockage and total pressure ratio oscillation. On the other hand, the mid blade spans show very little total pressure oscillation and could be loaded further. To mitigate or remove the NSV a design with a smaller loading of the upper blade span and a higher loading of the mid blade spans is recommended.

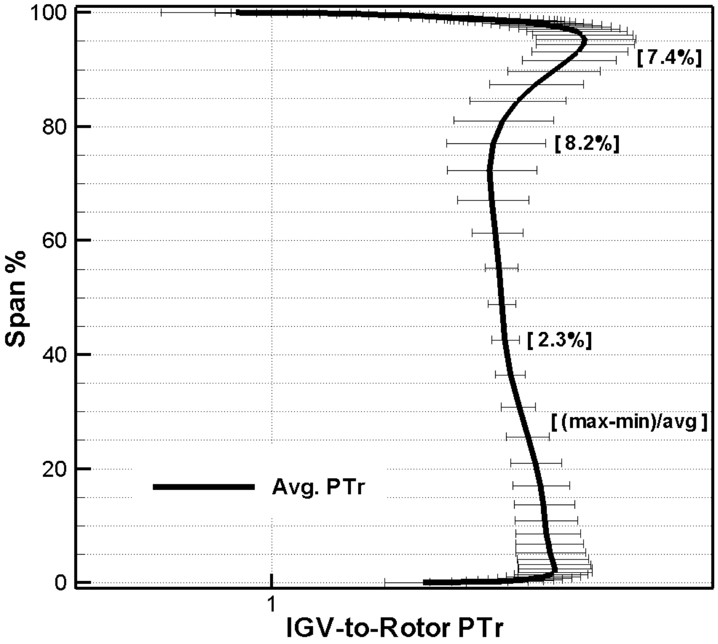

Figure 4.15: Radial profile of total pressure ratio unsteady average measured for IGV inlet to Rotor outlet. Bars indicate range of values in the instantaneous record starting at 1.5 revolutions.

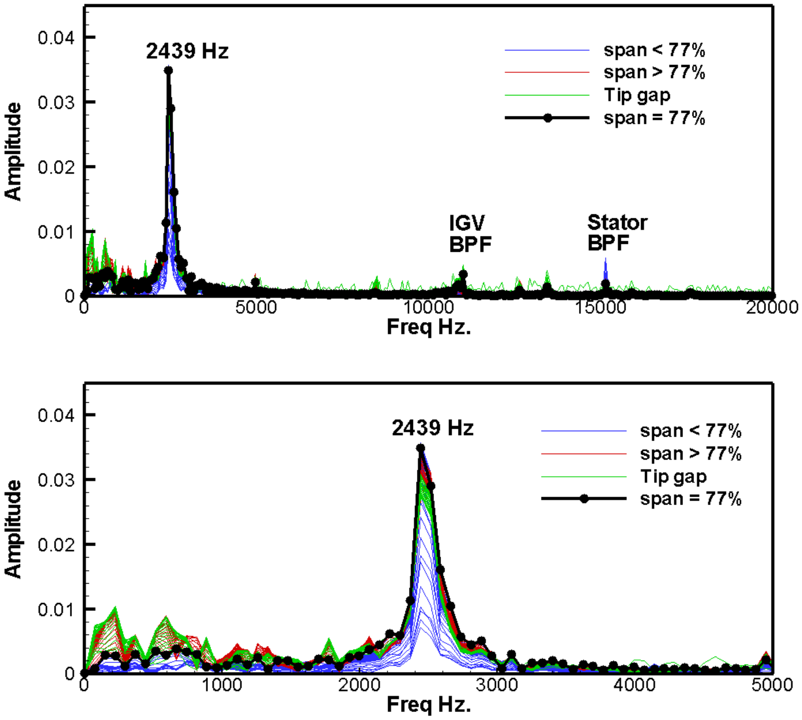

Figure 4.16: Frequency map for circumferentially averaged total pressure ratio instantaneous response showing strong peak at NSV frequency of 2439 Hz for radial locations near or above 77% span.

4.5 Conclusions

A 1-1/2 stage high-speed compressor is simulated using a full-annulus configuration to investigate the NSV aerodynamic excitation without circumferential sector boundary condition effect. A URANS solver is used and captures the NSV flow excitation frequency of 2439 Hz, which agrees reasonably well with the measured NSV frequency of 2600 in the rig test. The phenomena observed confirms for the most part the results obtained using 1/7 annulus URANS simulation with a circumferential time-shifted phase-lag BC. It is observed that the circumferentially traveling vortex formed in the vicinity of the rotor tip propagates at the speed of a non-engine order frequency and causes the NSV. The vortex travels along the suction surface of the blade and crosses the passage outlet near blade trailing edge. Such a vortex motion trajectory repeats in each blade passage and generates two low pressure regions due to the vortex core positions, one at the leading edge and one at the trailing edge, both are oscillating due to the vortex coming and leaving. These two low pressure regions create a pair of coupling forces that generates a torsion moment causing NSV.

The full-annulus simulation shows that the circumferentially traveling vortex has fairly periodical behavior and is a full annulus structure. Also, frequencies below the NSV excitation frequency of 2439 Hz with large amplitudes in response to flow-separation related phenomena are present. This behavior is consistent with experimental measurements.

For circumferentially averaged parameters like total pressure ratio, NSV is observed to have an effect, particularly at radial locations above 70% span. Therefore, to achieve similar or better total pressure ratio a design with a smaller loading of the upper blade span and a higher loading of the mid blade spans should be considered.

The influence of flow instabilities as an important mechanism that sustains NSV in compressor blades must be examined with interaction of structure vibration. Since the present full-annulus simulation assumes rigid blades, future work should include a full-annulus simulation with vibrating blades to determine the influence of blade modal frequencies coupling with flow frequencies and how this fluid-structure interaction affects NSV.

CHAPTER 5

Single-Passage Simulations of NSV

Since results from the full annulus simulation in Chapter 4 show that the circumferentially travelling vortex is present in all passages and propagating opposite to rotation direction in the relative frame, it can be expected that a single-passage simulation of the same configuration should capture the NSV excitation and its respective mechanisms. The GE high-speed axial compressor studied exhibits NSV at the first stage rotor blades [10]. A single-passage of the first 1-1/2 stage with 56 IGVs, 35 rotor blades and 70 stator blades of the high pressure compressor is used for current simulations. The rotor tip clearance of the compressor rig is 1.1% of tip chord. The measured blade NSV is a phase-locked response and close to 1st torsional blade natural frequency. The strain gage on the blade surface shows the NSV frequency of 2600 Hz at around 12880 rpm and 2661 Hz as the rotor speed slightly decreases to 12700 rpm as shown in Fig. 1.1 (left).

The URANS equations are solved in a rotating frame [22] with the Spalart-Allmaras turbulence model [69]. The Low Diffusion E-CUSP (LDE) Scheme [64] Riemann solver is used with a 3rd order WENO reconstruction for inviscid flux and a 2nd order central differencing is used for viscous terms [57]. An implicit 2nd order dual time stepping method [78] is solved using an unfactored Gauss-Seidel line iteration to achieve high convergence rate. The boundary conditions described in Chapter 3 are implemented on the simulations in this chapter.

By implementing a fully conservative sliding rotor-stator interface with direct store phase-lag BC, and a direct store phase-lag BC at the circumferential boundaries, a range of nodal diameters (NDs) are tested to see the influence of assumed disturbance wavelength on NSV excitation frequencies and amplitudes. Also, to test the influence of downstream stator blade-row on NSV, an IGV-rotor configuration is considered in this study.

5.1 Simulation Setup

The mesh topology presented in Section 4.3 and in Fig. 4.1 is followed for the single-passage simulations presented in this Chapter. The rotor tip clearance is modeled with 2 blocks of 21 spanwise grid points using an O-mesh topology of density 101×15. The grid around the blade was constructed as an O-mesh. The mesh size for the IGV and stator is 121(around blade)×51(blade-to-blade)×71(blade span); for the rotor the mesh size is 201(around blade)×51(blade-to-blade)×71(blade span). In Fig. 5.1 are displayed the two-blade-row (IGV-Rotor) and three-blade-row (IGV-Rotor-Stator) mesh configurations used on the left and the right respectively.

An H-mesh layer is used for the matched one-to-one grid point connection at the sliding BC interface of IGV/rotor/stator that enables variable exchange in a fully conservative manner. The dimensions of the interface depend on the blade-row that they belong to. As shown in Fig. 5.2, all H-mesh layers have 6(axial)×71(blade span) mesh dimensions but differ in the tangential dimensions where IGV interface block

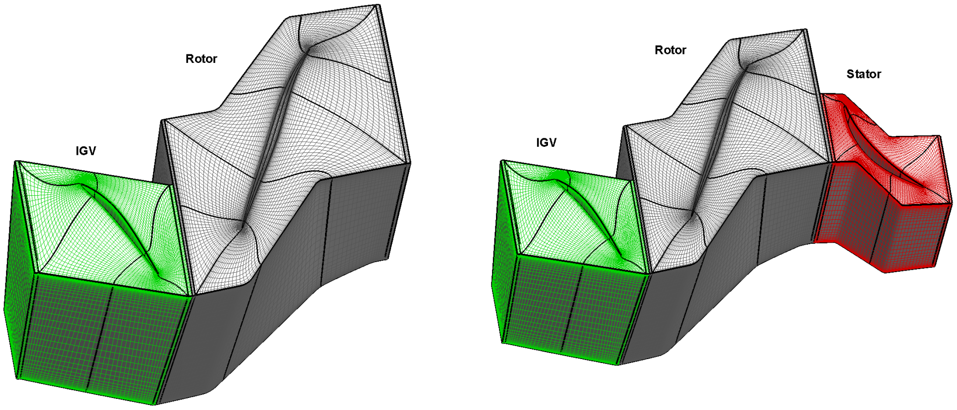

Figure 5.1: Single Passage mesh configurations of IGV-Rotor (left) and IGV-Rotor-Stator (right) for NSV simulation.

has 25 tangential grid points, Rotor interface blocks have 40 tangential grid points, and Stator interface block has 20 tangential grid points. This is proportional to the blade-blade angles for each blade row to ensure one-to-one mesh connectivity during unsteady simulations. In total the single-passage mesh has 22 blocks and a size of 1,282,416 for the IGV-Rotor configuration, and 30 blocks and a size of 1,737,597 for the IGV-Rotor-Stator configuration

The same numerical probes used for the full-annulus simulation in Chapter 4 are used in the single-passage simulations.

5.2 Results and Discussion

Steady flow simulations are conducted using a single passage of the compressor at different back pressure conditions to obtain the speedline. The speedline obtained from steady state simulations is shown in Fig. 5.3 with unsteady single-passage operating conditions shown to provide context. Since all simulations operate near a section of the speedline with a negative slope, it can be assumed that the operating

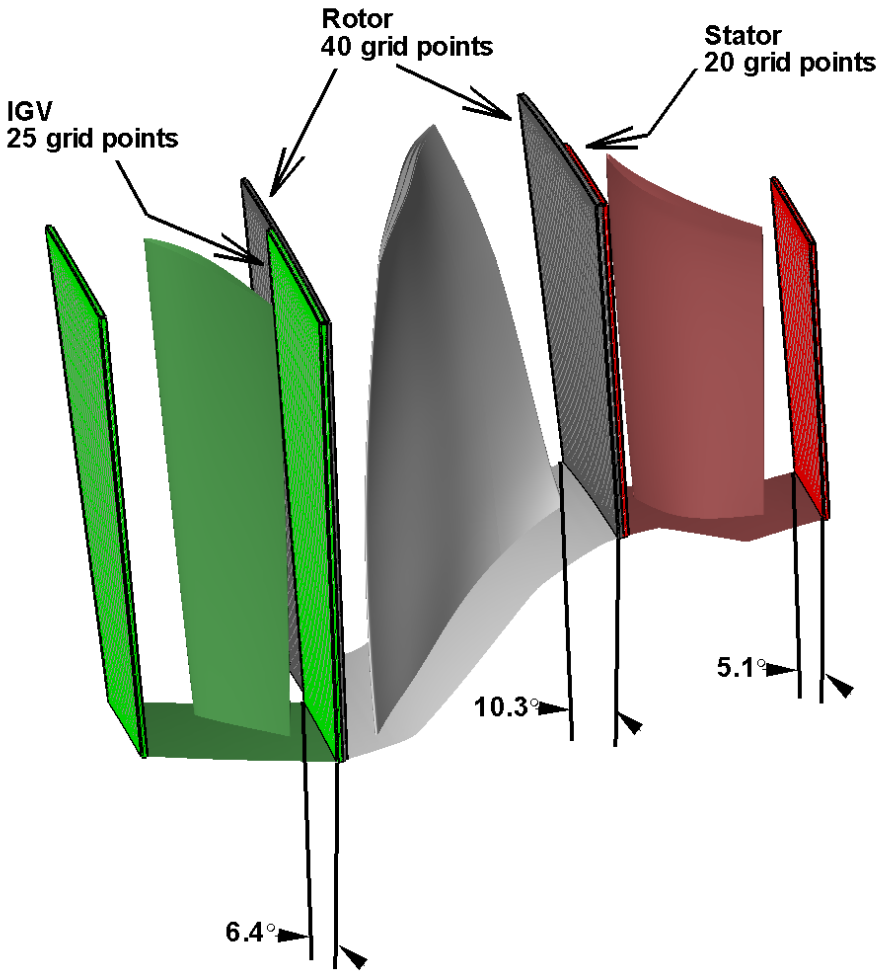

Figure 5.2: Single Passage sliding interface H-mesh layers with inter blade passage angles and tangential grid points for each blade row.

condition for these simulations is within the stable operating range of the compressor stage and that the flowfield is not stalled. Unsteady data points are averages of the last 2 rotor revolutions to avoid the transitional period since the unsteady computations are started from the steady solutions obtained by a mixing plane approach [87]. The numerical residual is reduced by three orders of magnitude within each physical time step, which is usually achieved within 15 to 20 pseudo time step iterations. A non-dimensional time step of about 0.005 is used.

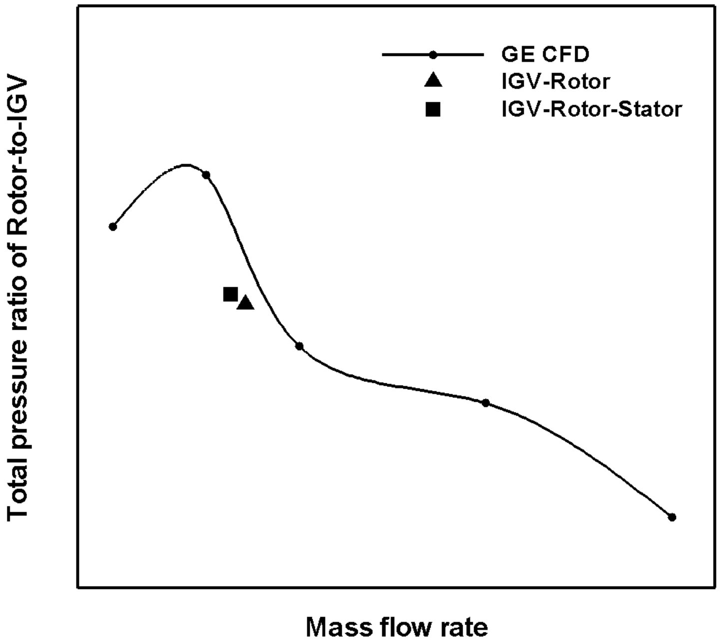

Figure 5.3: Total pressure ratio of IGV-to-Stator versus mass flow rate at the rotor exit.

5.2.1 NSV Excitation Prediction

5.2.1.1 Periodic simulations ($ND = 0$)

The rig testing of the axial compressor with 1.1% tip clearance [10] is shown to have the NSV frequency range of 2600 Hz to 2661 Hz as shown in Fig. 1.1; the measured compressor NSV is at 2600 Hz at the present simulation operating condition of 12880 RPM. The numerically captured NSV frequency for the full annulus configuration is 2439 Hz, as shown in Fig 4.16. In Fig. 5.4 the comparison between periodic single-passage unsteady simulations shows that, at 77% blade span near the LE on the suction surface, the two-blade-row configuration has a 2291 Hz NSV excitation frequency and the three-blade-row configuration predicts a 2365 Hz NSV excitation frequency with a significantly lower amplitude.

When the same measurements are presented at the 92% span location the tip flow instability effect is stronger in the three-blade-row configuration as shown in Fig. 5.5. In contrast, NSV excitation frequencies captured by the full-annulus and two-blade-row simulations decrease in amplitude showing that the flow instability is farther from the blade tip for these configurations.

Fig. 5.6 shows the frequency content of the IGV-Rotor two blade flow at different locations along the rotor blade span. Results for the full-annulus configuration in Fig. 4.13 differ in the sensitivity to harmonics of NSV excitation frequencies and to engine order pressure waves. It seems that boundary conditions have an effect due to wave reflection. However, excitation due to flow instabilities causing the NSV are dominant at the 77% consistent with the measurement. Thus the objective of capturing NSV excitation frequencies with a reduced domain such as a single-passage two-blade-row

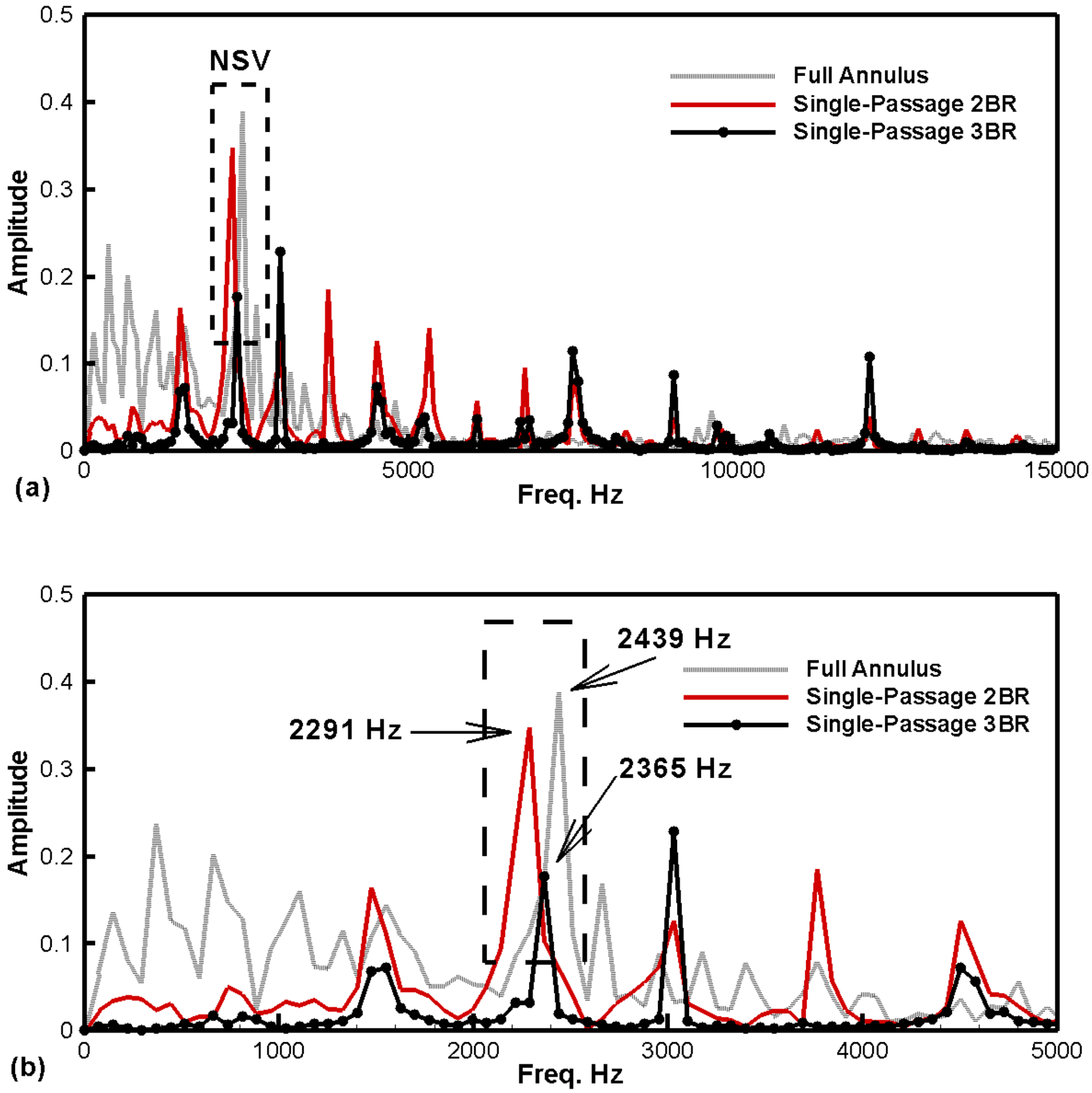

Figure 5.4: Predicted NSV frequencies for a sample blade of full annulus simulation and periodic single-passage simulations at 77% span near LE showing NSV region (a) and detail view with NSV peak frequencies (b)

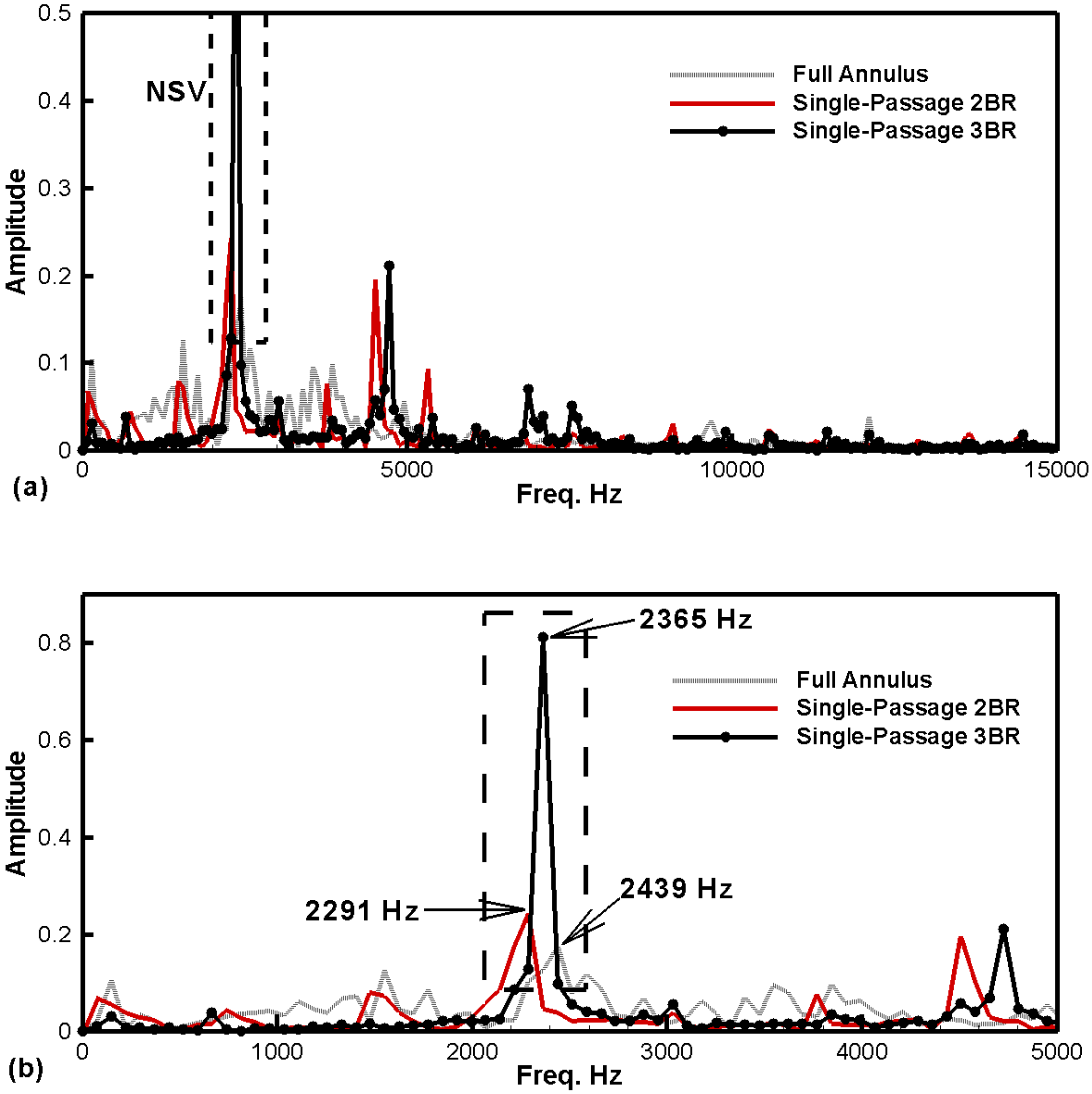

Figure 5.5: Predicted NSV frequencies for a sample blade of full annulus simulation and periodic single-passage simulations at 92% span near LE showing NSV region (a) and detail view with NSV peak frequencies (b)

configuration is achieved. Another observation is that the lower frequency content close to the SFV regime is not as prominent as observed in the full-annulus results. It seems that there is difficulty capturing all flow phenomena with only one passage and no effects from the stator blade-row considered; nonetheless, the trade-off of reducing computational costs over the qualitative loss of detail captured by the single-passage is not very significant since the simulation is able to capture NSV with only 2% of the computational resources required for a full-annulus simulation and 12% of the required computational resources required by a 1/7 annulus sector configuration.

Comparing Fig. 5.6 to the results shown in Fig. 5.7 for a three-blade-row simulation with periodic BCs, tip flow instabilities are suspect of having a big influence on the NSV excitation frequency. Frequencies from engine order excitations and harmonics of NSV excitation frequency from the two-blade row simulation are less prominent than those from the three-blade row simulation near the blade tip above 92% of span. However engine order excitations of higher frequency response are more dominant in the three-blade-row simulation compared to the two-blade-row simulation. The higher engine order frequencies can be explained by the fact that not only is the IGV blade-row interaction being captured, but also the influence of the downstream stator blade-row is captured and the effects are enhanced. Since the blade count for the stator row is 70, it should be expected that higher engine order frequencies would be excited, which is clearly captured in the signal captured for blade spans 77% and below. Fig. 5.8 is a sketch of the expected interactions between blade-row wakes and potential waves for a three-blade-row configuration; these interactions are capture in both the two- and three-blade-row configurations successfully, showin in Fig. 5.9.

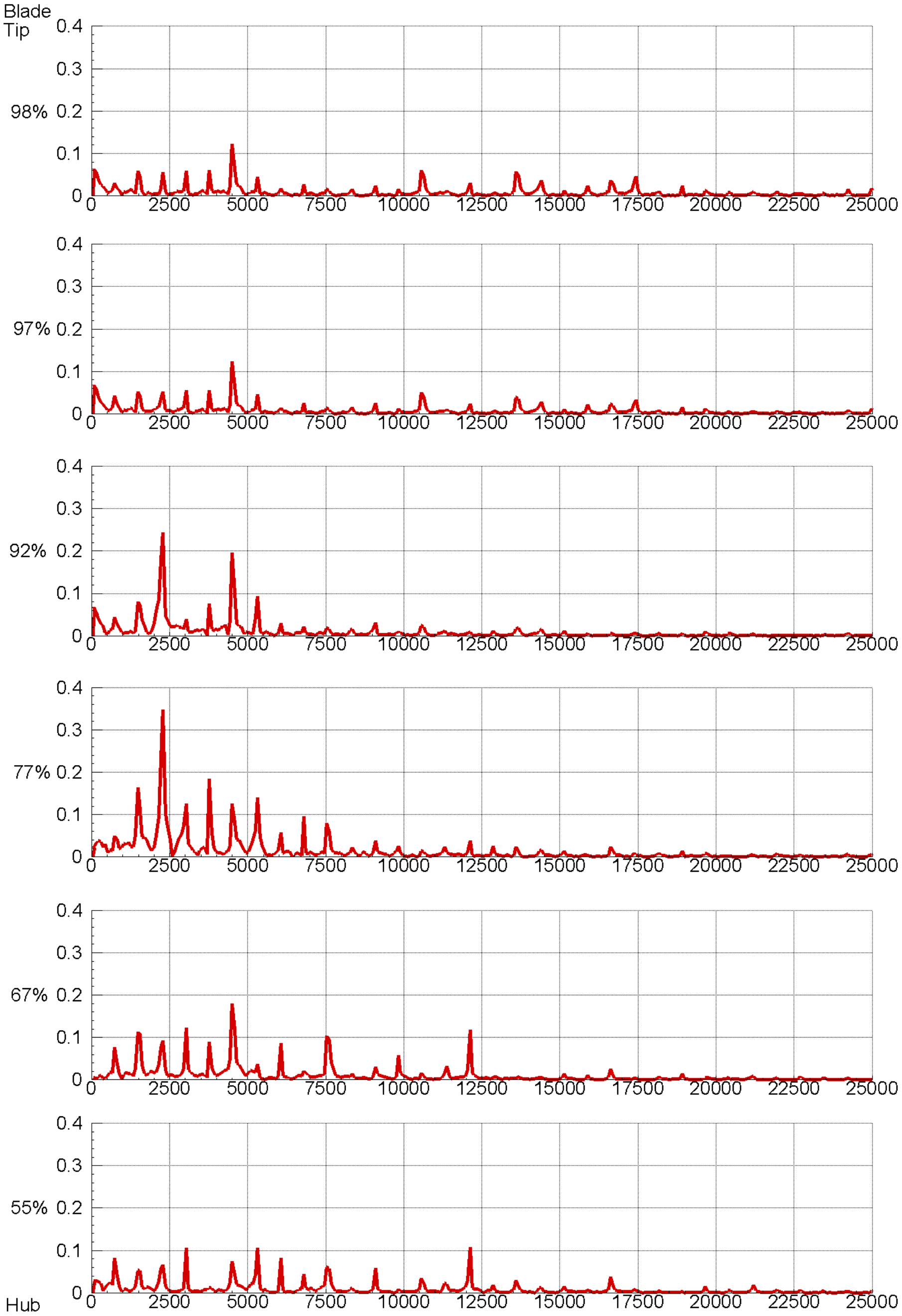

Figure 5.6: Predicted frequencies at different span locations near LE for IGV-Rotor configuration with periodic boundary conditions.

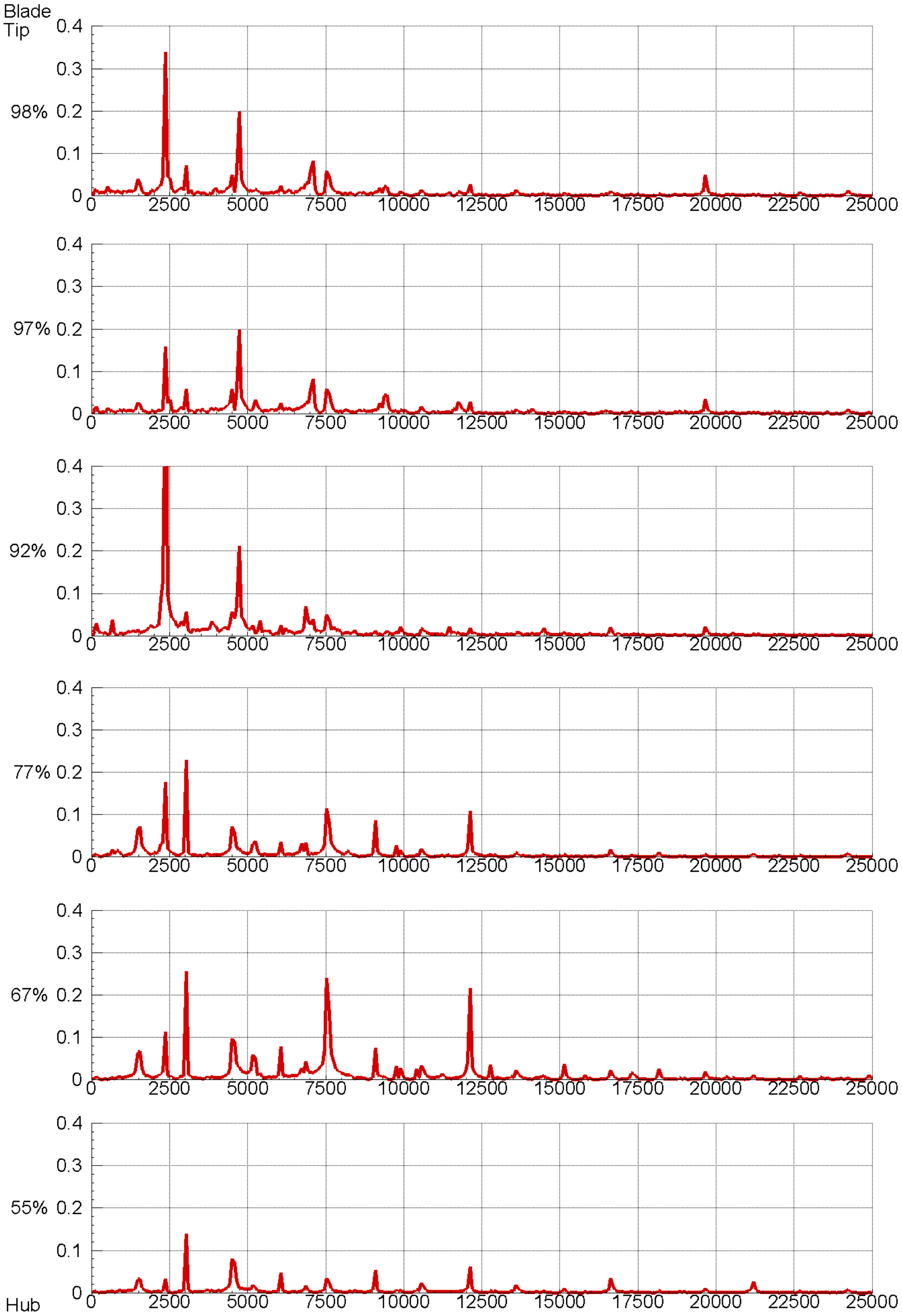

Figure 5.7: Predicted frequencies at different span locations near LE for IGV-Rotor-Stator configuration with periodic boundary conditions.

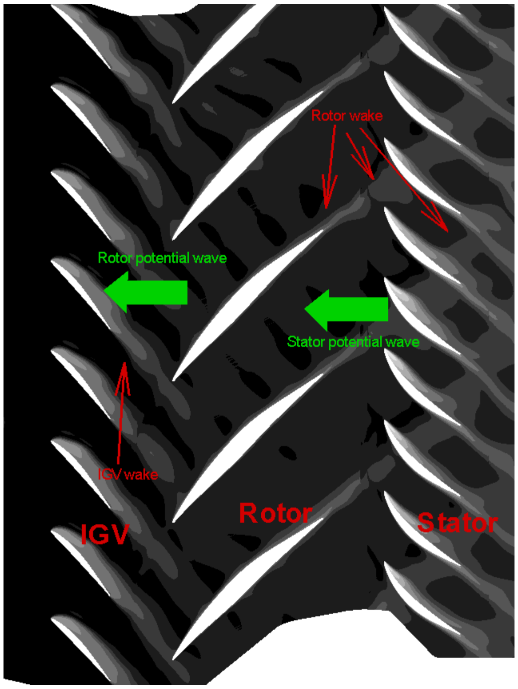

Figure 5.8: Sketch of possible IGV-Rotor-Stator interactions from [5].

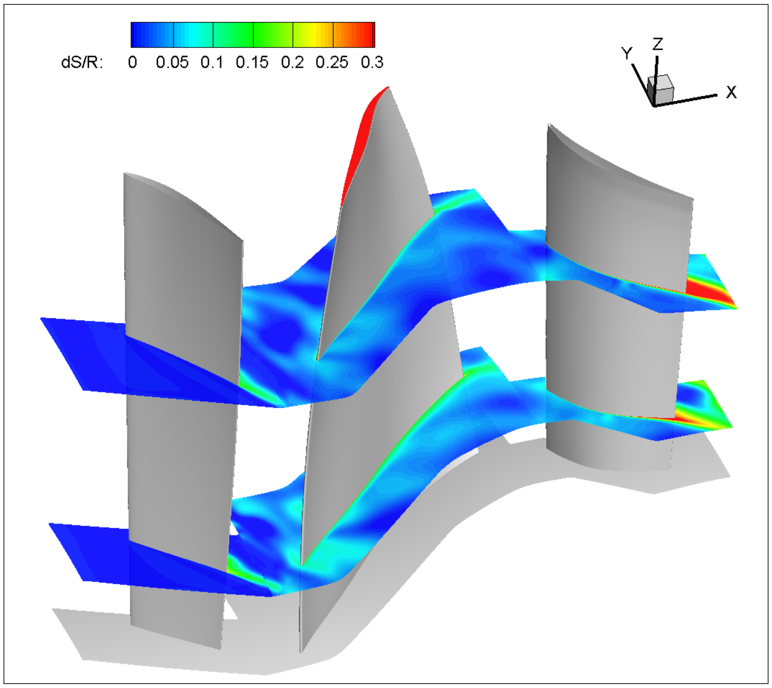

Figure 5.9: Entropy contours showing IGV-Rotor-Stator interactions.

When looking at the flow instabilities for each configuration a clear understanding is formed of why the location for excitation is different between the two- and three-blade-row configurations. Vortical structures in the rotor passage are shown in Fig. 5.10 for the two-blade-row configuration. The circumferentailly travelling vortex structure is the same as the one simulated in Chapter 4, and the streamwise travelling vortex has been observed for some passages in the full-annulus simulation [89]. This is not a surprise since the frequency response captured by the artificial pressure probes is the same as the full annulus simulation. The three-blade-row configuration rotor flow structure shown in Fig. 5.11 only has the tip vortex shedding travelling downstream above the 90% span location approximately. This explains why excitation frequencies have a higher amplitude for span locations above 90% in the frequency map in Fig. 5.7. This shows that there can be an effect by the stator blade row for NSV.

An explanation for this difference in tip flow instabilities is that, as observed previously, a periodic BC enhances the excitation coming from engine order flow structures for small domains. When the influence of IGV wake and Stator potential wave interact with each other, the flow becomes more unstable due to unsteadiness and endwall effects cause tip vortex shedding to be strengthened while dissipating the circumferentially travelling vortex. Since the periodic BC may be the cause for this amplification of engine order excitations due to wave reflection, phase-lag treatment at the interface and circumferential boundaries is implemented to attempt to filter some of these waves by imposing a disturbance wavelength greater than one rotor passage.

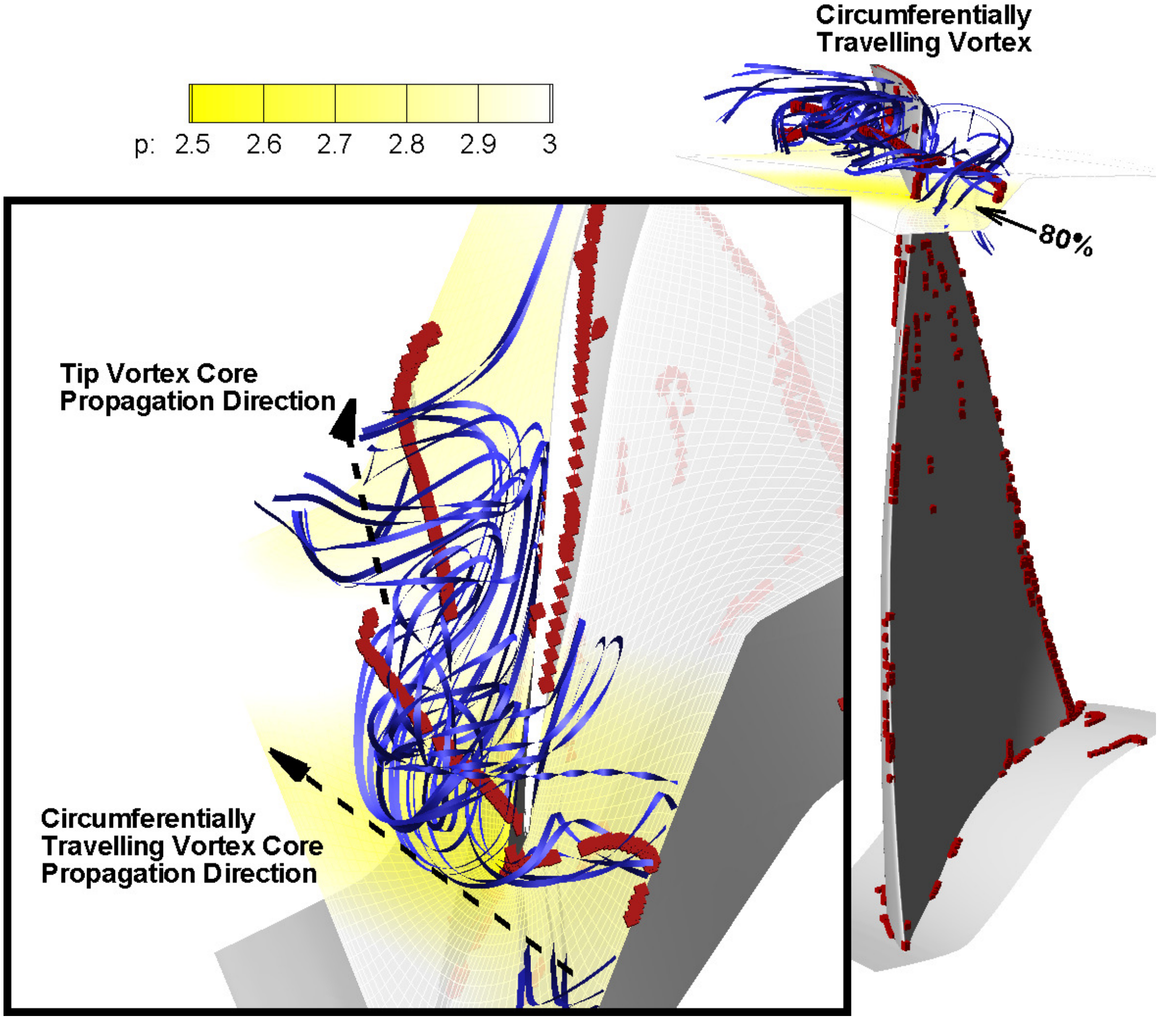

Figure 5.10: Rotor passage flow structure for IGV-Rotor configuration. Circumferentially travelling vortex structure above 80% span with a tip vortex travelling streamwise (static pressure contours)

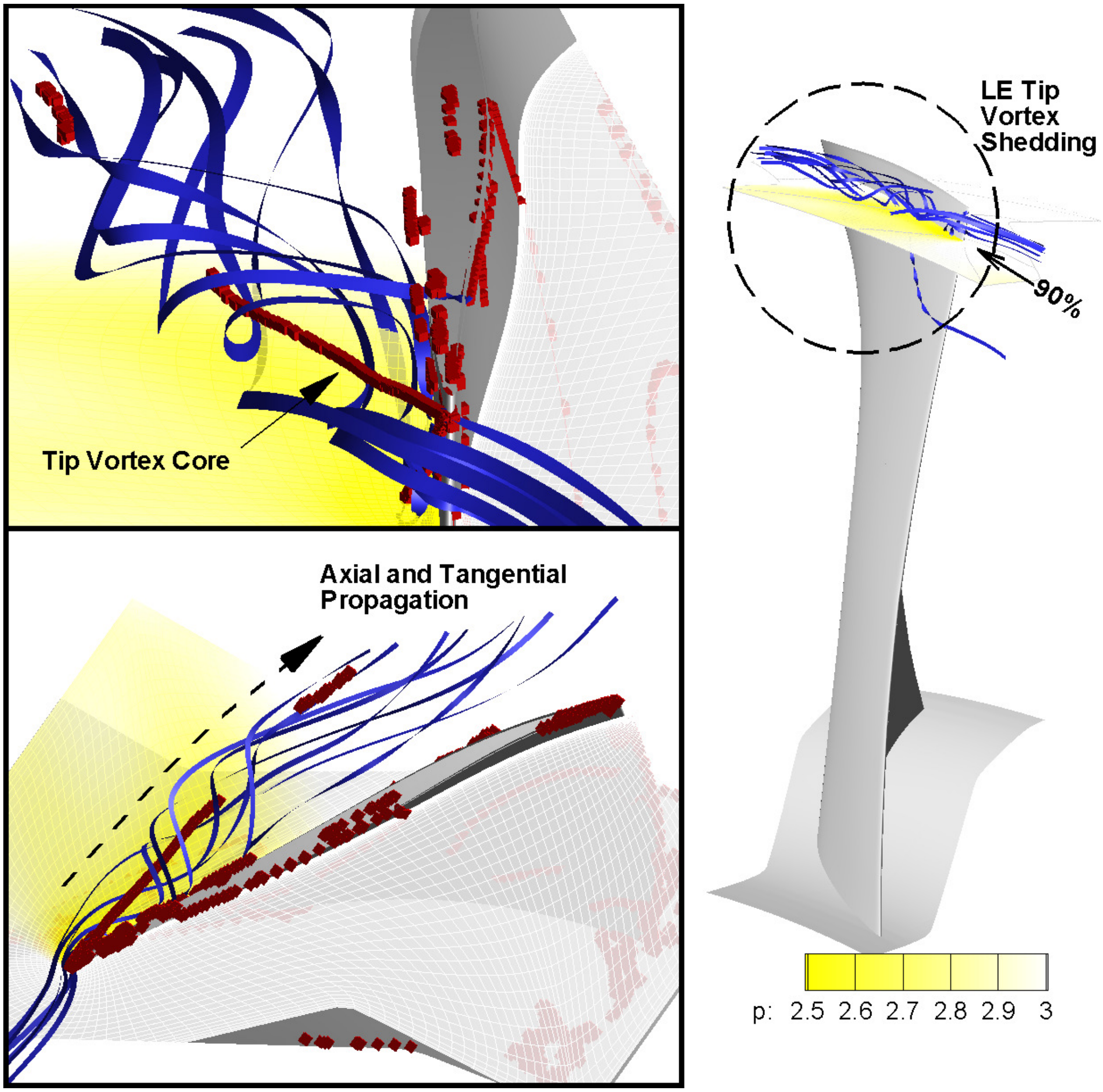

Figure 5.11: Rotor passage flow structure for IGV-Rotor-Stator configuration. Tip vortex structure shedding above 90% span travelling in streamwise direction (static pressure contours)

5.2.1.2 Phase-lag simulations ($ND \neq 0$)

The first test of the effect of Direct Store phase-lag on NSV was performed using a nodal diameter ND=5 for the three-blade row 1-1/2 stage compressor. The circumferential BC assumes a backward travelling wave while the sliding interface used the periodic assumption to observe the effects of phase-lag enforcement on the circumferential boundaries. The results show no difference for the three-blade-row configuration using periodic BC. The frequency signature from pressure probes is exactly the same as in Fig. 5.7 as shown in Fig. 5.12, fluid structure is also the same and is shown in Fig. 5.11.

The results of implementing a Direct Store phase-lag on the sliding interface while maintaining circumferential periodic BC are shown in Fig. 5.13. A nodal diameter of ND=7 is enforced and the results show that effects from NSV excitation are not captured. When looking into the flow structures, the circumferentially travelling vortex is present, but the streamwise tip vortex is not present in the flowfield, as shown in Fig. 5.14. The implication of these results is that while the flow instability, which can be the cause for NSV excitation, may be present in the rotor passage, it does not necessarily translate into a pressure response with a clear NSV excitation frequency and dominant amplitude.

Baumgartner et al. [6] provides an important explanation to the difference between a Rotating Instability (RI), known to have caused NSV in some compressors, and a rotating stall cell. Both flow instabilites rotate around the blade row from blade to blade, and they both can have a long (small ND) or a short (large ND) circumferential wavelength. However the main difference is that RI has been measured as a range of

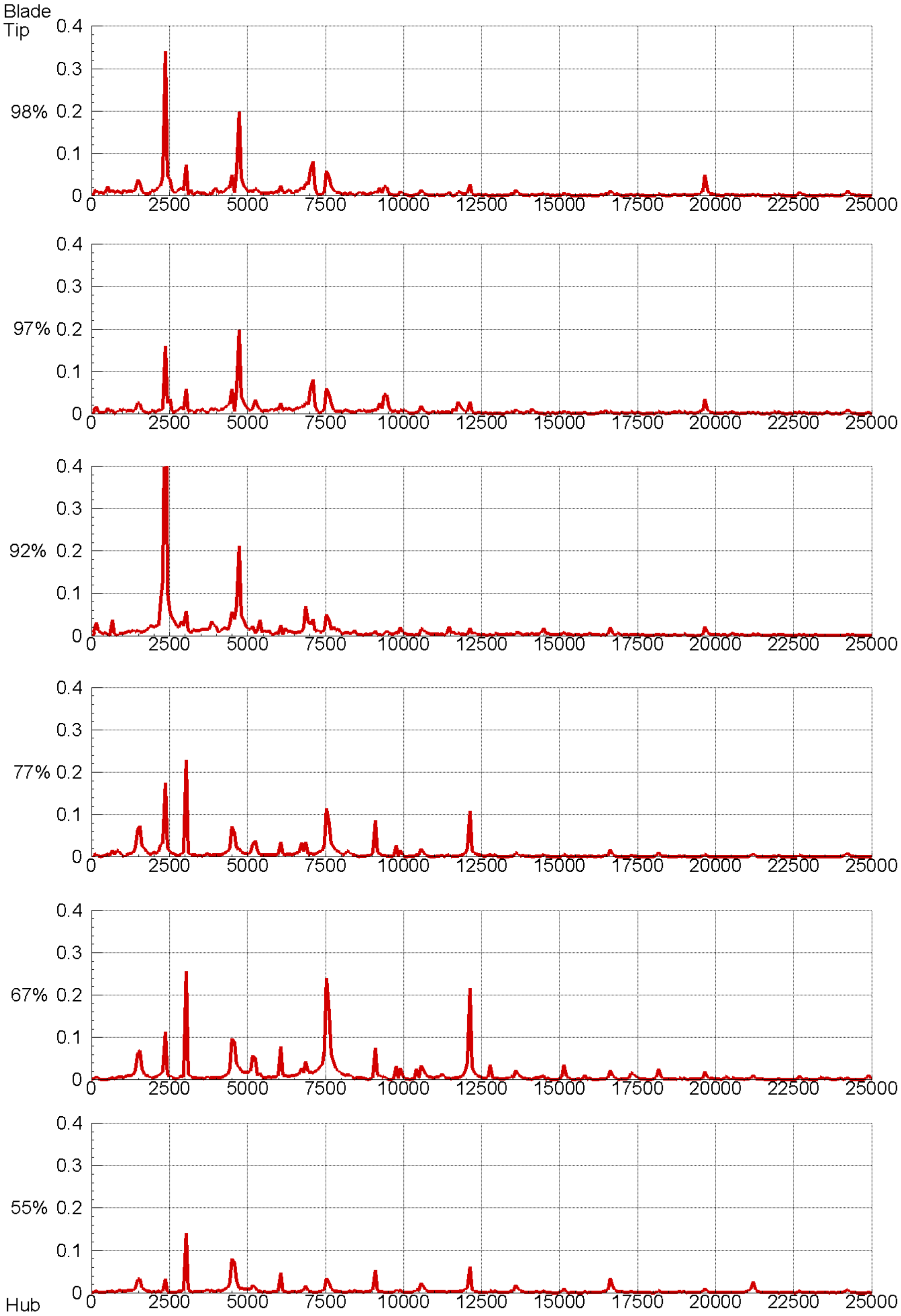

Figure 5.12: Predicted frequencies at different span locations near LE for IGV-Rotor-Stator configuration with phase-lag for ND=5 at circumferential BC only.

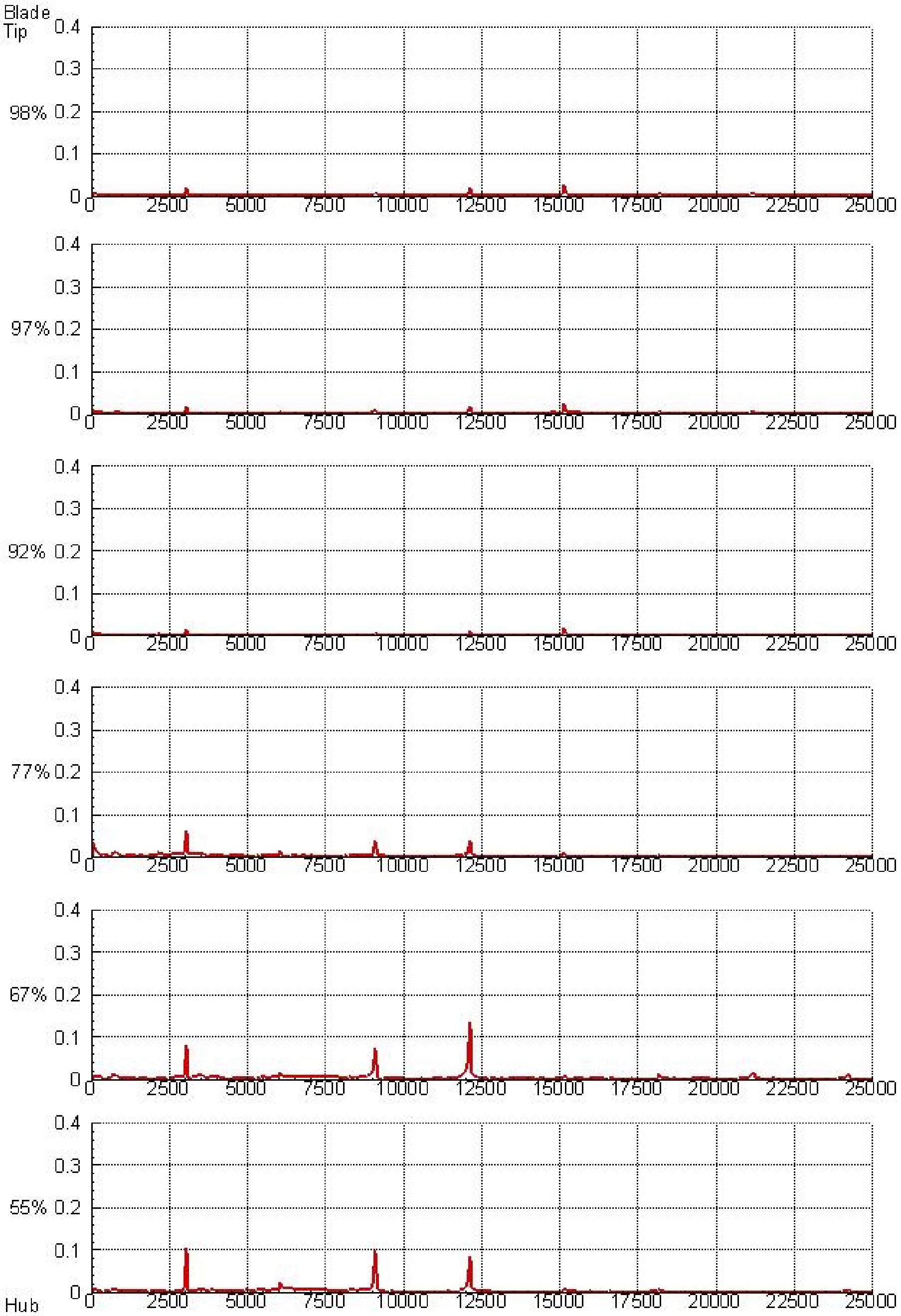

Figure 5.13: Predicted frequencies at different span locations near LE for IGV-Rotor-Stator configuration with phase-lag for ND=7 at sliding interface BC.

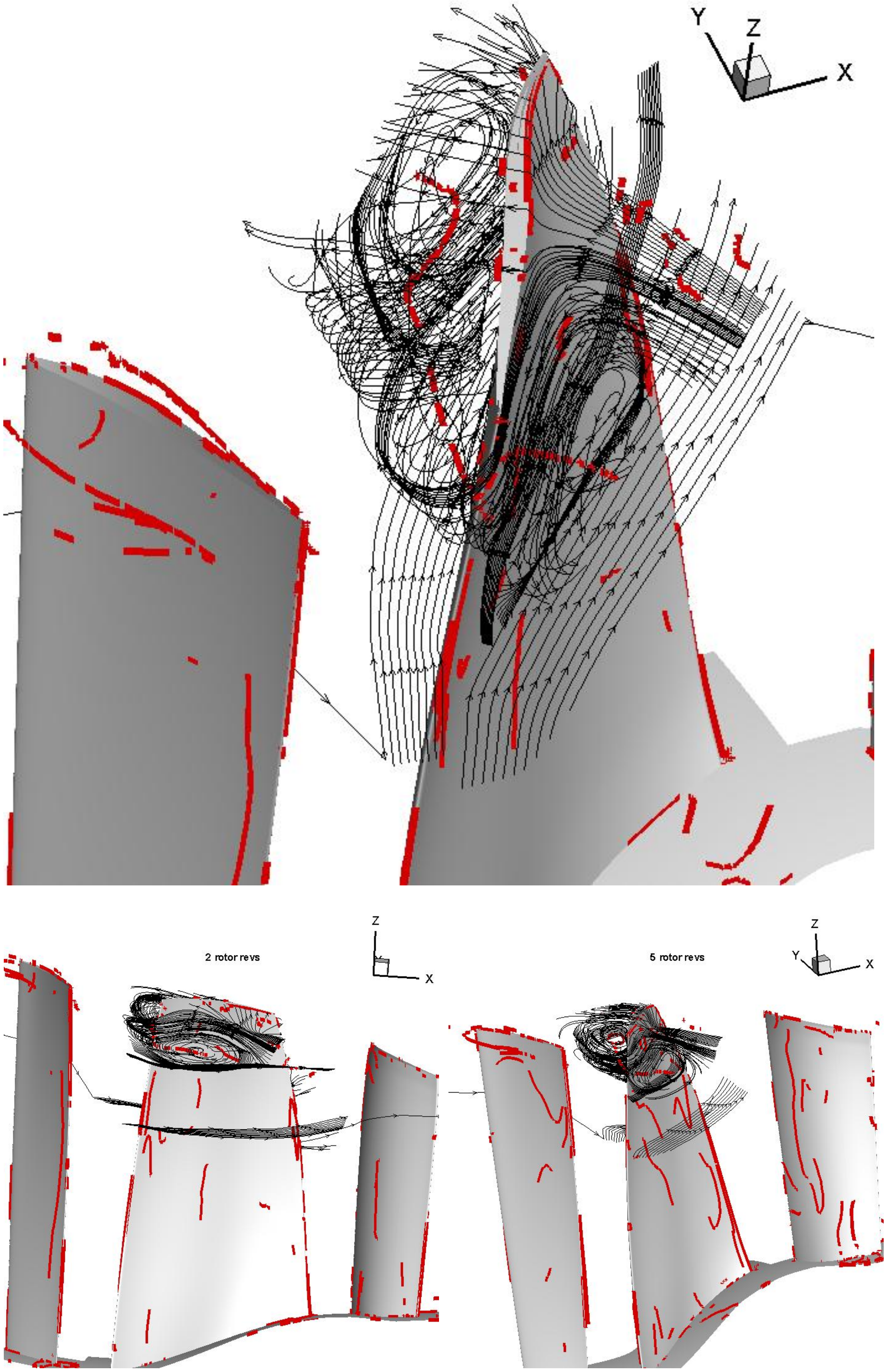

Figure 5.14: Rotor passage flow structure for IGV-Rotor-Stator configuration. Circumferentially travelling vortex structure above 80% span with no tip vortex travelling streamwise.

frequencies with a characteristic frequency signature due to pressure variation, but rotating stall has no pressure variation therefore it presents itself as a single discrete frequency, as illustrated in Fig. 5.15.

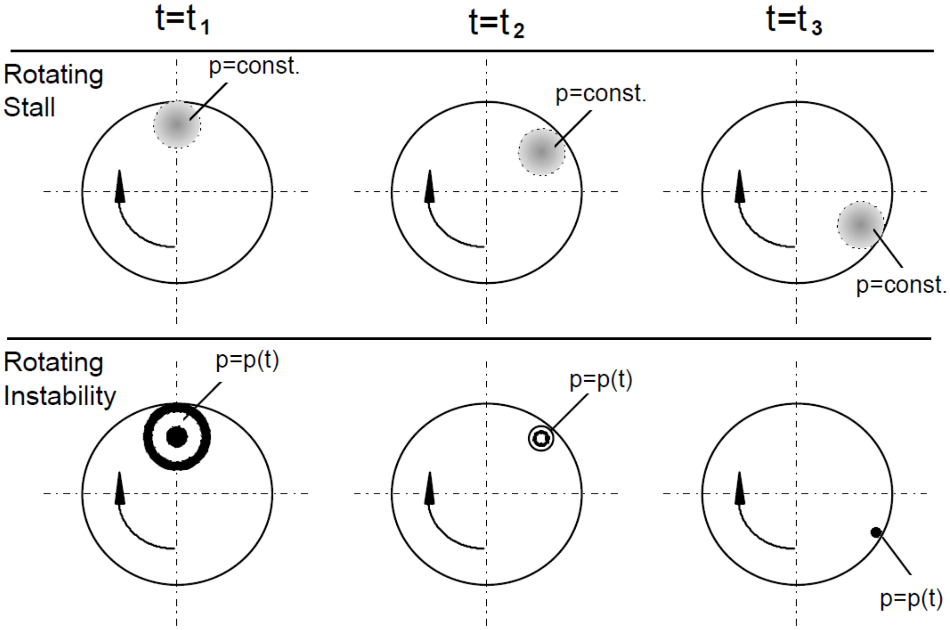

Figure 5.15: Illustration of the difference between a RI and rotating stall due to pressure variation in RI (plot adopted from [6]).

Vo [16] explains that rotating instabilities occur when one of the the two criteria for spike stall inception is satisfied; namely, tip clearance backflow below the trailing-edge blade tip. This means that conditions for flow instabilities to transform into spike-type stall cells could exist. Since the conditions under which the three-blade-row configuration simulations is performed are close to the wheel speed where NSV is not present anymore (see Fig. 1.1) it is plausible that engine order stimulation can cause the RI to simply become a contained stall cell, where only the upper spans of the blade are stalled but the flow remains stable at spans below 75% (see Fig. 5.14).

5.2.2 NSV Excitation frequencies summary

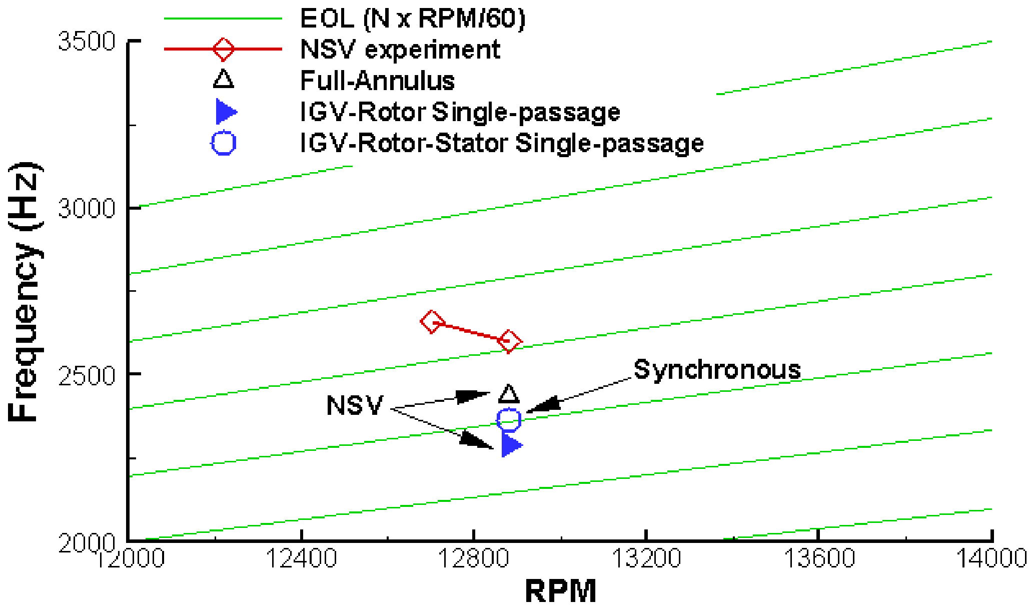

Figure 5.16: Campbell diagram summarizing single-passage results.

Fig. 5.16 summarizes the results of the single-passage simulations that exhibited peak frequency signals near the peak NSV excitation captured by the full-annulus simulation. Both the full-annulus simulation and the two-blade-row configuration with periodic interface and circumferential BCs capture excitation frequencies that are not synchronous to the engine order, similarly their rotor passage flow exhibit circumferentially travelling vortices above 80% span and streamwise travelling vortices shed at the tip region.

It should be pointed out that in Fig. 5.16 it is found that the three-blade-row single-passage simulation captures an excitation frequency synchronous to an engine order of 11. This further reinforces that the tip vortex shedding mechanism found in the rotor passage is driven by the interaction between IGV wake propagation and

Stator potential wave propagation. As discussed above, this is due to the reflective nature of the boundary conditions, which enhance the effect of rotor-stator interactions, inducing the forced response nature of the frequency signature shown in Fig. 5.7.

5.3 Conclusion

Single-passage simulations of a GE 1-1/2 stage axial compressor have been performed for an IGV-Rotor and an IGV-Rotor-Stator configuration and compared to available rig test data and full-annulus simulations. Steady-state simulations where carried out to ensure unsteady simulations would be performed under stable operating conditions. A fully-conservative sliding interface BC was implemented with phase-lag capabilities using the Direct Store method. Also Direct Store phase-lag was applied to the circumferential BCs to enforce longer disturbance wavelengths.

Simulations without phase-lag enforced (ND=0) at the boundaries were carried out where the two-blade-row configuration captured a 2291 Hz NSV excitation frequency and the three-blade-row configuration predicted a 2365 Hz NSV excitation frequency with a significantly higher amplitude above 90% span. This correlates closely to the predicted NSV excitation frequency of 2439 Hz for the full-annulus configuration. The two-blade-row configuration exhibited the same vortex structures captured in the full-annulus study, namely a circumferentially travelling vortex and a streamwise vortex that are considered the RI causing the NSV excitation. The three-blade-row only captured a tip vortex shedding at the LE, which can be attributed to the reflective nature of the BCs causing IGV-rotor-stator interactions to be augmented, becoming dominant and shifting NSV excitation response to engine order regime.

Phase-lag with a ND of 5 was enforced for the circumferential BCs for the three-blade-row configuration, and the results exactly matched the frequency response and flow structures of the periodic simulation. Another single-passage simulation was performed, this time isolating the effect of phase-lag to the sliding interface between blade-rows. A ND of 7 was enforced, however the NSV excitation completely dissapeared and only effects from IGV-Rotor-Stator interactions were captured by the artificial pressure probes. Nonetheless, in the rotor blade passage was captured a circumferentially travelling vortex similar to those observed in the full-annulus and two-blade-row simulations. This can be attributed to the fact that the condition in which the simulations where performed are very close to wheel speeds where the system no longer exhibits NSV. This can occur when the RI responsible for the NSV no longer maintains a pressure variation with a characteristic frequency signature as it rotates relative to the rotor rotation, and now has become the beginning of a spike-type stall cell. In this scenario the travelling vortex has become evidence of part-stall of the upper spans of the rotor blade, but stalling is contained maintaining stable operation.

In conclusion, an efficient method of capturing NSV excitation has been proposed in a high-fidelity manner, where only 2% of the computational resources used in a full annulus simulation are required for an accurate single-passage simulation.

CHAPTER 6

Conclusion

The objective of this research is twofold:

1. to investigate and confirm the periodicity of the NSV mechanism of a GE axial compressor with a full-annulus simulation
2. to develop a high fidelity single-passage tool with time-accurate unsteady capabilities able to capture rotor-stator interactions and NSV

Therefore, in this thesis a high fidelity methodology for axial turbomachinery simulation is developed using the low diffusion shock-capturing Riemann solver with high order schemes, the Spalart-Allmaras turbulence closure model, the fully conservative unsteady sliding BC for rotor-stator interaction with extension to full-annulus and single-passage configurations, and the phase lag boundary conditions applied to rotor-stator interface and circumferential BC. Validation is achieved to demonstrate high accuracy and robustness of the high fidelity simulation methodology with a GE 1-1/2 stage high-speed compressor, simulated using a full-annulus configuration to investigate the NSV aerodynamic excitation without circumferential sector boundary condition effect and compared it to strain gage measurements. Single-passage simulations have been performed for IGV-rotor and IGV-rotor-stator configurations and compared to available strain gage rig test data and full-annulus simulations.

A URANS solver is used and captures the NSV flow excitation frequency of 2439 Hz, which agrees reasonably well with the measured NSV frequency of 2600 in the rig test. The phenomena observed confirms for the most part the results obtained using 1/7 annulus URANS simulation with a circumferential time-shifted phase-lag BC. It is observed that the circumferentially traveling vortex formed in the vicinity of the rotor tip propagates at the speed of a non-engine order frequency and causes the NSV. The vortex travels along the suction surface of the blade and crosses the passage outlet near blade trailing edge. Such a vortex motion trajectory repeats in each blade passage and generates two low pressure regions due to the vortex core positions, one at the leading edge and one at the trailing edge, both are oscillating due to the vortex coming and leaving. These two low pressure regions create a pair of coupling forces that generates a torsion moment causing NSV.

The full-annulus simulation shows that the circumferentially traveling vortex has fairly periodical behavior and is a full annulus structure. Also, frequencies below the NSV excitation frequency of 2439 Hz with large amplitudes in response to flow-separation related phenomena are present. This behavior is consistent with experimental measurements.

For circumferentially averaged parameters like total pressure ratio, NSV is observed to have an effect, particularly at radial locations above 70% span. Therefore, to achieve similar or better total pressure ratio a design with a smaller loading of the upper blade span and a higher loading of the mid blade spans should be considered.

A fully-conservative sliding interface BC was implemented with phase-lag capabilities using the Direct Store method for single-passage simulations. Also Direct Store phase-lag was applied to the circumferential BCs to enforce longer disturbance wavelengths.

Simulations without phase-lag enforced (ND=0) at the boundaries were carried out where the two-blade-row configuration captured a 2291 Hz NSV excitation frequency and the three-blade-row configuration predicted a 2365 Hz NSV excitation frequency with a significantly higher amplitude above 90% span. This correlates closely to the predicted NSV excitation frequency of 2439 Hz for the full-annulus configuration. The two-blade-row configuration exhibited the same vortex structures captured in the full-annulus study, namely a circumferentially travelling vortex and a streamwise travelling vortex which are considered the RI causing the NSV excitation. The three-blade-row only captured a tip vortex shedding at the LE, which can be attributed to the reflective nature of the BCs causing IGV-rotor-stator interactions to be augmented, becoming dominant and shifting NSV excitation response to engine order regime.

Phase-lag with a ND of 5 was enforced for the circumferential BCs for the three-blade-row configuration, and the results exactly matched the frequency response and flow structures of the periodic simulation, illustrating the small effect that phase-lag has on strongly periodic flow disturbances. Another single-passage simulation was performed, this time isolating the effect of phase-lag to the sliding interface between blade-rows. A ND of 7 was enforced, however the NSV excitation completely dissapeared and only effects from IGV-Rotor-Stator interactions were captured by the artificial pressure probes. Nonetheless, in the rotor blade passage was captured a circumferentially travelling vortex similar to those observed in the full-annulus and two-blade-row simulations. This can be attributed to the fact that the condition in which the simulations where performed are very close to wheel speeds where the system no longer exhibits NSV. This can occur when the RI responsible for the NSV no longer maintains a pressure variation with a characteristic frequency signature as it rotates relative to the rotor rotation, and now has become the beginning of a spike-type stall cell. In this scenario the travelling vortex has become evidence of part-stall of the upper spans of the rotor blade, but stalling is contained maintaining stable operation.

In conclusion, an efficient method of capturing NSV excitation has been proposed in a high-fidelity manner, where only 2% of the computational resources used in a full annulus simulation are required for an accurate single-passage simulation.

6.1 Future Work

Hybrid turbulence closure models between LES/SA exist, namely Detached Eddy Simulation (DES) and its iterations: Delayed Detached Eddy Simulation (DDES) and Improved Delayed Detached Eddy Simulation (IDDES). This are high fidelity treatments of turbulence, however they require higher mesh density than a typical URANS simulation would require. For this reason application of DES and its variants should be done to a higher density mesh single-passage simulation to resolve the small scale structures that may contribute to mixing between tip leakage flow, main flow and vortical instabilites.

Also a Fluid-Structure Interaction (FSI) methodlogy could be implemented to the current full-annulus and single-passage methodologies. By allowing the blades to vibrate a further understanding of the lock-in nature of NSV can be pursued. Future work should include a full-annulus simulation with vibrating blades to determine the influence of blade modal frequencies coupling with flow frequencies and how this fluid-structure interaction affects NSV, and by extension, application of the approach to single-passage configurations to give accessibility to designers in industry fully aeroelastic design tools able to predict vibratory response earlier in the engine development process.

Bibliography

[1] J.I. Erods, E. Alzner, and W. McNally, “Numerical Solution of Periodic Transonic Flow Through a Fan Stage,” *AIAA Journal*, vol. 15, pp. 1559–68, Nov. 2004.

[2] M.B. Giles, “Stator/Rotor Interaction in a Transonic Turbine,” *AIAA Journal of Propulsion and Power*, vol. 6, pp. 621–627, 1990.

[3] H. D. Li, and L. He, “Blade Aerodynamic Damping Varaition With Rotor-Stator Gap: A Computational Study Using Single-Passage Approach,” *Journal of Turbomachinery*, vol. 127, pp. 573–578, Jul. 2005.

[4] E.J. Hall, “Aerodynamic Modeling of Multistage Compressor Flowfields - Part 1: Analysis of Rotor/Stator/Rotor Aerodynamic Interaction.” ASME 97-GT-344, 1997.

[5] H. D. Li, and L. He, “Toward Intra-Row Gap Optimization for One and Half Stage Transonic Compressor,” *Journal of Turbomachinery*, vol. 127, pp. 589–598, Jul. 2005.

[6] M. Baumgartner, F. Kameier, and J. Hourmouziadis, “Non-Engine Order Blade Vibration in a High Pressure Compressor.” ISABE, Twelfth International Symposium on Airbreathing Engines, Melbourne, Australia, 10-15, 1995.

[7] W.N. Dawes, “Turbomachinery Computational Fluid Dynamics: Asymptotes and Paradigm Shifts,” *Phil. Trans. R. Soc. A*, vol. 365, pp. 2553–2585, doi: 10.1098/rsta.2007.2021, 2007.

[8] C.H. Wu, “A General Through Flow Theory of Fluid Flow with Subsonic or Supersonic Velocity in Turbomachines Having Arbitrary Hubs and Casing Shapes.” NASA TN2388, 1951.

[9] J. Denton, “Loss Mechanisms in Turbomachines,” *AMSE J. of Turbomach.*, vol. 115, pp. 621–656, 1993.

[10] R. Kielb, J. Thomas, P. barter, and K. Hall, “Blade Excitation by Aerodynamic Instabilites - A Compressor Blade Study.” ASME Paper No. GT-2003-38634, 2003.

[11] J. Marz, C. Hah, and W. Neise, “An Experimental and Numerical Investigation Into the Mechanisms of Rotating Instability,” *Journal of Turbomachinery*, vol. 124, pp. 367–375, 2002.

[12] R. Mailach, I. Lehmann, and K. Vogeler, “Rotating Instabilites in an Axial Compressor Originating From the Fluctuating Blade Tip Vortex.” ASME Paper No. GT-2003-38634, 2003.

[13] H.S. Im, and G.C. Zha, “Investigation of Flow Instability Mechanism Causing Compressor Rotor-Blade Nonsynchronous Vibration,” *AIAA Journal*, vol. 52, pp. 2019–2031, doi: 10.2514/1.J052781, 2014.

[14] J. Thomassin, H. Vo, and N. Mureithi, “Blade Tip Clearance Flow and Compressor Nonsynchronous Vibrations: The Jet Core Feedback Theory as the Coupling Mechanism,” *Journal of Turbomachinery*, vol. 131, pp. 11013–1–11013–9, 2009.

[15] J. Thomassin, H. Vo, and N. Mureithi, “The Tip Clearance Flow Resonance Behind Axial Compressor Nonsynchronous Vibration,” *Journal of Turbomachinery*, vol. 133, pp. 041030–1–041030–10, 2011, doi:10.1115/1.4001368.

[16] Vo, H.D., “Role of Tip Clearance Flow in Rotating Instabilities and Nonsynchronous Vibrations,” *Journal of Propulsion and Power*, vol. 26, pp. 556–561, doi: 10.2514/1.26709, 2010.

[17] A. Sanders, “Nonsynchronous Vibration(NSV) due to a Flow-Induced Aerodynamic Instability in a Composite Fan Stator,” *Journal of Turbomachinery*, vol. 127, pp. 412–421, 2005.

[18] S. Clark, R. Kielb, and K. Hall, “Developing a Reduced-Order Model to Understand Nonsynchronous Vibration (NSV) in Turbomachinery.” ASME GT2012-68145, 2012.

[19] H.S. Im, and G.C. Zha, “Simulation of Non-Synchronous Blade Vibration of an Axial Compressor Using a Fully Coupled Fluid/Strcuture Interaction.” ASME GT2012-68150, 2012.

[20] J.Y. Gan, H.S. Im, D.A. Espinal, A. Lefebvre, and G.C. Zha, “Investigation of a Compressor Rotor Non-Synchronous Vibration with and without Fluid-Structure Interaction.” ASME GT2014-26478, 2014.

[21] C. Hah, J. Bergner, and H. Schifer, “Short Length Scale Rotating Stall Inception in a Transonic Axial Compressors : Criteria and Mechanisms.” GT2006-90045, ASME Turbo Expo, 2006, doi:10.1115/GT2006-90045.

[22] H.S. Im, X.Y. Chen, and G.C. Zha, "Detached Eddy Simulation of Stall Inception for a Full Annulus Transonic Rotor." Journal of Propulsion and Power, to appear.

[23] H. Khaleghi, M. Boroomand, A.M. Tousi, and J.A. Teixeira, "Stall Inception in a Transonic Axial Fan," *Journal of Power and Energy*, vol. 222, pp. 199–208, doi:10.1243/09576509JPE407, 2008.

[24] F. Lin, J. Zhang, J. Chen, and C. Nie, "Flow Structure of Short-Length-Scale Disturbance in an Axial-Flow Compressor," *Journal of Propulsion and Power*, vol. 24, pp. 1301–1308, doi: 10.2514/1.36525, 2008.

[25] J.Y. Gan, H.S. Im, and G.C. Zha, "Simulation of Stall Inception of a High Speed Axial Compressor with Rotor-Stator Interaction." AIAA Paper 2015-3932, 51st AIAA/SAE/ASEE Joint Propulsion Conference, Orlando, FL, 2015.

[26] J.Y. Gan, H.S. Im, and G.C. Zha, "Delayed Detached Eddy Simulation of Rotating Stall for a Full Annulus Transonic Axial Compressor Stage." ASME GT2016-57985, 2016.

[27] J. Chen, M. Hathaway, and G. Herrick, "Prestall Behavior of a Transonic Axial Compressor Stage via Time-Accurate Numerical Simulation," *AMSE J. of Turbomach.*, vol. 130, pp. 1–12, doi:10.1115/1.2812968, 2008.

[28] J. Chen, B. Johnson, M. Hathaway, and R. Webster, "Flow Characteristics of Tip Injection on Compressor Rotating Spike via Time-Accurate Simulation," *Journal of Propulsion and Power*, vol. 25, pp. 678–687, doi: 10.2514/1.41428, 2009.

[29] H. Khaleghi, J. Teixeira, A. Tousi, and M. Boroomand, "Parametric Study of Injection Angle Effects on Stability Enhancement of Transonic Axial Compressors," *Journal of Propulsion and Power*, vol. 24, pp. 1100–1107, doi: 10.2514/1.34817, 2009.

[30] L. He, and J.D. Denton, "Three-Dimensional Time Marching Inviscid and Viscous Solutions for Unsteady Flows Around Vibrating Blades," *Journal of Turbomachinery*, vol. 116, pp. 469–476, 1994.

[31] R. Srivastava, M.A. bakhle, T.G. Keith Jr, and G.L. Stefko, "Aeroelastic Analysis of Turbomachinery: Part I-Phase Lagged Boundary Condition Methods," *International Journal of Numerical Methods for Heat & Fluid Flow*, vol. 14, pp. 366–381, Nov. 2004.

[32] H. D. Li, and L. He, "Single-Passage Analysis of Unsteady Flows Around Vibrating Blades of a Transonic Fan Under Inlet Distortion," *Journal of Turbomachinery*, vol. 124, pp. 285–292, Apr. 2002.

[33] H.-S. Im, and G.-C. Zha, “Prediction of a Transonic Rotor Fluid/Structure Interaction With a Traveling Wave Using a Phase-lag Boundary Condition.” Proceedings of 51st AIAA Aerospace Sciences Meeting including the New Horizons Forum and Aerospace Exposition, Grapevine, Texas, Jan 2013, 2013.

[34] H.-S. Im, and G.-C. Zha, “ Flutter Prediction of a Transonic Rotor Using a Phase-lagged Boundary Condition.” Proceedings of 50th AIAA Aerospace Sciences Meeting including the New Horizons Forum and Aerospace Exposition, Nashville, Tennessee, Jan 2012, 2012.

[35] J.D. Denton, “The Calculation of 3-D Viscous Flow Through Multistage Turbomachines,” *Journal of Turbomachinery*, vol. 114, pp. 18–26, 1992.

[36] W.N. Dawes, “Toward Improved Throughflow Capability: the Use of 3-D Viscous Flow Solvers in a Multistage Environment,” *Journal of Turbomachinery*, vol. 114, pp. 8–17, 1992.

[37] U.K. Singh, “A Computation and Comparison With Measurements of Transonic Flow in an Axial Compressor Stage With Shock and Boundary-Layer Interaction,” *Journal of Engineering Gas Turbine Power*, vol. 104, pp. 510–515, 1982.

[38] J.W. Barter, P.H. Vitt, and J.P. Chen, “Interaction Effects in a Transonic Turbine Stage.” ASME paper 2000-GT-0376, Proceedings of ASME Turboexpo 2000, May 8-11 2000, Munich Germany, 2000.

[39] G. Fritch and M.B. Giles, “An Asymptotic Analysis of Mixing Loss.” ASME paper 93-GT-345, 1993.

[40] M. Rai, “Three-dimensional Navier-Stokes Simulations of Turbine Rotor-Stator Interaction. I - Methodology ,” *AIAA Journal of Propulsion and Power*, vol. 5, pp. 305–311, 1989.

[41] L. He, “Three-Dimensional Unsteady Navier-Stokes Analysis of Stator-Rotor Interaction in Axial Flow Turbines,” *Proceedings of the Institution of mechanical Engineers, Part A: Journal of Power and Energy*, vol. 214, pp. 13–22, 2000.

[42] A. Ruprecht, C. Bauer, C. Gentner, and G. Lein, “Parallel Computation of Stator-Rotor Interaction in an Axial Turbine.” ASME PVP Conference, CFD Symposium, Boston, 1999.

[43] J.P. Chen, and J.W. Barter, “ Comparison of Time-Accurate Calculations for the Unsteady Interaction in Turbomachinery Stage.” AIAA Paper 98-3292, 1998.

[44] M. Zaki, L. Sankar, and S. Menon, “Hybrid Reynolds-Averaged Navier-Stokes/Kinetic-Eddy Simulation of Stall Inception in Axial Compressors,” *Journal of Propulsion and Power*, vol. 26, pp. 1276–1282, doi: 10.2514/1.50195, 2010.

[45] R. Davis, and J. Yao, "Computational Approach for Predicting Stall Inception in Multistage Axial Compressor," *Journal of Propulsion and Power*, vol. 23, pp. 257–265, doi: 10.2514/1.50195, 2007, doi: 10.2514/1.18442.

[46] L. Castillon, "Evaluation of a Multiple Frequency Phase Lagged Method for Unsteady Numerical Simulations of Multistage Turbomachinery." 28th Int. Congress Aeronautical Sciences, 2012.

[47] L. Castillon, N. Gourdain, and X. Ottavy, "Multiple-Frequency Phase-Lagged Unsteady Simulations of Experimental Axial Compressor," *Journal of Propulsion and Power*, vol. 31, pp. 444–455, doi: 10.2514/1.B35247, 2015.

[48] G.A. Gerolymos, G.J. Michon, and J. Neubauer, "Analysis and Application of Chorochronic Periodicity in Turbomachinery Rotor/Stator Interaction Computations," *Journal of Propulsion and Power*, vol. 18, pp. 1139–1152, 2002.

[49] G.A. Gerolymos, "Filtered Chorochronic Interface as a Capability for 3-D Unsteady Throughflow Analysis of Multistage Turbomachinery," *Int. J. Comp. Fluid Dynamics*, vol. 27, pp. 100–117, 2013.

[50] X.D. Liu, S. Osher, T. Chan, "Weighted Essentially Non-Oscillatory Schemes," *J.Comput.Phys.*, vol. 115, pp. 200–212, 1994.

[51] G.S. Jiang, C.W. Shu, "Efficient Implementation of Weighted ENO Schemes," *J.Comput.Phys.*, vol. 126, pp. 202–228, 1996.

[52] C.W. Shu, "Essentially Non-Oscillatory and Weighted Essentially Schemesfor Hyperbolic Conservation Laws." NASA/CR-97-206253, 1997.

[53] B. Van Leer, "Towards the Ultimate Convservative Difference Scheme, V: A Second-Order Sequel to Godunov's Method," *J. of Computational Physics*, vol. 32, pp. 101–136, 1979.

[54] S.H. Zhang, C.W. Shu, "A New Smoothness Indicator for the WENO Schemes and its Effect on the Convergence to Steady State Solutions," *Journal of Scientific Computing*, vol. 31, pp. 273–305, 2007.

[55] A.K. Henrick, T.D. Aslam, J.M. Powers, "Mapped Weighted Essentially Non-Oscillatory Schemes:Achiving Optimal Order Near Critical Points," *J.Comput.Phys.*, vol. 208, pp. 206–227, 2005.

[56] Y.Q. Shen, and G.C. Zha, "Improvement of the WENO Scheme Smoothness Estimator," *International Journal for Numerical Methods in Fluids*, vol. 64,, pp. 653–675, DOI:10.1002/fld.2186, 2009.

[57] Y.Q. Shen, G.C. Zha, and B.Y. Wang, "Improvement of Stability and Accuracy of Implicit WENO Scheme," *AIAA Journal*, vol. 47, pp. 331–334, DOI:10.2514/1.37697, 2009.

[58] Y.Q. Shen, G.C. Zha, and X. Chen, "High Order Conservative Differencing for Viscous Terms and the Application to Vortex-Induced Vibration Flows," *Journal of Computational Physics*, vol. 228(2), pp. 8283–8300, doi:10.1016/j.jcp.2009.08.004, 2009.

[59] P. Roe, "Approximate Riemann Solvers, Parameter Vectors, and Difference Schemes," *Journal of Computational Physics*, vol. 43, pp. 357–372, doi:10.1016/0021–9991(81)90128–5, 1981.

[60] B. Van Leer, J.L. Thomas, P.L. Roe, and R.W. Newsome, "A Comparison of Numerical Flux Formulas for the Euler and Navier-Stokes Equations." AIAA paper 87-1104, 1987.

[61] M.S. Liou, and C.J. Steffen, "A New Flux Splitting Scheme," *Journal of Computational Physics*, vol. 107, pp. 1–23, 1993.

[62] A. Jameson, "Analysis and Design of Numerical Schemes for Gas Dynamics I: Artificial Diffusion, Upwind Biasing, Limiters and Their Effect on Accuracy and Multigrid Convergence in Transonic and Hypersonic Flow," *Journal of Computational Fluid Dynamics*, vol. 4, pp. 171–218, 1995.

[63] A. Jameson, "Analysis and Design of Numerical Schemes for Gas Dynamics II: Artificial Diffusion and Discrete Shock Structure," *Journal of Computational Fluid Dynamics*, vol. 5, pp. 1–38, 1995.

[64] G.C. Zha, Y.Q. Shen, and B.Y. Wang, "An Improved Low Diffusion E-CUSP Upwind Scheme ," *Journal of Computer and Fluids*, vol. 48, pp. 214–220, 2011, doi:10.1016/j.compfluid.2011.03.012.

[65] J.R. Edwards, "A Low-Diffusion Flux-Splitting Scheme for Navier-Stokes Calculations." AIAA Paper 95-1703-CP, June, 1995.

[66] J.R. Edwards, "A Low-Diffusion Flux-Splitting Scheme for Navier-Stokes Calculations," *Computer & Fluids*, vol. 6, pp. 635–659, doi:10.1016/S0045–7930(97)00014–5, 1997.

[67] S.A. Orszag, "Analytical Theories of Turbulence," *Journal of Fluid Mechanics*, vol. 41, pp. 363–386, 1970.

[68] G. Erlebacher, M. Y. Hussaini, C. G. Speziale, and T. A. Zang, "Toward the Large Eddy Simulation of Compressible Turbulent Flows," *Journal of Fluid Mechanics*, vol. 238, pp. 155–185, 1992, DOI:10.1017/S0022112092001678.

[69] P.R. Spalart, W.H. Jou, M. Strelets, and S.R. Allmaras, "Comments on the Feasibility of LES for Wings, and on a Hybrid RANS/LES Approach." Advances in DNS/LES, 1st AFOSR Int. Conf. on DNS/LES, Greyden Press, Columbus, H., Aug. 4-8, 1997.

[70] P.R. Spalart, S. Deck, M. Shur, and K.D. Squires, "A New Version of Detached Eddy Simulation, Resistant to Ambiguous Grid Densities," *Theoritical and Computational Fluid Dynamics*, vol. 20, pp. 181–195, 2006.

[71] P.R. Spalart, and S.R. Allmaras, "A One-equation Turbulence Model for Aerodynamic Flows." AIAA-92-0439, 1992.

[72] G.-C. Zha, and E. Bilgen, "Numerical Study of Three-Dimensional Transonic Flows Using Unfactored Upwind-Relaxation Sweeping Algorithm," *Journal of Computational Physics*, vol. 125, pp. 425–433, May 1996.

[73] Y.Q. Shen, B. Wang, and G.C. Zha, "Comparison Study of Implicit Gauss-Seidel Line Iteration Method for Transonic Flows." AIAA Paper 2007-4332, 2007.

[74] Zha, G.C., Shen, Y.Q., and Wang, B.Y., "Calculation of Transonic Flows Using WENO Method with a Low Diffusion E-CUSP Upwind Scheme." AIAA Paper 2008-0745, 46th AIAA Aerospace Sciences Meeting, Reno, NV, Jan. 2008.

[75] Y.Q. Shen, and G.C. Zha, "Large Eddy Simulation Using a New Set of Sixth Order Schemes for Compressible Viscous Terms," *Journal of Computational Physics*, vol. 229, pp. 8296–8312, doi:10.1016/j.jcp.2010.07.017, 2010.

[76] A. Jameson, "Time Dependent Calculations Using Multigrid with Applications to Unsteady Flows Past Airfoils and Wings." AIAA Paper 91-1596, 1991.

[77] J. Alonso, L. Martinelli, and A. Jameson, "Multigrid Unsteady Navier-Stokes Calculations with Aeroelastic Applications." AIAA Paper 95-0048, 1995.

[78] Y.Q. Shen, B.Y. Wang, and G.C. Zha, "Implicit WENO Scheme and High Order Viscous Formulas for Compressible Flows ." AIAA Paper 2007-4431, 2007.

[79] A.J. Strazisar, J.R. Wood, M.D. Hathaway, and K.L. Suder, "Laser Anemometer Measurements in a Transonic Axial-Flow Fan Rotor." NASA Technical Paper 2879, November, 1989.

[80] H.D. Vo, C.S. Tan, and E.M. Greitzer, "Criteria for Spike Initiated Rotating Stall," *AMSE J. of Turbomach.*, vol. 130, pp. 1–8, doi:10.1115/1.2750674, 2008.

[81] L. He, "Computational Study of Rotating-Stall Inception in Axial Compressors," *Journal of Propulsion and Power*, vol. 13, pp. 31–38, doi: 10.2514/2.5147, 1997.

[82] D.A. Hoying, C.S. Tan, H.D. Vo, and E.M. Greitzer, "Role of Blade Passage Flow Structures in Axial Compressor Rotating Stall Inception," *AMSE J. of Turbomach.*, vol. 121, pp. 735–742, doi:10.1115/1.2836727, 1999.

[83] J.D. Denton, "Lessons from Rotor 37," *Journal of Thermal Science*, vol. 6, pp. 1–13, doi: 10.1007/s11630–997–0010–9, 1996.

[84] J. Dunham, “CFD Validation for Propulsion System Components.” AGARD-AR-355, 1998.

[85] H.D. Vo, “Rotating Stall Suppression in Axial Compressors with Casing Plasma Actuation,” *Journal of Propulsion and Power*, vol. 26, pp. 808–818, doi: 10.2514/1.36910, 2010.

[86] H.D. Vo, “Role of Tip Clearance Flow on Axial Compressor Stability.” Ph.D. Thesis, MIT, 2002.

[87] H.S. Im, X.Y. Chen, and G.C. Zha, “Simulation of 3D Multistage Axial Compressor Using a Fully Conservative Sliding Boundary Condition.” ASME IMECE2011-62049, International Mechanical Engineering Congress & Exposition, Denver, November 2011, 2011.

[88] B. Wang, Z. Hu, and G. Zha, “A General Sub-Domain Boundary Mapping Procedure For Structured Grid CFD Parallel Computation,” *AIAA Journal of Aerospace Computing, Information, and Communication*, vol. 5, pp. 425–447, 2008.

[89] D.A. Espinal, H.S. Im, and G.C. Zha, “Full-Annulus Simulation of Non-Synchronous Blade Vibration Excitation of an Axial Compressor.” AIAA Paper 2014-0790, AIAA SciTech, 52nd Aerospace Sciences Meeting, 13-17 January 2014, National Harbor, Maryland, 2014.